DISSERTATION

ON THE INTERACTIONS BETWEEN TROPICAL CONVECTION AND GRAVITY WAVES: COMPARISONS BETWEEN SIMPLE MODELS AND NUMERICAL SIMULATIONS

Submitted by

Stefan Tulich

Department of Atmospheric Science

In partial fulfillment of the requirements

for the degree of Doctor of Philosophy

Colorado State University

Fort Collins, Colorado

Fall 2003

COLORADO STATE UNIVERSITY

July 18, 2003

WE HEREBY RECOMMEND THAT THE DISSERTATION PREPARED UNDER OUR SUPERVISION BY STEFAN NEIL TULICH ON THE INTERACTION BETWEEN TROPICAL AND GRAVITY WAVES: COMPARISONS BETWEEN SIMPLE MODELS AND DIRECT NUMERICAL SIMULATIONS BE ACCEPTED AS FULFILLING IN PART REQUIREMENTS FOR THE DEGREE OF DOCTOR OF PHILOSOPHY.

Committee on Graduate Work

Adviser

Department Head

ABSTRACT OF DISSERTATION

ON THE INTERACTIONS BETWEEN TROPICAL CONVECTION AND GRAVITY WAVES: COMPARISONS BETWEEN SIMPLE MODELS AND NUMERICAL SIMULATIONS

The interactions between tropical convection and atmospheric waves are investigated in an idealized, i.e., two-dimensional (2D) and non-rotating, framework. A primary goal is to determine whether and, if so, how tropical convection can "spontaneously" become organized through gravity wave dynamics. This will provide important groundwork for future studies aimed at improving the representation of tropical convective variability in numerical weather and climate prediction models.

The dissertation is made up of three parts. The first investigates the linear response of an initially motionless tropical atmosphere to a spatially and temporally localized deep convective heat source. Consistent with output from high-resolution numerical simulations, results show that the heat source tends to strongly excite gravity wave packets with phase speeds in the range 35-45 m s^{-1} and16-20 m s^{-1}, and that the passage of the faster- (slower-) moving packets should tend to inhibit (favor) the development of additional deep convection.

Part II discusses a linear tropical wave model in which vertical structure is truncated to include just two vertical normal modes: a fast-moving (first internal) mode and a slow-moving (second internal) mode. Based on the notion that deep convective development is strongly inhibited by the effects of dry air entrainment, anomalies in deep convective heating are assumed to be directly proportional to anomalies in column-integrated moisture. The model predicts that convectively coupled gravity waves, with realistic phase speeds and vertical temperature structures, should spontaneously develop from random initial conditions, even in the absence of a mean flow. Owing to an assumed temporal lag of stratiform precipitation processes with respective to deep convection, the largest growth rates of the unstable waves are found to occur at a wavelength of about 2000 km.

In Part III, a vertical normal mode transform algorithm is used to analyze the structure and energetics of large-scale [O(1000 km)] convectively coupled gravity waves that spontaneously develop in a 2D cloud resolving model simulation of radiative convective equilibrium. Results show that the simulated waves primarily owe their existence to an unstable interaction between convection and modes with phase speeds in the range 16-18 m s^{-1} (i.e., third internal modes). Stratiform heating processes are found to play an important role in maintaining the energy of these modes, in agreement with the stratiform instability theory. In contrast to this theory, however, deep convective heating processes also play an important role.

Stefan Neil Tulich
Department of Atmospheric Science
Colorado State University
Fort Collins, CO 80523
Fall 2003

ACKNOWLEDGEMENTS

I first and foremost acknowledge GOD for providing me with the strength and courage to achieve this goal. Next, I would like to thank my adviser, Prof. David Randall, for his encouragement and support, for his willingness to allow me to pursue my own research interests, and finally, for his patience. I also thank Profs. Wayne Schubert and Mike Montgomery, both members of my committee, for their friendship and encouragement and for their helpful discussions. The work described in this dissertation would not have been possible without the countless hours of instruction given by Prof. Wayne Schubert. I also thank Simon Tavener for serving on my committee.

I thank each of the members of the Randall Research Group (Mark Branson, Don Dazlich, Charlotte Demott, Mostafa El-Kady, Laura Fowler, Ross Heikes, Marat Khairoutdinov, Cara-Lyn Lappen, Todd Ringler, and Kelley Wittmeyer) for providing me with solutions to problems I have encountered during the course of my research. I would also like to acknowledge the "behind-the-scene" work of the administrative staff here at Colorado State University, especially that of Fredi Boston, Cindy Carrick, Michelle McDaniel, and Melissa Tucker.

Special thanks go to Dr. Marat Khairoutdinov for providing me with his cloud resolving model and for teaching me how to use it. I also acknowledge Dr. Scott Fulton for providing me with his vertical normal mode transform algorithm and for teaching me how to use it. The assistance of Lyle Pakula in using the super-computers at the National Center for Atmospheric Research (NCAR) is also greatly appreciated.

Finally, I am grateful for the unwavering encouragement, support, and prayers of my family and friends, especially my fiance, Mandy Fisher, and also Phil Watson, Cindy Frost, Andrew Davies, D.J. Eschelman, Rick Edwards, and Chad Smith. GOD has truly blessed me with such friends and loved ones.

This research was supported by the National Science Foundation under Grant ATM-9812384 and by the National Oceanic and Atmospheric Administration under Contract NA17RJ1228.

CONTENTS

CHAPTER 1 INTRODUCTION....1

1.1 Motivation and background....1
1.2 Two theories of coupled wave instability....6
1.2.1 Wave-CISK....6
1.2.2 Stratiform Instability....8
1.2.2.1 A problem with stratiform instability theory....11
1.3 An alternative theory of coupled wave instability....13
1.4 Research strategy....15
1.5 Outline of dissertation....17

CHAPTER 2 ON THE STRUCTURE AND ENERGETICS OF GRAVITY WAVES EXCITED BY DEEP CONVECTION....19

2.1 Introduction....19
2.1.1 Motivation....19
2.1.2 Research objectives....22
2.2 The vertical normal mode transform....23
2.2.1 Theory....23
2.2.2 Application to a realistic tropical sounding....26
2.3 The linear gravity wave response to a deep convective heat source....29
2.3.1 Derivation of the solution....30
2.3.2 Properties of the solution....33
2.3.3 CAPE, CIN, and PW_{FT}....38
2.3.4 The effects of steady translation....41
2.3.5 Summary and discussion....43
2.4 Numerical simulation of an isolated cloud....45
2.4.1 Numerical model....46
2.4.2 Experimental setup....47
2.4.3 Model analysis strategy....48
2.4.4 Results....50
2.4.5 Summary and discussion....55

CHAPTER 3 A SIMPLE MODEL OF CONVECTIVELY COUPLED GRAVITY WAVES 57

3.1 Introduction 57
3.2 The moisture convergence model 59
3.2.1 Model development 59
3.2.1.1 Convective parameterization 60
3.2.1.2 Convective heating profiles 62
3.2.1.3 Solution procedure 65
3.2.2 Analysis 67
3.2.2.1 Energetics 70
3.2.2.2 The effects of stratiform heating 71
3.3 The moisture relaxation model 72
3.3.1 Model development 74
3.3.3.1 Energetics 77
3.3.2 Analysis 77
3.3.3 The effects of stratiform precipitation processes 80
3.3.3.1 Parameterization of stratiform precipitation processes 82
3.3.3.2 Model equations 83
3.3.3.3 Analysis 84
3.4 Summary and conclusions 88

CHAPTER 4 LARGE-SCALE CONVECTIVELY COUPLED GRAVITY WAVES IN A TWO-DIMENSIONAL CLOUD RESOLVING MODEL 92

4.1 Introduction 92
4.2 Experimental setup 93
4.3 A convection classification scheme 94
4.4 The vertical normal mode transform: implementation 95
4.5 General features of the simulation 97
4.5.1 Space-time evolution 97
4.5.2 Convective partitioning 99
4.5.2.1 Convective heating profiles 101
4.5.2.2 Convective heating spectra 103
4.6 Time-mean wave structure and energetics: analysis in physical space 105
4.6.1 Wave structure 105
4.6.1.1 Surface precipitation 107
4.6.1.2 Precipitable water and moisture convergence 107
4.6.1.3 CAPE, CIN, and surface heat flux 110
4.6.2 Energetics 115
4.6.2.1 Energy production 117
4.7 Time-mean wave structure and energetics: analysis in spectral space 122
4.7.1 Wave structure 122
4.7.2 Energetics 124
4.7.2.1 Energy production 127

4.7.2.2 Distribution of energy production 129
4.8 Transient structure of the large-scale waves 132
4.8.1 Methodology 132
4.8.2 Results 132
4.9 Summary and discussion 138

CHAPTER 5 IMPORTANT FINDINGS AND SUGGESTIONS FOR FUTURE RESEARCH 142

5.1 What's new 143
5.2 Future research 148

CHAPTER 1

INTRODUCTION

1.1 Motivation and background

Convectively coupled Kelvin waves, a.k.a. "super clusters", have been well documented as a dominant mode of submonthly tropical weather variability (Takayubu 1994, Wheeler and Kiladis 1999; Straub and Kiladis 2002). They are large-scale eastward moving cloud disturbances with phase speeds in the range 11-22 m s^{-1} and the dispersion characteristics of shallow-water Kelvin modes. The convective envelope associated with the waves extends roughly 1000 km in the horizontal and is typically comprised of several smaller-scale [O(100 km)], westward-moving 'cloud clusters' (see Fig. 1.1, adopted from Nakazawa 1988; Straub and Kiladis 2002). Longitude-height cross-sections of the temperature anomalies associated with the waves display a "boomerang"-like structure with the elbow of the boomerang located in the upper troposphere (Wheeler et al. 2000, Straub and Kiladis 2002). The deep convection associated with the waves is strongest when air is anomalously cool in the lower troposphere, anomalously warm in the upper troposphere,

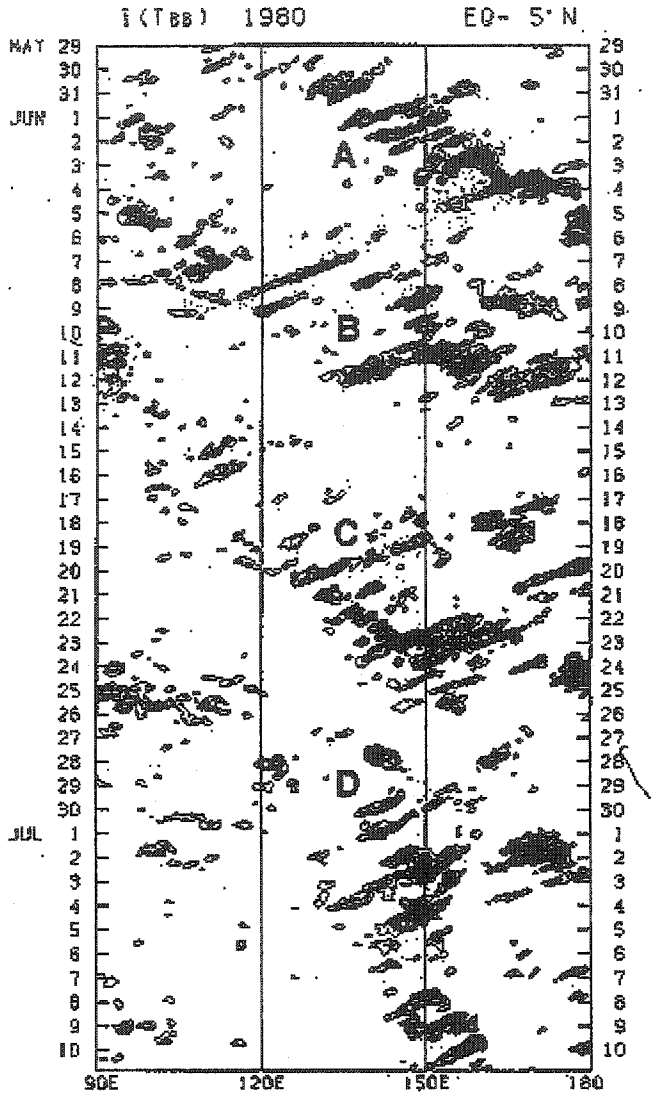

Figure 1.1 Hovmoller diagram of an index of deep convective cloudiness (averaged between the equator and 5° N) derived from 3-hourly Geostationary Meteorological Satellite (GMS) observations of outgoing longwave radiation collected between May 29 and July 10, 1980 (taken from Nakazawa 1988).

and anomalously cool at the level of the tropopause (Wheeler et al. 2000, Straub and Kiladis 2002).

As with other types of convectively coupled equatorial waves, convectively coupled Kelvin waves are characterized by an implied equivalent depth in the range 12-50 m. This

equivalent depth is much shallower than that predicted theoretically as the peak projection response to deep convective heating (e.g. Fulton and Schubert 1985). Determining the mechanisms that lead to such a shallow equivalent depth is one of the fundamental issues yet to be resolved in tropical meteorology. Another unresolved issue is whether convectively coupled Kelvin waves represent a mode of tropical convective "self-organization", i.e., whether they can spontaneously develop from random initial conditions, under uniform large-scale forcing and uniform lower boundary conditions. Addressing these issues is of interest from a practical perspective of improving the representation of convectively coupled waves in general circulation models. A need for such improvements has recently been emphasized by Randall et al. (2003).

Several different theories have been proposed to explain the existence and dynamics of large-scale waves coupled to convection including wave-CISK (Conditional Instability of the Second Kind; Hayashi 1970, Lindzen 1974), stratiform instability (Mapes 2000, Majda and Schefter 2001) and WISHE (Wind Induced Surface Heat Exchange; Emanuel et al. 1994 and the references therein). The first two theories are similar to one another in that they both predict that convectively coupled Kelvin waves should spontaneously develop from random initial conditions, even in the absence of a mean easterly flow. WISHE theory, on the other hand, predicts that convection acts to remove energy from these waves in the absence of a mean easterly flow.

Grabowski and Moncrieff (2001) recently used a two-dimensional (2D) cloud resolving model (CRM) to investigate the problem of spontaneous wave development in a controlled experimental setting. They conducted a 30-day simulation of radiative-convective equilibrium in a non-rotating planetary-scale domain with: 1) a prescribed spatially uni-

form radiative cooling profile, 2) a prescribed spatially uniform easterly flow, and 3) a prescribed spatially uniform sea-surface temperature (SST). Starting from a state of random convection, they observed the spontaneous development of a series of large-scale convectively coupled gravity waves. The authors noted that the phase speed, vertical temperature structure (depicted in Fig. 1.2a), and inner-convective structure of the simulated waves bear strong resemblance to observations of convectively coupled Kelvin waves. Based on results from an additional 15 day simulation, starting on day 15 of the control simulation and with the interactive surface fluxes "turned off", the authors concluded that the mechanism of WISHE is not required for the maintenance of the simulated waves. It is not clear, however, whether the mechanism of WISHE is needed for their development.

Inspired by Grabowski and Moncrieff's (2001) success, this study uses a 2D CRM to conduct a 15-day numerical simulation of radiative convective equilibrium in a non-rotating, periodic domain extending 8192 km in the horizontal with a prescribed spatially uniform radiative cooling profile and a prescribed spatially uniform SST. To eliminate the mechanism of WISHE, the horizontal winds are uniformly relaxed to zero on a 4 hr time scale. Results (presented in Chapter 4) show the spontaneous development of two large-scale convectively coupled gravity waves that propagate eastward (i.e., to the right) at a speed of about 16 m s^{-1}. The convective envelopes associated with waves extend roughly 1000 km in the horizontal and are comprised of several smaller-scale cloud clusters that successively form to the east but propagate to the west. Similar to Grabowski and Moncrieff (2001), the temperature perturbations associated with the waves exhibit a boomerang-like structure with the elbow of the boomerang located in the upper troposphere. The deep convection associated with the waves is strongest when air is anomalously cool in the

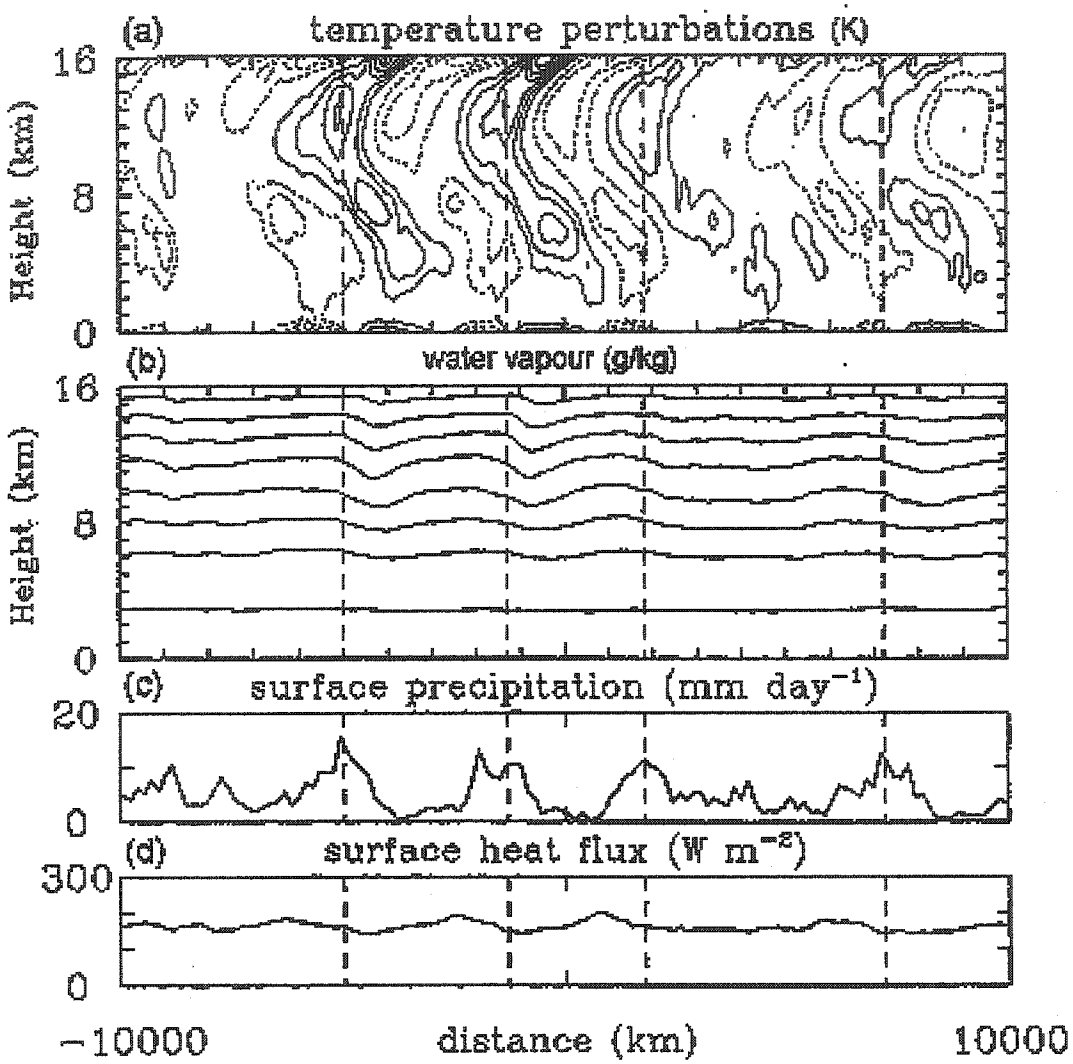

Figure 1.2 Spatial distributions of (a) temperature perturbations (from the domain average at each level), (b) water vapor mixing ratio, (c) surface precipitation, and (d) the total surface heat flux associated with large-scale, eastward moving convective envelopes produced in a CRM simulation performed by Graboswki and Moncrieff (2001). Contour interval for the temperature perturbations are 0.2 K and full (dashed) contours are for positive (negative) perturbations.

lower troposphere, anomalously warm in the upper troposphere, and anomalously cool at the level of the tropopause.

The results obtained here suggest that large-scale convectively coupled gravity waves can spontaneously develop from random initial conditions, even in the absence of a mean

flow. What are the mechanisms responsible for the development and maintenance of these waves? Also, what determines their speed? The following paragraphs provide a brief discussion of two different theories that offer possible answers to these questions: wave-CISK and stratiform instability theory. Section 1.3 then proposes an alternative theory for the spontaneous development of large-scale convectively coupled gravity waves. A strategy for assessing the predictions and assumptions of these three different theories using model output is then outlined in Section 1.4. The organization of the dissertation is discussed in Section 1.5.

1.2 Two theories of coupled wave instability

1.2.1 Wave-CISK

The term "wave-CISK" (Conditional Instability of the Second Kind) refers to the cooperative interaction between small-scale cumulus clouds and a large-scale atmospheric wave. Conceptually, low-level convergence associated with the wave promotes enhanced amounts of convection that, in turn, provides energy to the wave.

Linear wave-CISK models have been developed by a number of investigators including Hayashi (1970), Lindzen (1974), Crum and Stevens (1983), and Chang and Lim (1988). Although these models generally differ from one another in the way that the convective heating is related to the low-level convergence, they each predict that, for certain choice of model parameters, convectively coupled Kelvin waves should spontaneously develop from random initial conditions. The unstable waves propagate at speeds in the range 10-30 m s^{-1}, depending on the vertical profile and strength of the heating, and

exhibit a westward tilt with height in the troposphere (Crum and Stevens 1983, Chang and Lim 1988).

The mechanism of wave-CISK involves a cooperative interaction between convection and two vertical normal modes that are phase-locked with one another: a fast-moving mode and a slow-moving mode. (Crum and Stevens 1983, Lau and Peng 1987, Chang and Lim 1988). As demonstrated in Chapter 3 (see also Numagati and Hayashi 1991), this phase-locking tends to occur whenever the convergence field of the fast mode *lags* that of the slow mode, thereby allowing eddy generation of available potential energy in both modes. Owing to the effects of an effectively reduced static stability, the unstable waves propagate at a speed close to that of the slow-moving mode.

A well-known problem with most wave-CISK models is that they predict the largest growth rates to occur at the smallest scales. Thus, they cannot explain the large-scale organization of tropical convection. Davies (1979) suggested that this problem could be avoided by introducing a finite lag time (τ_a) between the convective heating and the low-level convergence. Physically, τ_a can be regarded as the time it takes a cumulus ensemble to adjust to changes in the large-scale forcing. Using a linear wave-CISK model with the effects of finite adjustment time included, he demonstrated that Kelvin wave-CISK modes, with synoptic to planetary scale wavelengths and periods on the order of 10 days, are rendered unstable when τ_a exceeds 6 hrs.

Evidence for the existence of a lag between convection and large-scale forcing can be found in the numerical modelling work of Xu and Randall (1996). Running a CRM with time-varying large-scale forcing and a horizontal resolution of 2 km, they showed that changes in the spatially averaged precipitation rate tend to lag those of the generalized

convective available potential energy (GCAPE; Wang and Randall 1994) by 1-5 hrs depending on the choice of averaging distance and also depending on the shape of the imposed cooling and moistening profiles.

1.2.2 Stratiform Instability

Radar observations collected during the Tropical Ocean Global Atmosphere Coupled Ocean-Atmosphere Response Experiment (TOGA-COARE) indicate that about 60-70% of the total rain volume over the equatorial western Pacific is generated by spatially localized convective cells, while the remaining 30-40% falls over wide-spread regions in the form of stratiform precipitation spawned by deep convection (Rickenbach and Rutledge 1998). Figs. 1.3a and c illustrate the characteristic profiles of latent heating within deep convective and stratiform regions of precipitation, respectively (adopted from Houze 1997). The deep convective heating profile shows warming across the depth of the troposphere with a maximum in the middle troposphere. The stratiform heating profile, on the other hand, shows warming at upper-levels and cooling at low-levels.

Figs. 1.3b and d illustrate the characteristic profiles of the horizontal divergence that are most efficiently excited in regions of deep convection and stratiform precipitation, respectively. The former shows low-level convergence and upper-level divergence (a first internal mode response), while the latter shows mid-level convergence and upper- and lower-level divergence (a second internal mode response).

With the above observations and atmospheric responses to convection in mind, Mapes (2000) developed a simple tropical wave model that includes separate treatments of deep convection, mid-level convection, and stratiform precipitation and with vertical resolution

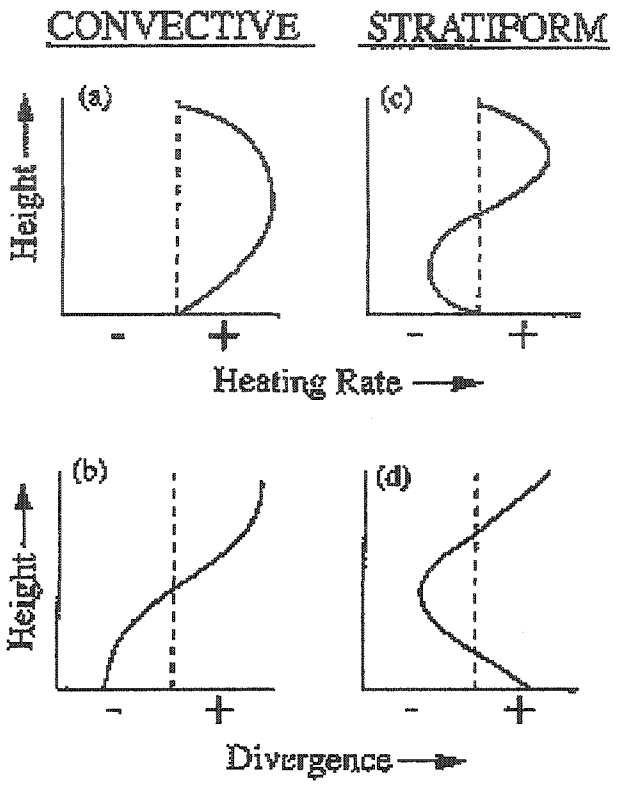

Figure 1.3 Characteristic profiles of convective heating and horizontal divergence in regions of deep convective (a and b, respectively) and stratiform (c and d, respectively) regions of precipitation (taken from Houze, 1997)

truncated to include just two vertical normal modes: a first internal mode with a gravity wave phase speed (c_n) of 52 m s^{-1} and a second internal mode with c_n = 23 m s^{-1}. Three important assumptions in the model are as follows. First, stratiform heating lags deep convective heating and decays exponentially on a 3 hr time scale. Second, deep convection *solely* excites the first internal mode, while stratiform convection *solely* excites a second internal. Third, variations in congestus heating act in such a way as to damp temperature perturbations associated with second internal mode.

Mapes (2000) identifies two different regimes in the model's parameter space. The first, where variations in deep convection are primarily controlled by CAPE (convective available potential energy), shows no growing instabilities, while the second, where varia-

tions in deep convection are primarily controlled by CIN (convective inhibition), shows the spontaneous development of "stratiform instability" waves. For a certain choice of model parameters, Mapes finds that the horizontal scale (O[1000 km]), phase speed (~ 20 m s^{-1}), and vertical temperature structure of the unstable waves broadly agree with Wheeler et al.'s (2000) observations of convectively coupled Kelvin waves. Straub (2002), however, points out that in observations, upper-level warm temperature anomalies are in phase with convective heating anomalies, while in Mapes' simulated waves, upper-level warm temperature anomalies lead convective heating anomalies by a quarter wave cycle.

The mechanism of stratiform instability, in the case of an eastward moving gravity wave, can be summarized as follows (see also Fig 1.4). First, a reduction in CIN, associated with the passage of the second internal mode, leads to anomalous deep convective heating and hence, anomalous stratiform heating that peaks three hours later. The anomalous stratiform heating acts to further excite the second internal mode which propagates eastward to generate additional deep convection. At the same time, linearly enhanced congestus heating acts to damp the second internal mode and thus, damp the growth of the instability.

Majda and Schefter (2001) later performed a linear stability analysis of a simple tropical wave model that also includes just two vertical normal modes but where variations in deep convection are controlled solely by CAPE. Their model still allows for stratiform instability, however, because CAPE is parameterized as being proportional to $\theta_{eb} - \theta^*_{em}$, where θ_{eb} is the equivalent potential temperature of air in the boundary layer and θ^*_{em} is the saturation equivalent potential temperature of air in the *lower-middle*-troposphere.

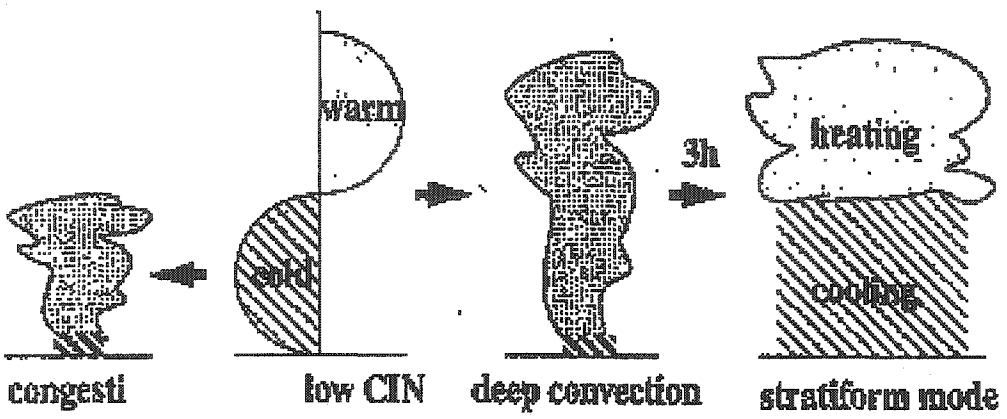

Figure 1.4 Schematic diagram illustrating Mapes' (2000) stratiform instability mechanism for the spontaneous development of convectively coupled waves (adopted from Mapes 2000).

Thus, stratiform cooling in the lower-troposphere can promote the development of deep convection owing to its positive impact on CAPE. Because Majda and Schefter's (2001) version of CAPE does not depend on temperature changes in the upper-troposphere, we will hereafter refer to this measure as "shallow-CAPE".

Choosing a stratiform adjustment time of 3 hrs, Majda and Schefter (2001) demonstrated the existence of stratiform instability waves with maximum growth rates occurring at scales of either 200 or 1200 km, depending on the choices of model parameters. Although the unstable waves arise through the coupling of convection to the second internal mode, their phase speeds actually range between 11 and 15 m s^{-1}, considerably slower than the waves produced in Mapes' (2000) model.

1.2.2.1 A problem with stratiform instability theory?

An important assumption made in the aforementioned models is that deep convection does not, by itself, cause a reduction in CIN or an increase in shallow-CAPE, i.e., that deep convection does not strongly excite higher-order gravity modes. A recent test of this

assumption can be found in the work of Lane and Reeder (2001) who conducted a 2D numerical simulation of an isolated deep convective cloud. Their Hovmoller diagrams of CAPE and CIN reveal a series of gravity wave disturbances that radiate from the cloud at different speeds. One of these disturbances travels at a speed of about 15 m s^{-1} and appears as ~ 20 km wide region where CIN is reduced by as much as 33% from its background value, while CAPE remains largely unaffected. Both the speed and vertical temperature structure of this disturbance suggest that it can be classified as a third internal mode gravity wave packet excited by the cloud.

Does the passage of the third internal mode promote the development of deep convection? Results from Ouchi's (1999) 2D CRM simulation of a large-scale eastward moving convectively coupled gravity wave suggest that the answer to this question is yes. His Figs. 6a and b, shown here in Figs. 1.5a and b, are Hovmoller diagrams of the simulated cloud water (a) and upward motion (b) at a height of 3 km. The diagrams are for an arbitrary five hour period during the simulation, and they focus on a 160 km section of the eastward moving wave.

In Fig. 1.5a, we see the successive eastward development of mesoscale groups westward of cloud features. The cloud features are roughly 10 km wide and they consist of one or more convective cells. Fig 1.5b shows packets of upward motion emanating from these convective cells at phase speeds of about 14 m s^{-1}. Both their speed and non-dispersive nature suggests that they can be classified as gravity wave packets generated by the convective cells. Because the development of cloud features typically coincides with the arrival of the eastward moving gravity wave packets, it seems reasonable to hypothesize

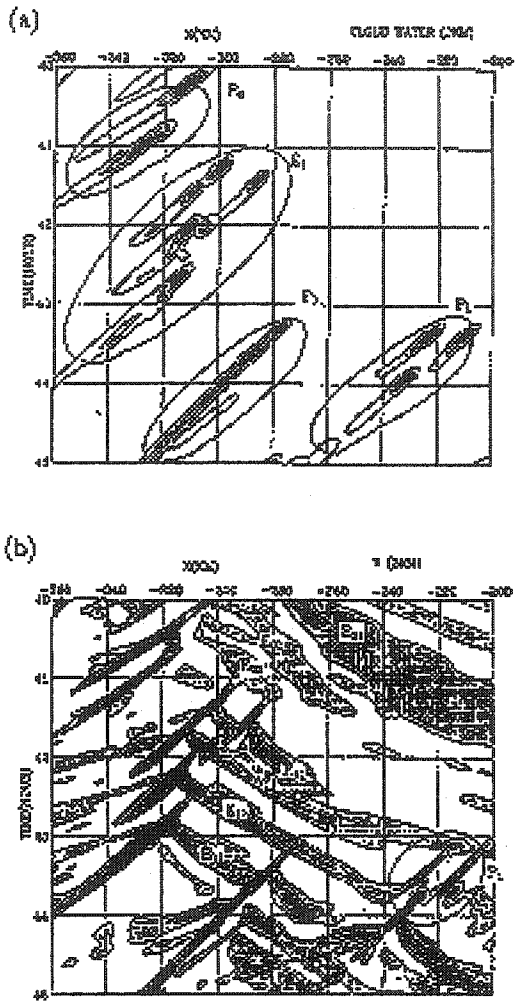

Figure 1.5 Hovmoller diagrams of cloud water mixing ratio (a) and upward motion (b) at 3 km for a 5 hour time period from 2D CRM simulation of an eastward moving cloud disturbance. The diagrams are focused on a 160 km section of the disturbance (the model domain extends 7200 km in the horizontal direction). In (b), dark hatched regions denote cloud regions. Adopted from Ouchi's (1999) Figs. 6a and b.

that the 14 m s^{-1} mode (a third internal mode) can indeed promote the development of deep convection.

1.3 An alternative theory for coupled wave instability

The aforementioned results suggest the possibility that deep convective heating processes, as well as stratiform heating processes, play an important role in the spontaneous

development and maintenance of convectively coupled gravity waves. Presumably, this could happen via a stratiform instability-type mechanism, in which deep convection promotes the development of additional deep convection via its excitation of a third (or second) internal mode and the subsequent impact of this mode on CIN. Alternatively, the passage of this mode might favor the development of deep convection owing to its positive impact on the vertically integrated moisture content of the free troposphere (demonstrated in the next chapter). This moistening would serve to partially offset the detrimental effects of cumulus entrainment, thereby allowing clouds to reach higher altitudes. Observations by Sherwood (1999) provide evidence that the primary factor controlling the "outbreak" of deep convection over the western Pacific Warm Pool region is the moisture content of the free troposphere. Grabowski (2003) later demonstrated that interactions between convection and water vapor are crucial for the maintenance of Madden Julian Oscillation-(MJO-) like coherent structures produced in a global primitive equation model with a CRM used for a convective parameterization.

Goswami and Rao (1994) developed a simple tropical wave model in which convective heating anomalies are directly proportional to column-integrated moisture anomalies; the constant of proportionality is a moisture relaxation time-scale τ_r. To simplify their analysis, they truncated the vertical structure of the model to include only the first internal mode. Choosing $\tau_r \approx 0.7$ days, the authors found that planetary-scale Kelvin waves with periods on the order of 30-50 days are rendered unstable in the presence of a mean easterly flow (via the mechanism of WISHE). All waves were found to be damped, on the other hand, in the absence of a mean easterly flow. Fuchs and Raymond (2002) later obtained qualitatively similar results using a model based on a slightly different set of physical

assumptions but with vertical structure also truncated to include only the first internal mode.

Extending the work of Goswami and Rao (1994) and Fuchs and Raymond (2002), Chapter 3 of the present study develops a linear 2D tropical wave model, in which: 1) deep convective heating is directly related to column integrated moisture anomalies, and 2) vertical structure is truncated to include both a fast and slow vertical normal mode. Importantly, the model predicts that convectively coupled gravity waves should tend to spontaneously develop from random initial conditions, even in the absence of a mean flow. The unstable waves, referred to here as moisture instability- (MI-) waves, propagate at phase speeds close to that of the slow moving mode and exhibit a westward tilt with height in the troposphere. Much like classical wave-CISK models, the largest growth rates are found to occur at the smallest scales. The degree of the "ultraviolet catastrophe" is generally not as severe in this case, however, and is found to be completely eliminated when the effects of a delay between stratiform and deep convective heating processes are included. Even in the latter case, however, deep convective heating processes are found to generate a substantial fraction of the energy in the slow vertical normal mode.

1.4 Research strategy

The three theories discussed above (i.e., wave-CISK, stratiform instability, and moisture relaxation) each predict that large-scale convectively coupled gravity waves (with realistic phase speeds, spatial scales, and vertical temperature structures) should spontaneously develop from random initial conditions even in the absence of a mean flow. Given that these theories differ from one another in the way that the convective heating is parameterized (as well as in their predictions for the relative roles of deep convective and strati-

form heating processes in coupled wave instability) determining which, if any, is "on the right track" would have important applications towards improving the parameterization of convection in numerical weather and climate prediction models.

Fulton and Schubert (1985), hereafter referred to as FS85, have developed a vertical normal mode transform algorithm that can be used to calculate the projection of a given profile of meteorological data on to a discrete set of vertical normal modes. Haertel and Johnson (1998) later used such an algorithm to analyze observations of "two-day" disturbances over the equatorial western Pacific. They found that the vertical structure of the large-scale dynamical fields associated with the two-day disturbance project most strongly onto a vertical normal mode with a dry gravity wave phase speed of 20 m s^{-1} (a second internal mode). They also found that the vertical profile of the disturbance's convective heating should tend to strongly excite this vertical normal mode. Based on their results, the authors speculated that the dynamics of two-day disturbances primarily involves an unstable interaction between the disturbance's convection and the 20 m s^{-1} mode. They postulated that the unstable interaction occurs because of the impact of the 20 m s^{-1} mode on CIN.

In this study, the FS85 vertical normal mode transform algorithm is used to analyze output from the simulation of convectively coupled gravity waves described briefly in Section 1.1. Two important research questions to be addressed are as follows.

Research Question 1: Which vertical normal modes appear most prominently in the simulated wave's dynamical structure, and what are the phase relationships between these modes?

Research Question 2: What are the relative roles of deep convective, shallow convective, and stratiform heating processes in maintaining the energy in these modes?

Answers to these research questions are used to thoroughly assess existing theories of coupled wave instability. Additional assessments are made by using model output to test convective parameterizations upon which these theories are based.

1.5 Outline of the dissertation

The theoretical background of the dissertation is contained in Chapters 2 and 3. Chapter 2 has two main parts. The first studies the 2D linear response of a stably stratified atmosphere to a transient convective heat source, extending the work of Nicholls et al. (1991), Pandya et al. (1993), and Mapes (1993). The primary objectives are: 1) to better understand how the spatial and temporal structures of an isolated cloud influence the structure and energetics of the gravity waves that occur in response to the heating and 2) to assess the impact of the waves on the CAPE, CIN, and free tropospheric moisture content of the cloud's environment.

In the second part of Chapter 2, the vertical normal mode transform algorithm is used to analyze output from a 2D CRM simulation of an isolated cloud. The goal is to determine the extent to which the theoretical concepts outlined in Part 1 agree with the results of the simulation. This will serve to identify some of the limitations of using the vertical normal mode transform (a concept based on linear hydrostatic theory) to interpret output from a non-linear and non-hydrostatic numerical model.

Chapter 3 performs a linear stability analysis of an inviscid, 2D tropical wave model under two different types of convective parameterization. Results of the analysis provide quantitative predictions for the structure and energetics of both wave-CISK and MI modes. In Chapter 4, these predictions are tested using output from the 2D CRM simula-

tion of convectively coupled gravity waves. Chapter 5 summarizes the important findings of this work and makes suggestions for future research.

CHAPTER 2

ON THE STRUCTURE AND ENERGETICS OF GRAVITY WAVES EXCITED BY DEEP CONVECTION

2.1 Introduction

This dissertation seeks to improve our dynamical understanding of convectively coupled Kelvin and gravity waves. As a first step in this endeavor, the present chapter studies the gravity wave response of a 2D, stably stratified atmosphere to a transient convective heat source. The results obtained here will provide important theoretical groundwork for Chapter 3, which performs a linear stability analysis of a simple tropical wave model, and Chapter 4, which characterizes the large-scale dynamical structure of convectively coupled gravity waves in a 2D CRM. The motivation for the present study is discussed below. Specific research objectives and the outline of the chapter are discussed thereafter.

2.1.1 Motivation

Lane and Reeder (2001), hereafter referred to as LR01, recently used a 2D CRM to study the generation of gravity waves by an isolated deep convective cloud. They showed that the cloud excites a spectrum of spatially localized gravity wave disturbances with ver-

tical wavelengths that are harmonics of the depth of the troposphere. Two of these disturbances were found to have a significant impact on the CAPE and CIN of the cloud environment: a first internal mode with $c_n = 55$ m s^{-1} and a third internal mode with $c_n = 15$ m s^{-1}. The former appeared as a region where the CAPE is strongly reduced from its background value, while the CIN is increased only slightly. The latter, on the hand, appeared as a region where the CIN is strongly decreased, while the CAPE remains largely unaffected.

The notion that a deep convective cloud strongly excites a third internal mode, and that the passage of this mode causes low-level cooling and moistening, goes against much of what has previously been thought concerning the atmosphere's response to convective heating. FS85, for example, found that almost all of the energy generated by a prescribed (impulsive) deep convective heat source is partitioned in a band of first internal modes with a peak at about 48 m s^{-1}. Pandya et al. (1993) later studied the linear response of a stably stratified atmosphere to a prescribed deep convective heat source that is switched on and then maintained, extending the work of Nicholls et al. (1991). They showed that the response consists of horizontally and vertically propagating gravity wave pulses that radiate from source and whose passage causes deep adiabatic warming and drying. They do not present evidence for low-level cooling in the vicinity of the source, except when the convective heating profile includes a stratiform heating component with cooling at low-levels.

The results just mentioned, along with those of Mapes (1993), have served as the theoretical basis for the tropical wave models developed separately by Mapes (2000) and Majda and Schefter (2001). As discussed in Chapter 1, these models are based on the implicit assumption that deep convection does not, by itself, cause a reduction in CIN or

an increase in shallow-CAPE, i.e., that deep convection does not excite a second internal mode gravity wave response with cooling at low-levels.

There are several possible explanations for why the numerical results of LR01 conflict with our conceptual understanding of how the atmosphere responds to cumulus convection. The most likely is that the analytical studies of Nicholls et al. (1991), Pandya et al. (1993), and Mapes (1993) primarily focused on the atmosphere's response to a convective heat source that is switched on and then *maintained.* LR01's simulated cloud, on the other hand, is characterized by a finite lifetime. In the latter case, one expects that the cooling and moistening effects of the higher-order gravity modes will not become apparent until *after* the warming and dying effects of the lower-order modes have dispersed from the vicinity of the heated region. One also expects that a convective heat source of finite duration will be more efficient, relative to impulsive or steadily maintained heating, at generating energy in higher-order modes. This is because the higher-order modes will spend a larger amount of time in the heated region and thus, will have a greater opportunity to experience eddy generation of available potential energy.

Another point worth considering is that the vertical profile of the latent heating in LR01's simulated cloud is "top-heavy" during the later stages of its lifetime with a maximum in the upper-troposphere (see their Fig. 10). This would imply that their simulated cloud is more efficient, relative to a "pure" deep convective heat source, at generating energy in higher-order gravity modes.

Finally, LR01 demonstrated that the magnitude of the local change in buoyancy caused by non-linear advection terms is comparable to that caused by microphysical processes. On the basis of this result, they suggested that the non-linear advection of buoy-

ancy within clouds plays a central role in the generation of gravity waves. Nicholls et al. (1991), Pandya et al. (1993), and Mapes (1993), however, neglected the effects of non-linearities.

2.1.2 Research objectives

This chapter is composed of two main parts. The first part, Section 1.3, investigates the 2D linear response of a realistic tropical atmosphere to a convective heat source of finite duration. The primary objectives are: 1) to understand how the morphology of the source influences the structure and energetics of the gravity waves that occur in response to the heating and, 2) to characterize the effects of these waves on the cloud environment, extending the work of LR01. The second part, Section 1.4, uses the FS85 vertical normal mode transform algorithm (described in the next section) to analyze output from a high-resolution 2D CRM simulation of an isolated cloud. A primary goal is to determine the extent to which the theoretical concepts outlined in Part I can be used to interpret the results of the simulation.

In addition to using Hovmoller diagrams of CAPE and CIN, the effect of the convectively generated gravity waves on the cloud environment is assessed here using diagrams of the precipitable water of the free troposphere (PW_{FT}), defined as the column-integrated mass of water vapor above 900 mb. Work by Sherwood (1999) serves to motivate our interest in the impact of deep convection on PW_{FT}. His observations provide evidence that the primary factor controlling the development of deep convection in the equatorial warm-pool region is the moisture content of the free troposphere.

2.2 The vertical normal mode transform

The following paragraphs review FS85's theory of the vertical normal mode transform. The application of the transform to a realistic tropical sounding is discussed thereafter.

2.2.1 Theory

We begin with a linearized system of equations describing small-amplitude motions of a 2D, fully compressible, and non-rotating atmosphere in hydrostatic balance, i.e.,

$$\frac{\partial u}{\partial t} = -\frac{\partial \phi}{\partial x} + F, \tag{2.1}$$

$$\frac{\partial \phi}{\partial p} + \frac{RT}{p} = 0 \ , \tag{2.2}$$

$$\frac{\partial u}{\partial x} + \frac{\partial \omega}{\partial p} = 0, \text{ and} \tag{2.3}$$

$$c_p \frac{\partial T}{\partial t} - \frac{p\sigma}{\kappa}\omega = Q. \tag{2.4}$$

Here, u is the horizontal velocity, p is the pressure, ω is the vertical p-velocity, ϕ is the geopotential, R is the dry air gas constant, T is the temperature, c_p is the specific heat of dry air at constant pressure, $\sigma = [p^{-2}(\kappa R\overline{T} - pdR\overline{T}/dp)]$ is the static stability parameter of the basic state, and, $\kappa = R/c_p$. For the purposes of the present discussion, we shall regard F and Q as specified momentum and diabatic forcing terms, respectively. Later on, these terms will be generalized to include the effects of non-linearities and subgrid-scale (SGS) turbulent transport processes.

The linearized upper and lower boundary conditions are given by

$$\omega = 0 \text{ at } p = p_T, \text{ and} \tag{2.5}$$

$$\frac{\partial \phi}{\partial t} - \frac{R\bar{T}\omega}{p} = 0 \text{ at } p = p_S, \tag{2.6}$$

respectively, where, p_T and p_S are the pressures at the top of the atmosphere and at the surface, respectively.

The goal of the theory is to eliminate the vertical structure from (2.1)-(2.6). To do this, we first eliminate T and ω from (2.2)-(2.4) to arrive at

$$L\left\{\frac{\partial \phi}{\partial t}\right\} + \frac{\partial u}{\partial x} = L\left\{\frac{\partial \Phi}{\partial t}\right\}, \tag{2.7}$$

where L is a vertical differential operator of the form

$$L = -\frac{\partial}{\partial p}\left[\frac{1}{\sigma}\frac{\partial}{\partial p}(.)\right] \text{ and,} \tag{2.8}$$

Φ is the "forced geopotential" that would result if the motion were constrained to be non divergent, i.e.,

$$-p\frac{\partial}{\partial p}\left(\frac{\partial \Phi}{\partial t}\right) = \kappa Q. \tag{2.9}$$

Similarly, using (2.2) and (2.4), we can write the boundary conditions as

$$B_T\left[\frac{\partial \phi}{\partial t} - \frac{\partial \Phi}{\partial t}\right] = B_S\left[\frac{\partial \phi}{\partial t} - \frac{\partial \Phi}{\partial t}\right] = 0, \tag{2.10}$$

where B_T and B_S are upper and lower boundary functionals that depend only on p.

To eliminate the L operator from (2.7), FS85 define a vertical integral transform operator of the form

$$VT[u(p)] = u_n = \langle u(p), \Psi_n(p) \rangle, \tag{2.11}$$

where $\Psi_n(p)$ is the transform kernel, and

$$\langle u(p), \Psi_n(p) \rangle \equiv \frac{1}{p_B - p_T} \int_{p_T}^{p_S} u(p) \Psi_n(p) dp \tag{2.12}$$

is a vertical inner product. Provided that: 1) $\Psi_n(p)$ is a solution of the vertical structure problem, given by

$$L\{\Psi_n(p)\} = \lambda_n \Psi_n(p) \text{ and} \tag{2.13}$$

$$B_T[\Psi_n(p)] = B_B[\Psi_n(p)] = 0, \tag{2.14}$$

where λ_n is a constant eigenvalue, and 2) the vertical structures of u and ϕ are seperable from the horizontal and temporal structures, FS85 show that (2.1) and (2.7) can be transformed to obtain:

$$\frac{\partial u_n}{\partial t} = -\frac{\partial \phi_n}{\partial x} + F_n \text{ and,} \tag{2.15}$$

$$\frac{\partial \phi_n}{\partial t} + \frac{1}{\lambda_n} \frac{\partial u_n}{\partial x} = \frac{\partial \Phi_n}{\partial t} \quad . \tag{2.16}$$

This system is formally equivalent to the shallow water equations when λ_n is written as $(gh_n)^{-1}$, where g is the acceleration due to gravity and h_n is the "equivalent depth" of the fluid.

As FS85 discuss, two important properties of the solutions to (2.13) and (2.14) are that: 1) the eigenvalues λ_n are real, and 2) the eigenfunctions $\Psi_n(p)$ are orthonormal in the inner product. The first property implies that we can define a real gravity wave phase speed, $c_n = (gh_n)^{1/2}$, associated with each vertical mode, while the second property allows the energetics of the nth mode to be expressed as

$$\frac{\partial}{\partial t}\left(\frac{1}{2}u_n^2+\frac{1}{2}\frac{\phi_n^2}{c_n^2}\right)=-\frac{\partial}{\partial x}(\phi_n u_n)+u_n F_n+\frac{\phi_n \partial \Phi_n}{c_n^2 \partial t}. \tag{2.17}$$

Here, $\frac{1}{2}u_n^2$ is the kinetic energy (KE_n), $\frac{1}{2}(\phi_n^2/c_n^2)$ is the available potential energy (APE_n), $-\frac{\partial}{\partial x}(\phi_n u_n)$ is the energy flux divergence, $u_n F_n$ is the eddy generation of KE_n due to momentum forcing, and finally, $\frac{\phi_n \partial \Phi_n}{c_n^2 \partial t}$ is the eddy generation of APE_n due to heating processes. Another important property of the eigenfunctions is that they form a complete set. This means that any function $\zeta(p)$ can be expanded as

$$\zeta(p) = \sum_{n=0}^{\infty} \zeta_n \Psi_n(p), \tag{2.18}$$

with uniform convergence provided that, $\zeta(p)$ satisfies the boundary conditions, and $d^2\zeta(p)/dp^2$ is continuous on the interval $[p_T, p_S]$. (2.18) represents the inverse vertical transform.

2.2.2 Application to a realistic sounding

The vertical structure problem can only be solved analytically for a few special cases, e.g. an atmosphere where σ = constant or where $p^2\sigma$ = constant. In the case of an observed sounding, FS85 use the Rayleigh-Ritz method to obtain an approximate solution expressed in terms of a weighted summation of N Chebychev polynomials. The authors show that the error in the numerical solution decreases by an order of magnitude as N is incrementally increased in the range 2- 16. They also point out that the aliasing of higher-

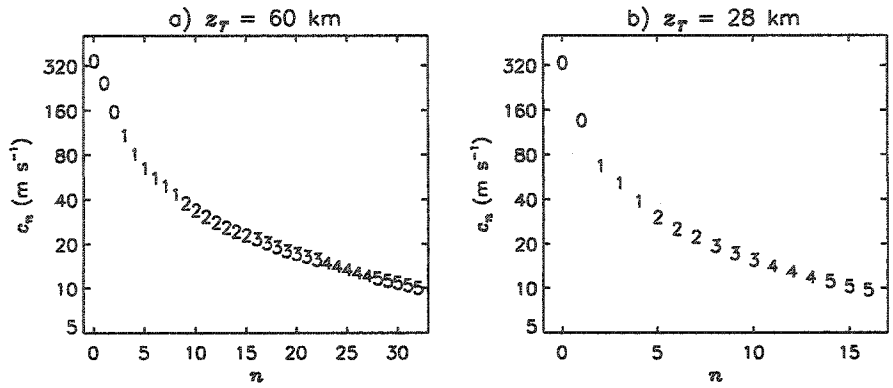

Figure 2.1 Eigenvalues c_n plotted as a function of n for a realistic GATE sounding with z_T = 60 km (a) and z_T = 28 km (b). The plotting symbols identify how many times the corresponding eigenfunction Ψ_n crosses the zero axis between the surface and the tropopause (14 km).

order modes on to lower-order modes is smallest when the observed sounding is sampled at levels equally spaced in log-p coordinates.

Fig. 2.1a shows the distribution of eigenvalues, plotted as a function of n, for an input temperature sounding based on conditions observed during the GARP (Global Atmospheric Research Program) Atlantic Tropical Experiment (GATE). Note that the sounding was interpolated onto a 1024-level grid (equally spaced in log-p) with p_T = 0.47 mb, z_T = 60 km and N = 128. Above 48 mb (the highest level recorded during GATE), the temperature profile was specified using the standard tropical atmosphere of McClatchey *et al.* (1972).

The plotting symbols in Fig. 2.1a identify how many times the corresponding eigenfunction crosses the zero axis between the surface and the tropopause. Thus, the set of Ψ_ns with eigenvalues in the range, 38-100 m s^{-1}, corresponds to a band of first internal modes, while, those with c_ns between 20-38 and 13-20 m s^{-1} are bands of second internal

and third internal modes, respectively. The implication is that Ψ_ns with relatively deep vertical structures propagate faster than those with shallower vertical structure. This is analogous to hydrostatic gravity waves in an infinitely deep and uniformly stratified atmosphere, where the horizontal phase speed of the waves is linearly proportional to the vertical wavelength (e.g. Holton, 1972). Of course, in the latter case, the eigenfunctions are simple sinusoids, while here they are not.

The solid lines in Fig. 2.2a-d depict the vertical structure of four different Ψ_ns with phase speed c_n = 48, 21, 16, and 13 m s^{-1}, respectively. In each case, we see a series of relatively smooth oscillations whose characteristic depth and amplitude increase dramatically as one moves upwards across the tropopause. The dashed curves in Figure 1.4a-d depict the structure of Ψ_ns with similar eigenvalues to those of the solid curves but with z_T lowered from 60 to 28 km. Although the amplitudes of the oscillations in the dashed curves are larger, owing to the orthonormality condition, their shapes are nearly identical to those of the solid curves.

While the eigenvalues and shapes of the eigenfunctions show little sensitivity to changes in the depth of the atmosphere, a comparison of Figs. 2.1a and b shows that the density of eigenvalues decreases by roughly a factor of two when z_T is decreased by the same amount. Since the Ψ_ns can be regarded as states of the atmosphere in which the ratio of the APE_n to KE_n is minimized (FS85), Fig 2.2 implies that decreasing the depth of the atmosphere reduces the number of these "minimum" energy states.

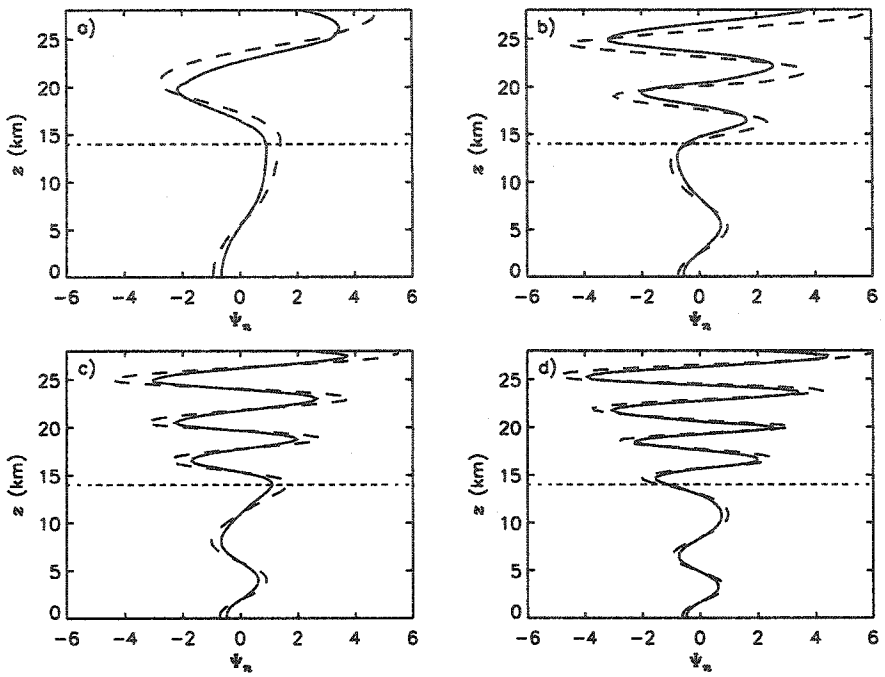

Figure 2.2 Vertical structure of various eigenfunctions Ψ_n computed from the GATE sounding with z_T = 60 km (solid curves) and z_T = 28 km (dashed curves). The eigenvalues for the solid (dashed) curves in a)-d) are given by 48 (48), 21 (20), 16 (16), and 13 (13) m s^{-1}, respectively. The horizontal dotted line denotes the level of the tropopause

2.3 The linear gravity wave response to a deep convective heat source

Which of the above vertical normal modes are most efficiently excited by an isolated deep convective cloud, and how do these modes impact the CAPE, CIN, and PW_{FT} of the cloud environment? Here, we answer this question analytically by assuming a stationary convective heat source of the form

$$Q(x,z,t) = \frac{J_0}{\tau}\left(\frac{a^2}{a^2+x^2}\right)\Omega(z)\{H(t)-H(t-\tau)\}, \tag{2.19}$$

where J_0 is the net heat input per unit mass, τ is the duration of the heating, a is the half-width of the source, and $H(t-t_0)$ is the Heaviside (step) function, defined as

$$H(t-t_0) = 0, \text{ for } t < t_0, \text{ and} \tag{2.20}$$

$$H(t-t_0) = 1, \text{ for } t \geq t_0. \tag{2.21}$$

The vertical structure of the heating is specified as

$$\Omega(z) = \left\{ \sin\left[\pi \frac{z-z_1}{z_2-z_1} \right] \right\}^2 \cdot \{H(z-z_1) - H(z-z_2)\}, \tag{2.22}$$

where z_1 is the base of the source and z_2 is its top. Unless otherwise stated, the heating parameters are given by $J_0 = 1 \times 10^4$ J kg^{-1}, $a = 5$ km, $\tau = 0.5$ hrs, $z_1 = 1$ km and $z_2 = 14$ km - chosen to represent a relatively narrow deep convective core with a maximum precipitation rate of 30 mm hr^{-1}.

Using Fourier and Laplace transforms, Nicholls et al. (1991) showed that the linear response to (2.19), for an individual vertical normal mode, consists of pair of gravity wave packets that radiate in either direction from the source at speed c_n. The following paragraphs demonstrate that an identical solution can be obtained using the method of characteristics.

2.3.1 Derivation of the solution

Because the vertical structure of Q is separable from its horizontal and temporal structures, we can immediately write the governing equations as

$$\frac{\partial u_n}{\partial t} + \frac{\partial \phi_n}{\partial x} = 0 \text{ and} \tag{2.23}$$

$$\frac{\partial \phi_n}{\partial t} + c_n^2 \frac{\partial u_n}{\partial x} = \frac{\kappa J_0}{\tau} \left(\frac{a^2}{a^2 + x^2} \right) \Omega_n \{H(t) - H(t-\tau)\}, \tag{2.24}$$

where the effects of momentum forcing have been neglected and

$$\Omega_n = \langle \int_{\ln p}^{\ln p_S} \Omega d\ln p, \Psi_n(p) \rangle \tag{2.25}$$

is the projection of the vertical profile of $\partial\Phi/\partial t$. Introducing the non-dimensional variables,

$$X_n = (u_n/c_n + \phi_n/c_n^2) \text{ and,} \tag{2.26}$$

$$Y_n = (u_n/c_n - \phi_n/c_n^2), \tag{2.27}$$

(2.22) and (2.23) can be combined to obtain the following pair of ordinary differential equations,

$$\frac{\partial X_n}{\partial t} = \frac{\kappa J_0}{\tau}\left(\frac{a^2}{a^2 + (\xi_{n-} + c_n t)^2}\right)\Omega_n\{H(t) - H(t-\tau)\} \text{ and} \tag{2.28}$$

$$\frac{\partial Y_n}{\partial t} = -\frac{\kappa J_0}{\tau}\left(\frac{a^2}{a^2 + (\xi_{n+} - c_n t)^2}\right)\Omega_n\{H(t) - H(t-\tau)\}, \tag{2.29}$$

where $\xi_{n-} = x - c_n t$ and $\xi_{n+} = x + c_n t$ are the two characteristic lines of the system. Integrating these expression forward in time leads to the solution pairs,

$$X_n(x,t) = \frac{\kappa J_0 a \Omega_n}{c_n^3 \tau}\left[\text{atan}\left(\frac{x}{a}\right) - \text{atan}\left(\frac{x - c_n t}{a}\right)\right] \text{ for } 0 \le t \le \tau, \text{ and} \tag{2.30}$$

$$X_n(x,t) = \frac{\kappa J_0 a \Omega_n}{c_n^3 \tau}\left[\text{atan}\left(\frac{x - c_n t^*}{a}\right) - \text{atan}\left(\frac{x - c_n t}{a}\right)\right] \text{ for } t > \tau, \tag{2.31}$$

and

$$Y_n(x,t) = \frac{\kappa J_0 a \Omega_n}{c_n^3 \tau}\left[\text{atan}\left(\frac{x}{a}\right) - \text{atan}\left(\frac{x + c_n t}{a}\right)\right] \text{ for } 0 \le t \le \tau, \text{ and} \tag{2.32}$$

$$Y_n(x,t) = \frac{\kappa J_0 a \Omega_n}{c_n^3 \tau}\left[\text{atan}\left(\frac{x + c_n t^*}{a}\right) - \text{atan}\left(\frac{x + c_n t}{a}\right)\right] \text{ for } t > \tau, \tag{2.33}$$

where atan() is the inverse tangent and $t^* = t - \tau$. The upper and lower pairs of solutions describe information moving to the right and left, respectively, at speed c_n.

Using (2.24) and (2.25) along with (2.28)-(2.31), the solutions for the geopotential and horizontal velocity perturbations of the nth mode can be written as

$$\phi_n(x, p, t) = \frac{\kappa J_0 a \Omega_n}{2 c_n \tau} \Psi_n(p) \cdot \{\Pi_n(x, t) \cdot H(t) - \Pi_n(x, t^*) \cdot H(t^*)\} \text{ and} \tag{2.34}$$

$$u_n(x, p, t) = \frac{\kappa J_0 a \Omega_n}{2 c_n^2 \tau} \Psi_n(p) \cdot \{\Pi^*_n(x, t) \cdot H(t) - \Pi^*_n(x, t^*) \cdot H(t^*)\}, \tag{2.35}$$

respectively, where

$$\Pi_n(x, t) = \text{atan}\left(\frac{x + c_n t}{a}\right) - \text{atan}\left(\frac{x - c_n t}{a}\right) \text{ and} \tag{2.36}$$

$$\Pi^*_n(x, t) = \text{atan}\left(\frac{x + c_n t}{a}\right) - \text{atan}\left(\frac{x - c_n t}{a}\right) + 2\,\text{atan}\left(\frac{x}{a}\right). \tag{2.37}$$

The solutions for the remaining field variables including the water vapor mixing ratio[1], r_n, are given by

$$\omega_n(x, p, t) = \frac{\kappa J_0 \Omega_n}{c_n^2 \tau} \chi_n(p) \cdot \{\Gamma_n(x, t) \cdot H(t) - \Gamma_n(x, t^*) \cdot H(t^*)\}, \tag{2.38}$$

$$T_n(x, p, t) = -\frac{J_0 a \Omega_n}{2 c_p c_n \tau}\left[\frac{d}{d \ln p}(\Psi_n p)\right] \cdot \{\Pi_n(x, t) \cdot H(t) - \Pi_n(x, t^*) \cdot H(t^*)\}, \text{ and} \tag{2.39}$$

$$r_n(x, p, t) = -\frac{\kappa J_0 a \Omega_n}{c_n^3 \tau} \chi_n(p) \frac{d}{dp} \tilde{r} \cdot \{\Gamma^*_n(x, t) \cdot H(t) - \Gamma^*_n(x, t^*) \cdot H(t^*)\}. \tag{2.40}$$

---

1. The solution for r_n was obtained by forward time integration of the linearized statement expressing conservation of r in the absence of phase changes.

Here,

$$\chi_n(p) = \int_{p_T}^{p} \Psi_n(p)dp, \tag{2.41}$$

$$\Gamma_n(x,t) = \frac{a^2}{a^2+x^2} - \frac{1}{2}\left(\left[1+\left(\frac{c_n t+x}{a}\right)^2\right]^{-1} + \left[1+\left(\frac{c_n t-x}{a}\right)^2\right]^{-1}\right), \text{ and,} \tag{2.42}$$

$$\Gamma^*_n(x,t) = \left(\frac{c_n t}{a}\right)\frac{a^2}{a^2+x^2} - \frac{1}{2}\Pi(x,t). \tag{2.43}$$

(2.32)-(2.41), when summed over n, describe the linear hydrostatic response of an inviscid, initially motionless, non-rotating atmosphere to a finite duration convective heat source given by (2.19). A discussion of this response is given below.

2.3.2 Properties of the solution

Figs. 2.3a-c depict the horizontal structures of ϕ_n, u_n, and ω_n in the lower troposphere at $t = \tau$, 2τ, and 3τ, respectively, with $c_n = 52$ m s^{-1}. Note that the solutions have been normalized by their maximum respective values at $t = \tau$. Just after the heating is switched off, we see a relatively broad minima in ϕ_n stretching across the central 180 km of the domain with correspondingly broad inflow to either side. The horizontal structure of ω_n, on the other hand, shows a relatively narrow minimum in the center of the domain, matching the spatial structure and location of the heating and two positive peaks located at $x \approx \pm 95$ km. Later on, these fields have "separated" into two spatially localized gravity wave packets moving in opposite directions from the source at speed c_n. There is rising (sinking) motion at the leading (trailing) edge of both packets and low geopotential anom-

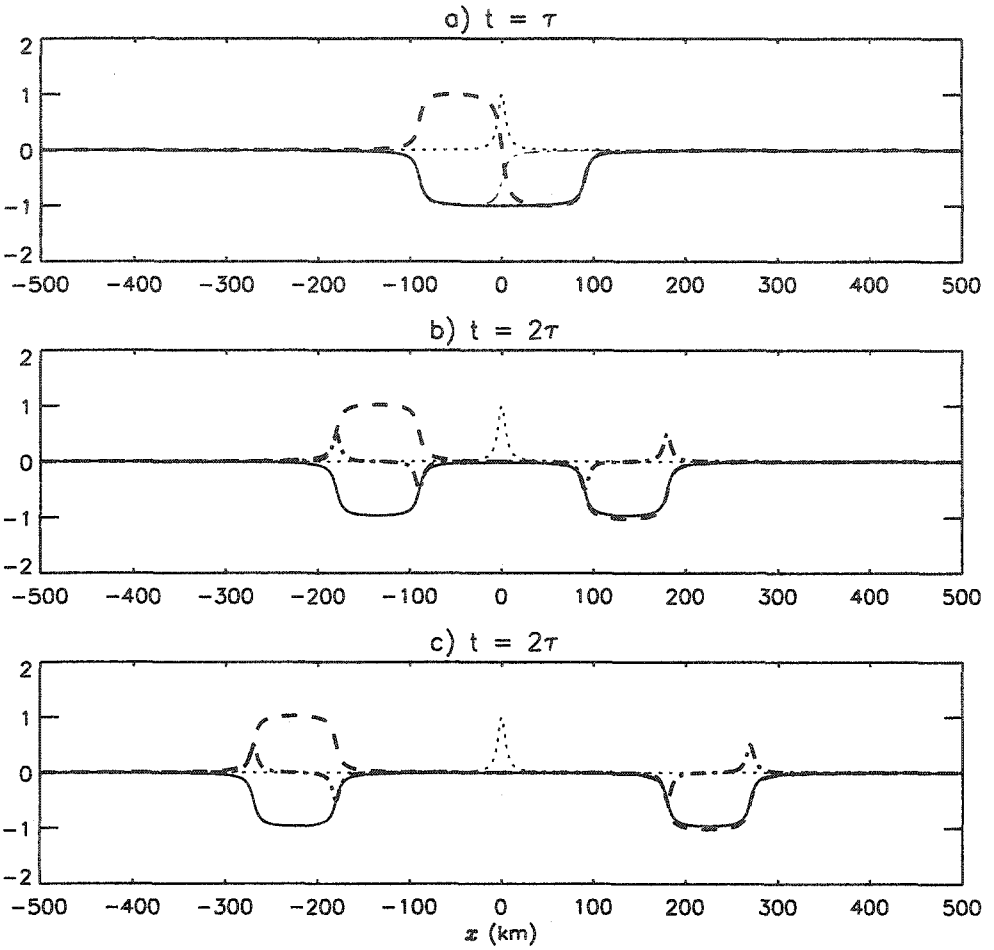

Figure 2.3 Snapshots of ϕ_n (solid line), u_n (dashed line), and ω_n (dash-dotted line) in the lower troposphere at $t = 1$ (a), 2 (b), and 3 τ (c) for the case where, $\tau = 0.5$ hr, $a = 5$ km, and $c_n = 48$ m s^{-1}. The amplitudes of all fields are normalized by their maximum absolute values at $t = \tau$. The dotted line depicts the normalized amplitude of the heating, switched on at $t = 0$ and switched off at $t = \tau$.

alies at their centers. The characteristic horizontal scale of the each packet is roughly 180 km and their amplitudes remain constant with time.

Inspection of the far-field solution for the geopotential anomalies, i.e., (2.32) for $t > \tau$, shows that the expressions for the half-width and maximum amplitude of the nth gravity wave packet are given by

$$b_n = a\sqrt{1+\left(\frac{c_n}{c_Q}\right)^2} \text{ and} \tag{2.44}$$

$$\phi_n^{max} = \frac{\kappa J_0 \Omega_n}{2} \frac{c_Q}{c_n} \left[\operatorname{atan}\left(\frac{c_n}{c_Q}\right) \right], \tag{2.45}$$

respectively, where $c_Q \equiv 2a/\tau$ is a characteristic phase speed associated with the heated region. Taking the limit as $\tau \to 0$ (corresponding to impulsive heating), we find that the packet takes on the shape of the heated region with $\phi_n^{max} = \kappa J_0 \Omega_n / 2$. On the other hand, when $a = 5$ km and $\tau = 0.5$ hrs, Figs. 2.4a and b shows that the slower moving packets are relatively broad and weak, while the faster moving packets are relatively narrow and intense. A simple explanation of this result is that the faster (slower) moving packets propagate out of the heated region more quickly (slowly) and, thus, have less (more) of an opportunity to experience the effects of the heating.

After the heating is switched off, inspection of (2.17) shows that the domain integrated energy within each vertical normal mode, i.e.,

$$\int_{-\infty}^{\infty} E_n(x,t)dx = \int_{-\infty}^{\infty} \{KE_n(x,t) + APE_n(x,t)\}dx, \tag{2.46}$$

is conserved for all time. Substitution of the far-field solutions for the horizontal wind and geopotential anomaly into (2.46) yields

$$[E_n] = \frac{c_Q^2}{2c_n^2}\left(\frac{\kappa J_0 \hat{\Omega}_n}{c_n}\right)^2 [\Pi_n{}^2 + \Pi^*{}_n{}^2] \text{ for all } t > \tau, \tag{2.47}$$

where the brackets hereafter denote a domain integrated quantity. In the limit as $\tau \to 0$, this expression becomes

$$\lim_{\tau \to 0}[E_n] = \frac{1}{2c_n^2}(\kappa J_0 \hat{\Omega}_n)^2 \left[\left(\frac{a^2}{a^2 + x^2}\right)^2\right] \text{ for all } t > 0. \tag{2.48}$$

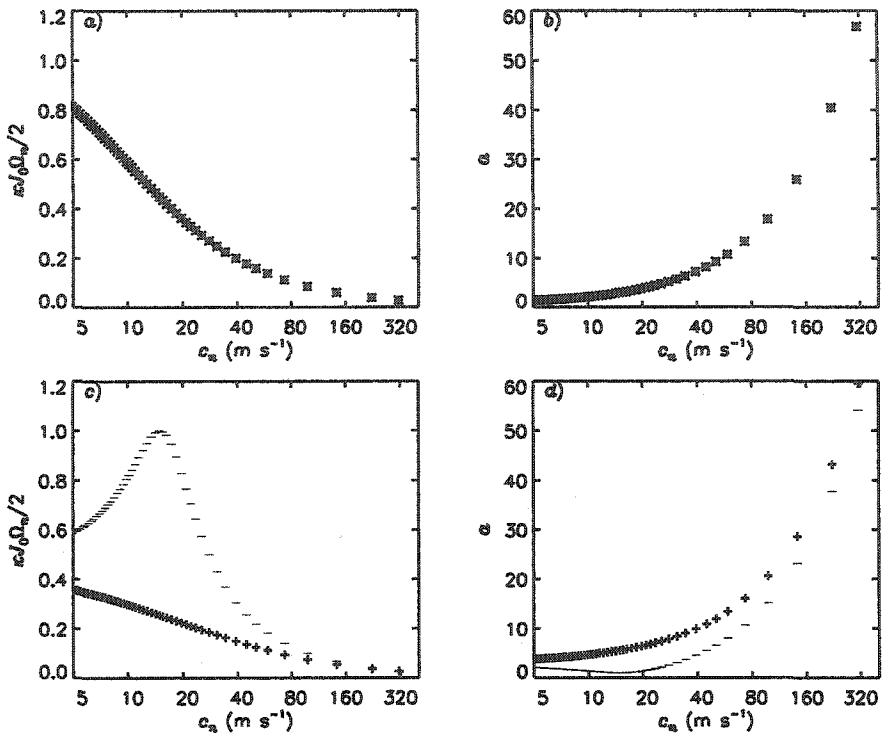

Fig 2.4 Amplitude (a and c) and half-width (b and d) of gravity wave packets excited by a convective heat source with a = 5 km and τ = 0.5 hrs. The top two panels are for a stationary heat source. The bottom two panels are for a heat source that translates steadily at speed u_t = 15 m s^{-1}, where, the '+' ('-') symbols denote gravity wave packets propagating in the opposite (same) direction to that of the heat source.

Since $\kappa J_0 \Omega_n = \int_0^\infty \frac{\partial \Phi_n}{\partial t} dt$, (2.45) implies that the quantity, $\left(\frac{1}{c_n}\frac{\partial \Phi_n}{\partial t}\right)^2$, will give the partitioning of energy among the various modes, provided that the heating is impulsive.

The solid and dotted curves in Fig. 2.5c depict the far-field spectra of $[E_n]$ generated by a source with τ = 0.5 hrs and by a source in the limit as $\tau \to 0$, respectively. Note that the spectra have been normalized by the maximum value of $\lim_{\tau \to 0}[E_n]$. The two spectra appearing in Fig. 2.5c both show that most of the energy is contained within two relatively narrow bands: a primary band centered at 48 m s^{-1} and a secondary band centered at

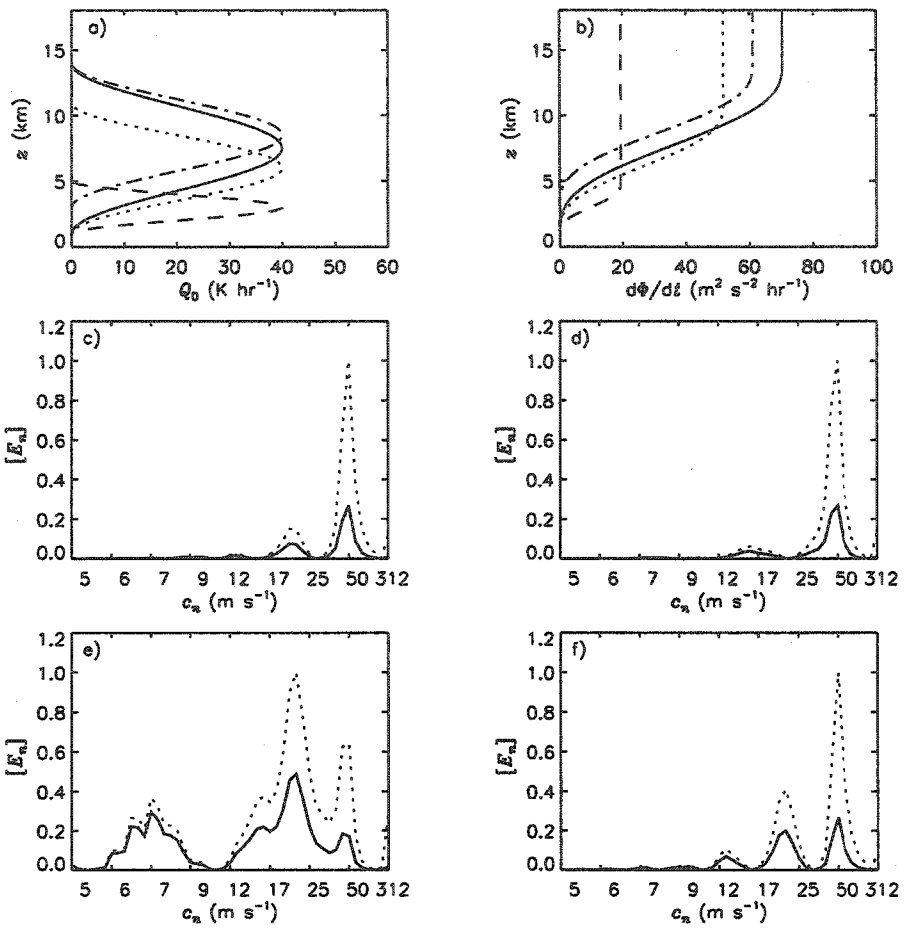

Figure 2.5 Normalized far-field spectra of $[E_n]$, generated by a convective heat source with a = 5 km and vertical structure given by either the solid (c), dotted (d), dashed (e), or dot-dashed curves (f) appearing in a). The spectra given by the solid are for finite duration heating with $\tau = 0.5$ hrs while, those given by the dotted curves are for impulsive heating. Note that both spectra have been normalized by the maximum value of $\lim_{\tau \to 0} [E_n]$.

21 m s^{-1}. Because the difference in amplitude between the two bands is smaller in the case of the solid curve, we can conclude that the heat source of finite duration is relatively more efficient at generating energy in higher-order modes. This can be explained by the fact that the higher-order modes spend a greater amount of time in the heated region and, thus, have a greater opportunity to experience eddy generation of APE_n.

Figs. 2.5d-f show how the partitioning of the energy changes when $\Omega(z)$ is modified while all other parameters are held fixed. Decreasing z_2 from 14 to 11 km, Fig 2.5c shows that the location of the secondary band shifts downward to about 16 m s^{-1}, while, the location of the primary band remains unchanged. This downward shift of the secondary band is important because, as demonstrated in the next section, the impact of the 21 m s^{-1} and 16 m s^{-1} modes on the CAPE is different. When z_2 is decreased to a typical congestus top-height (i.e., 5 km), Fig 2.5e shows that the widths of the primary and secondary bands each increase and that their peaks shift "downwards" to roughly 21 and 8 m s^{-1}, respectively. On the other hand, when z_2 is held fixed at 14 km while z_1 is increased from 1 to 3 km (Fig 2.5f), we see a substantial increase in the energy of the 21 m s^{-1} band and also, the emergence of a tertiary band at 13 m s^{-1}.

2.3.3 CAPE, CIN, and PW_{FT}

The solutions for the temperature and water vapor perturbations (when summed over n) can be used to construct Hovmoller diagrams that illustrate how CAPE, CIN, and PW_{FT} fluctuate in space and time. Figs 2.6a-c are examples of such diagrams - constructed for the source with z_1 = 1 and z_2 = 14 km. Note that, throughout this study, values of CAPE and CIN are calculated, assuming pseudo-adiabatic ascent, as averages over all parcel origin-levels between the surface and 500 m.

The passage of the 48 and 21 m s^{-1} modes are both clearly evident in Figs. 2.6a-c. The 48 m s^{-1} mode appears as a 90 km wide region where values of CAPE and PW_{FT} are depressed by ~ 30% and 10%, respectively, from their background value, while CIN is

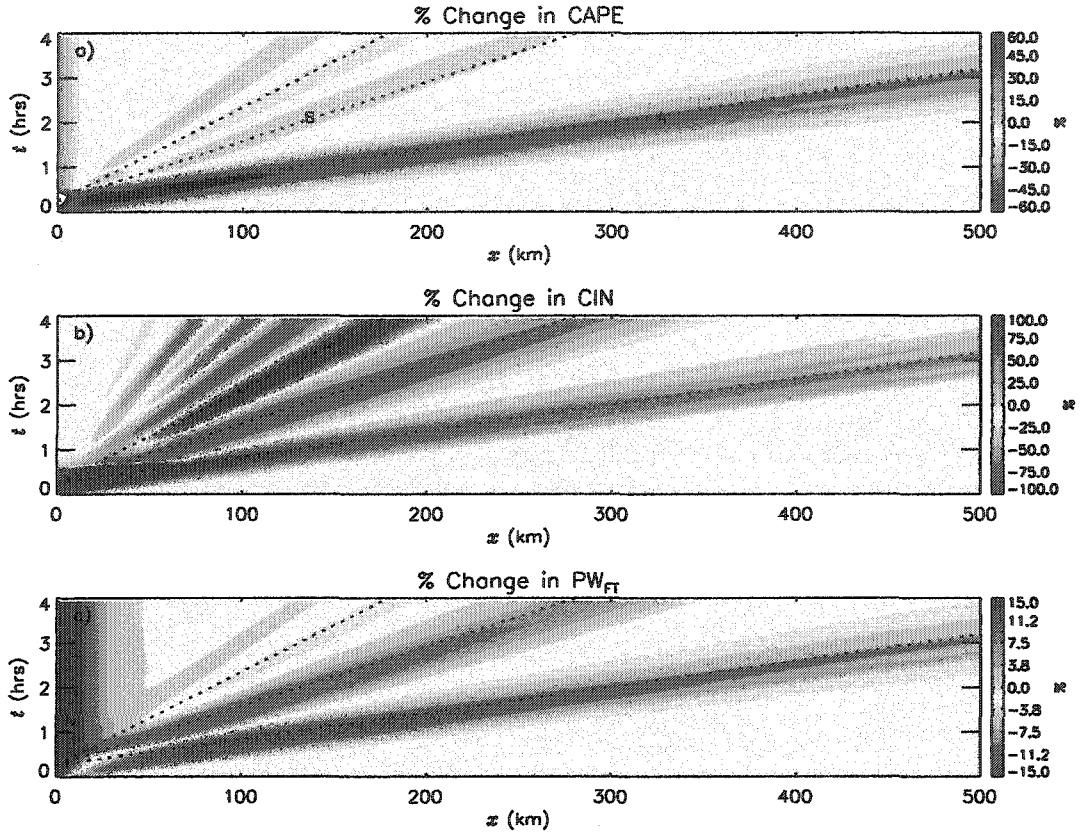

Figure 2.6 Hovmoller diagrams of fluctuations in CAPE (a), CIN (b), and PW_{FT} (c) resulting from a convective heat source with $J_0 = 2.5 \times 10^4$ J kg^{-1}, $a = 5$ km, $\tau = 0.5$ hrs, $z_1 = 1$ km, and $z_2 = 14$ km. Results are plotted as percentage changes relative to the following background values: CAPE = 1880 J kg^{-1}, CIN = 2 J kg^{-1}, and $PW_{FT} = 35$ kg m^{-2}. The dotted lines in each diagram denote phase speeds of 48, 21, and 13 m s^{-1} Profiles of temperature and water vapor perturbations at locations A and B are shown in Figure 2.7a and b, respectively.

enhanced by about 50%. The 21 m s^{-1} mode, on the other hand, appears as a 40 km wide region with depressed values of CIN and enhanced amounts of PW_{FT}. The CAPE remains largely unaffected by this mode. As alluded to the in introduction, we see that the low-level cooling and moistening effects of the 21 m s^{-1} mode do not become apparent until after the heating is switched off.

In addition to the 48 and 21 m s^{-1} modes, Fig 2.6b shows evidence for the excitation of a series of higher-order modes with the sign of the low-level temperature perturbations reversed from one mode to the next. Even though these modes carry negligible amounts of energy (Fig 2.5c), they still have a significant impact on the low-level temperature field and thus, CIN. They have little effect on quantities involving deep tropospheric averages (i.e., CAPE and PW_{FT}), however, since the vertical averaging process tends to cancel out their high-frequency oscillations.

Fig. 2.7 is similar to Fig. 2.6 but with z_2 lowered from 14 to 11 km. In this case, it is the 16 m s^{-1} mode, rather than the 21 m s^{-1} mode, that acts to lower the CIN while increasing PW_{FT}. Importantly, however, the 16 m s^{-1} mode also acts to increase the CAPE by as much as 10%.

To help explain these differences, Figure 2.8 shows soundings of T and r at the locations A and B in Figure 2.6a and C in Figure 2.7a (referred to as Soundings A-C, respectively, in the following discussion). Sounding A, representative of the 48 m s^{-1} mode, shows the effects of deep subsidence warming and drying with a peak amplitude of 2 K at a height of roughly 5 km. This warming and drying leads to a decrease in both the CAPE and PW_{TR} and an increase in CIN. Sounding B, representative of the 21 m s^{-1} mode, shows the effects of rising motion at low-levels and sinking motion aloft. Importantly, although the magnitudes of the upper and lower level temperature perturbations are comparable to one another, we see that the magnitudes of the moisture perturbations are not. This explains why the 21 m s^{-1} mode, a second internal mode, can promote enhanced (suppressed) amounts of PW_{TR} (CIN) while leaving the CAPE virtually unchanged. Sounding

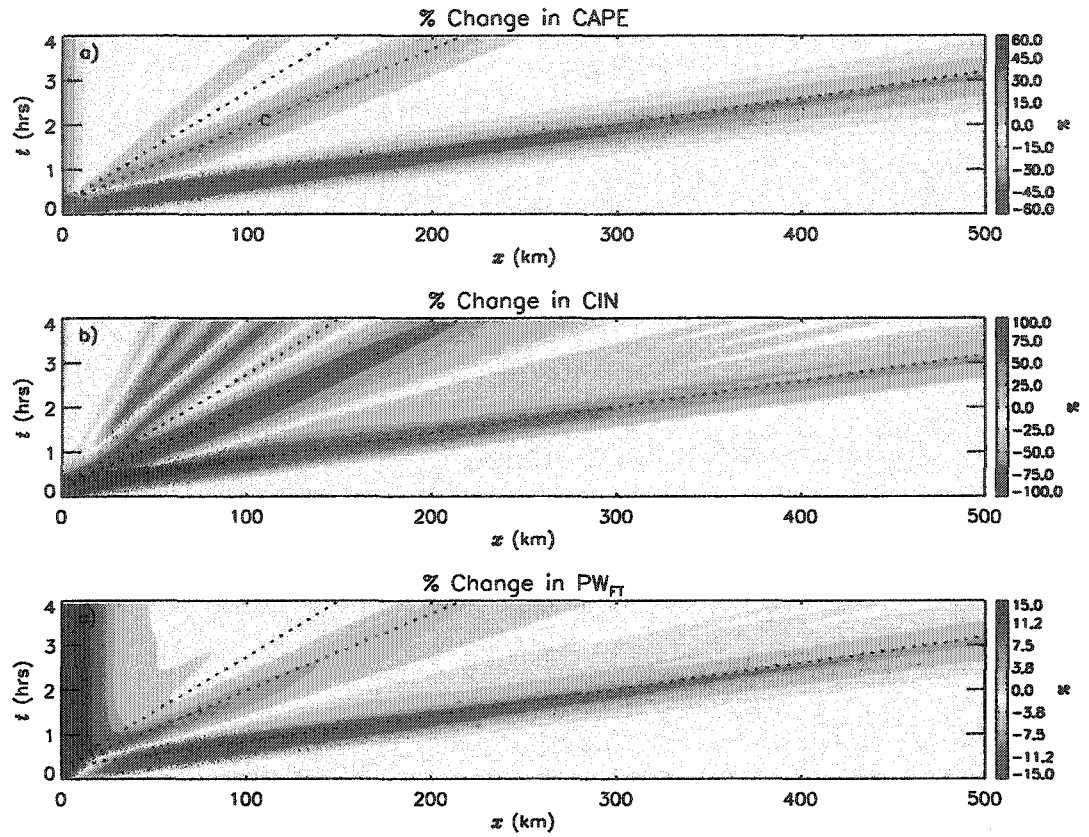

Figure 2.7 Similar to Fig. 2.6 but with z_2 decreased to 11 km. The dotted lines denote phase speeds of 48, 16, and 11 m s^{-1}.

C, representative of the 16 m s^{-1} mode, shows a moisture profile similar to sounding B although the magnitude of the upper level drying is somewhat greater. Unlike Sounding B, however, Sounding C also shows net cooling of both the upper- and lower-troposphere. This explains why the 16 m s^{-1} mode (a third internal mode) can act to increase both the CAPE and PW_{TR}, while decreasing the CIN.

2.3.4 The effects of steady translation

The discussion thus far has focused on a localized heat source that is fixed in space. In reality, however, convection can propagate relative to the background flow through internal storm dynamics. To understand the effects of this propagation on gravity wave genera-

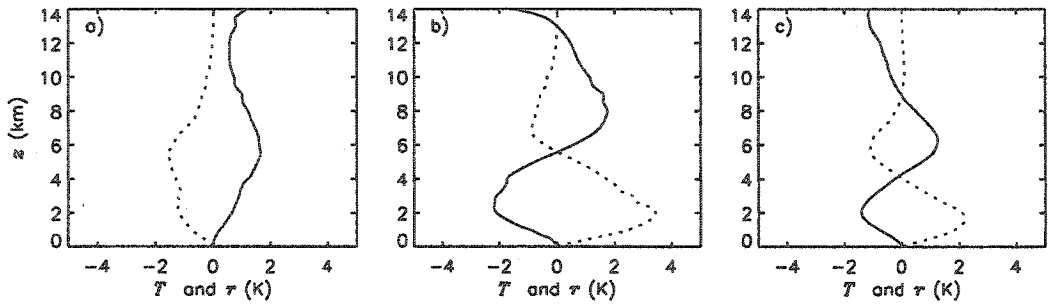

Figure 2.8 Profiles of T (solid line) and r (dotted line, plotted in equivalent temperature units) at points A (a) and B (b) in Fig. 2.6a and at point C (c) in Fig. 2.7a.

tion, we assume here that the convective heat source translates steadily at speed u_t. The far field expressions for the half-width and maximum amplitude of the convectively generated gravity wave packets are then given by

$$b_{n+/-} = a\sqrt{1+\left(\frac{c_n \pm u_t}{c_Q}\right)^2} \text{ and} \tag{2.49}$$

$$\phi_{n+/-}^{max} = \frac{\kappa J_0 \Omega_n}{2}\frac{c_Q}{c_n \pm u_t}\left[\text{atan}\left(\frac{c_n \pm u_t}{c_Q}\right)\right], \tag{2.50}$$

where, the '+' ('-') symbol denote packets moving in the same (opposite) direction as the source.

Figs. 2.4c and d depict (2.47) and (2.48), respectively, plotted as a function c_n, for the case where u_t = 15 m s^{-1}, a = 5 km and τ = 0.5 hrs. Packets moving with the source are relatively narrow and intense while those moving against the source are relatively broad and weak. Analogous to impulsive heating, we see that packets moving in the same direction and at close to the same speed of the source, take on the shape of the heated region with ϕ_{n-}^{max} approaching $\kappa J_0 \Omega_n / 2$. This can be explained by the fact that packets travelling in

the same (opposite direction) to the source remain in the heated region for a greater (shorter) period of time.

2.3.5 Summary and Discussion

The preceding section examined the 2D linear response of a realistic tropical atmosphere to a convective heat source of finite duration. In agreement with previous studies, it was shown that the response consists of a spectrum of horizontally propagating gravity wave packets that radiate from the source at different speeds. The half-width, maximum amplitude, and energy of the packet was found to be controlled by the amount of time the packet spends in the heated region, as well as the vertical profile of the heating. In the case of deep convective heating profiles, it was shown that most of the energy is contained within a 48 m s^{-1} mode and either a 21 m s^{-1} or 16 m s^{-1} mode, depending on the depth of the heating.

The effects of the gravity wave packets on the cloud environment were assessed using Hovmoller diagrams of CAPE, CIN, and PW_{FT}. The 48 m s^{-1} mode appeared as region of enhanced CIN and reduced CAPE and PW_{FT}. The 21 and 16 m s^{-1} modes, on the other hand, appeared as a region of enhanced (reduced) PW_{FT} (CIN). Owing to a net cooling of the troposphere, the 16 m s^{-1} mode also increased the CAPE by ~ 10%. These results provide further evidence that an isolated deep convective cloud tends to create a region in its vicinity where conditions are favorable for further convective development. Here, it was shown that the size of this region depends on the duration of the heating as well as its speed of translation. It was also shown that this region does not emerge until *after* the heating is switched off.

Why does an isolated deep convective heat source cause low-level cooling and moistening in its surroundings? We can address this question by considering the linear response of an infinitely deep and uniformly stratified atmosphere to a source with vertical structure given by $\Omega(z) = \sin(\pi z/z_2) \cdot \{H(z)-H(z-z_2)\}$. As demonstrated by Mapes (1999), the vertical modes in this case are simple sinusoids and the vertical spectrum of the heating is given by

$$\Omega_{n^*} = \int_0^{\Theta} \sin\phi \sin(n^*\Theta) d\phi = \frac{I|_0^{\phi}}{\pi}. \tag{2.51}$$

Here, n^* is a continuos mode index ranging from 0 to ∞, where $I = \pi/2$ for $n^* = 1$ and $I = \frac{\sin[(n^*-1)\Theta]}{2(n^*-1)} - \frac{\sin[(n^*+1)\Theta]}{2(n^*+1)}$ otherwise. When the atmosphere is bounded by a rigid lid, (2.53) still holds true but the spectrum of the heating is a discrete Fourier expansion.

The solid curve in Fig. 2.9, shows the continuous version of (2.51), normalized by Q_0/π, for the parameter choices: $N_B = 0.01$ s^{-1} and $z_2 = 10$ km, where N_B is the Brunt-Vaisalla frequency. The spectrum shows positive values for c_n greater than about 17 m s^{-1} and negative values in the range 10-17 m s^{-1}. The peak projection response to the heating occurs at a speed of about 40 m s^{-1} (corresponding to a vertical wavelength of about $2.5 \times z_2$), while the secondary projection response occurs at a speed of about 13 m s^{-1} (corresponding to a vertical wavelength of about $0.85 \times z_2$). The sign of the spectrum gives information about the vertical structure of the solution: positive (negative) values imply warming (cooling) near the surface. Thus, Fig. 2.9 implies that, sometime after the

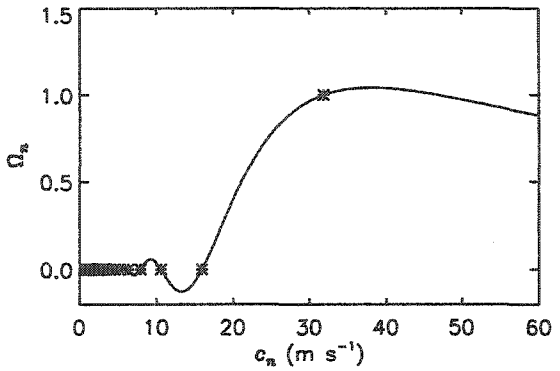

Figure 2.9 Continuous (solid curve) and discrete (plotting symbols) spectra of a deep convective heat source embedded in a uniformly stratified atmosphere, where $\sigma = 0.01$ s^{-1} and $z_2 = 10$ km. The continuous spectra is derived for an infinitely deep atmosphere, while the discrete spectra is for an atmosphere with a rigid lid placed at z_2.

heating is switched, there will develop a region in the vicinity of the source where conditions are favorable for additional convective development.

The plotting symbols in Fig. 2.9 represent the discrete version of (2.53) with $z_T = 10$ km. In this case, the spectrum is non-zero at 31 m s^{-1} and zero otherwise. Apparently, the presence of the rigid lid eliminates the region of low-level ascent induced by the heating. Because the presence of the rigid lid also eliminates the vertical propagation of gravity wave energy, this suggests that the former is related to the latter.

2.4 Numerical simulation of an isolated cloud

An obvious limitation of the preceding analysis is that it is based on linear hydrostatic theory, even though cumulus clouds are both non-linear and non-hydrostatic phenomena. The vertical profile of the heating was also assumed rather than being explicitly calculated.

This section uses a high-resolution 2D CRM to simulate the gravity wave response of a stably stratified atmosphere to an isolated deep convective cloud. The primary objective is to determine the extent to which the theoretical concepts outlined in Sections 2.2 and 2.3 can be used to interpret the results of the simulation. The following paragraphs offer brief descriptions of the numerical model, the experimental setup, and the model analysis-strategy. Results are presented thereafter.

2.4.1 Numerical model

The CRM (described in Khairoutdinov and Randall 2003) is based on an anelastic, i.e., soundproof, system of equations that is suitable for the description of deep moist convection relative to a horizontally uniform hydrostatic reference state. The prognostic variables are the Cartesian components of the velocity vector ($\underset{\sim}{u} = u\hat{i} + w\hat{k}$), the mixing ratio of non-precipitating water (r_{np}), the mixing ratio of precipitating water (r_p), and the liquid/ice water static energy, ($h_l = c_p T + gz - L_c(r_{liq}) - L_s(r_{frz})$, where, $T = T' + \overline{T}$ now refers to the total temperature, L_c and L_s are the latent heat of evaporation and sublimation, respectively, r_{liq} is the mixing ratio of liquid water (cloud water + rain), and r_{frz} is the mixing ratio of frozen water substance (ice + graupel + snow).

The model equations are solved on an Arakawa C-type grid with periodic lateral boundary conditions and rigid lid conditions imposed at the upper and lower boundaries. The advection of momentum is computed using a second-order finite difference scheme that conserves the domain averaged kinetic energy. Scalar advection is computed using the positive definite and monotonic scheme of Smolarkiewicz and Grabowski (1990). Time-stepping is performed using the third-order Adams-Bashforth scheme. The perturbation

pressure field is diagnosed at each time step using a fast fourier transform and a tridiagonal matrix solver.

The SGS turbulent fluxes are parameterized using a simple Smagorinsky-type closure, with the turbulent mixing coefficient taken to be proportional to the square of the local *vertical* grid spacing (note: this ensures that the model does not produce excessive vertical mixing in regions where the vertical grid spacing is much smaller than the horizontal grid spacing). The primary assumptions in the model's bulk microphysics parameterization are as follows.

1) The number concentration of each hydrometeor species is distributed with size according to Marshall and Palmer (1948).

2) The terminal velocity of precipitating hydrometeor particles are proportional to the size of the particle raised to a constant coefficient that depends on the type of hydrometeor.

3) The rate of evaporation of precipitating hydrometeor particles is proportional to the saturation deficit, modulo a "ventilation factor", with the magnitude of the ventilation depending on the size and type of the hydrometeor, as well as the temperature of its surroundings.

4) The collection of cloud condensate of type l by precipitating hydrometeor particles of type m is proportional to the square of the size precipitation particle and a constant collection efficiency factor, E_{ml}.

5) The autoconversion of cloud water/ice into precipitation is proportional to r_l-r_{l0}, where, $l = c$ (cloud water) or i (cloud ice) and, r_{l0} is a threshold mixing ratio of cloud condensate.

See Khairoutdinov and Randall (2003) for additional details concerning the model's bulk microphysics and SGS turbulence parameterizations.

2.4.2 Experimental setup

The basic state temperature and moisture soundings are taken from the GATE mean sounding described earlier with z_T = 28 km. The simulation is initialized with a relatively

warm and moist "bubble" located near the surface and at the horizontal center of the domain (x_c). The initial temperature anomaly of the bubble is given by

$$T'(x,z) = T_0' \cos\left(\frac{\pi}{2}\sqrt{\left(\frac{x-x_c}{x_b}\right)^2 + \left(\frac{z}{z_b}\right)^2}\right), \tag{2.52}$$

where, T_0' = 0.5 K, and x_b = 8000 m and z_b = 800 m are the maximum half-width and maximum height of the bubble, respectively. The initial relative humidity (*RH*) anomaly is given by a similar expression but with RH_0' = 10 %.

The model domain is 512 km wide and 28 km tall with the vertical grid spacing stretching from 25 m near the surface to 250 m above 6 km. The horizontal grid spacing is 250 m at all points. The use of a stretched vertical coordinate allows for increased resolution in the lower portions of the atmosphere where the cloud first develops. The domain is wide enough so that the majority of horizontally propagating gravity wave energy does not cross the lateral boundaries during the simulation. Rayleigh damping is applied in the uppermost 8 km of the domain to reduce the reflection of vertically propagating gravity waves. The simulation lasts for 2.25 hrs and all fields are saved at 2.25 minute intervals.

2.4.3 Model analysis strategy

The statement expressing conservation of energy of the *n*th vertical normal mode, (2.17), can be written as

$$\frac{\partial}{\partial t}E_n = -\frac{\partial}{\partial x}(\phi_n u_n) + EKE_n + EAPE_n, \tag{2.53}$$

where, EKE_n represents the eddy generation of KE_n and $EAPE_n$ represents the eddy generation of APE_n. The source terms, F and Q, are given by

$$F = F_{sgs} - \left(u\frac{\partial u}{\partial x} + \omega\frac{\partial u}{\partial p} \right) \text{ and} \tag{2.54}$$

$$Q = Q_{mic} + Q_{sgs} - c_p\left(u\frac{\partial}{\partial x}T' + \omega\frac{\partial}{\partial p}T' \right) + \omega\frac{RT'}{p}, \tag{2.55}$$

respectively, where F_{SGS} and Q_{sgs} represent terms involving SGS-transport processes and Q_{mic} is the heating due to microphysical processes. Taking the domain average of (2.55), we arrive at

$$\frac{\partial}{\partial t}[E_n] = [EKE_n] + [EAPE_n]. \tag{2.56}$$

The goal is to determine how well the results of the simulation satisfy (2.55). To achieve this objective, we use the vertical normal mode transform to compute E_n, EKE_n, and $EAPE_n$ at each grid-column in the simulation. The procedure for projecting model output onto the $\Psi_n s$ is briefly discussed below.

The transformed variables, $u_n(x)$ and $\partial\Phi_n^{mic}(x)/\partial t$, are calculated as

$$\frac{\partial}{\partial t}\Phi_n^{mic}(x) = \left\langle \int_p^{p_B} \tilde{Q}_{mic}(x, p) d\ln p, \Psi_n(p) \right\rangle, \tag{2.57}$$

$$\frac{\partial}{\partial t}\Phi_n^{mic}(x) = \left\langle \int_p^{p_B} \tilde{Q}_{mic}(x, p) d\ln p, \Psi_n(p) \right\rangle, \tag{2.58}$$

respectively, where the '~' indicates that the profile of simulated data has been linearly interpolated from the z-level coordinate system of the CRM to the p-level coordinate system of the Ψ_ns. Similar expression are used to obtain the transformed variables, ϕ_n, F_n^{sgs}, and $\partial\Phi_n^{sgs}(x)/\partial t$. Special care must be taken, however, in evaluating the non-linear terms appearing in (2.56) and (2.57), since they are formulated in a p-level coordinate system. Here, these terms are approximated simply as

$$F_{non} \approx -\left(u\frac{\partial u}{\partial x} + w\frac{\partial u}{\partial z}\right) \text{ and} \tag{2.59}$$

$$Q_{non} \approx -c_p\left(u\frac{\partial}{\partial x}T' + w\frac{\partial}{\partial z}T'\right) - wg\frac{T'}{\overline{T}}, \tag{2.60}$$

where terms involving either triple products of primed quantities or $\partial p'/\partial t$ have been neglected.

2.4.4 Results

Fig. 2.10a is a time-height plot of the domain averaged net latent heating rate, $[Q_{mic}]$, during the first 80 mins of the simulation. Areas shaded in blue (yellow) denote regions where the heating (cooling) rate exceeds 2 K day $^{-1}$. The development of the cloud is evident as a vertically coherent "pulse" of heating that rises through most of the depth of the troposphere between 20 and 45 mins; a secondary pulse of weaker amplitude occurs between 40 and 65 minutes. The time-height evolution of $[Q_{non}]$, depicted in Fig. 2.10b, implies relatively strong warming at the top of the cloud and cooling at its base.

The spectral evolution of $[EAPE_n]$, depicted in Fig. 2.10c, shows a "burst" of energy production between 15 and 35 mins. As the cloud-top rises from roughly 1 to 6 km (between 15 and 25 mins), peak values of $[EAPE_n]$ are found to shift "upwards" from 16 to 47 m s^{-1} with additional production occurring across a broad range of higher-order modes at 25 mins. As the cloud-top rises from roughly 6 to 14 km (between 25 and 35 mins), strong secondary and tertiary peaks develop at 20 and 14 m s^{-1}, respectively, in addition to the primary peak at 47 m s^{-1}. Note that an inspection of the evolution of $[EAPE_n^{sgs}]$,

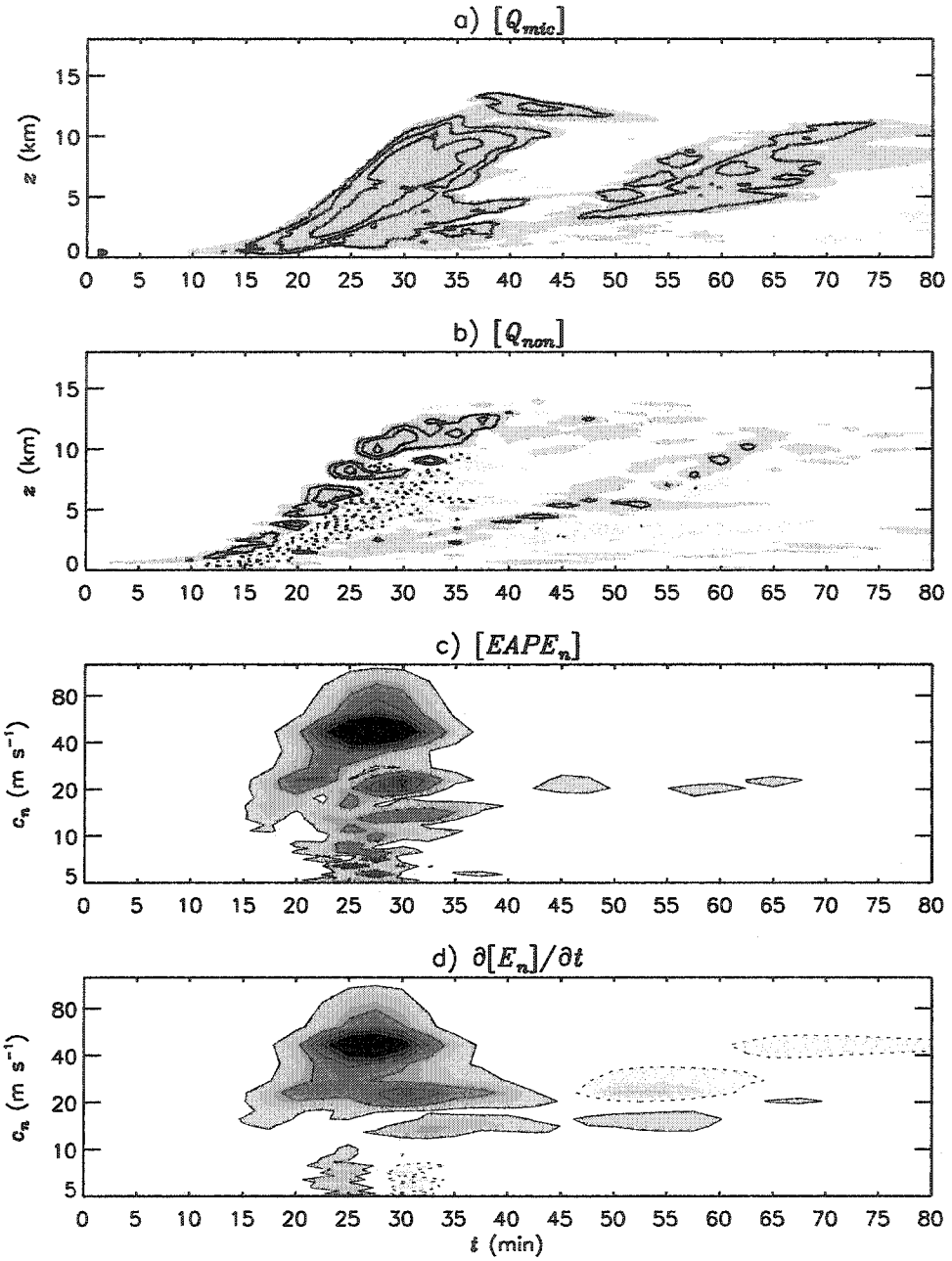

Figure 2.10 Evolution of $[Q_{mic}]$ (a), $[Q_{non}]$ (b), $[EAPE_n]$, and $\partial[E_n]/\partial t$ (d) during the first 80 mins of the 2D CRM simulation of an isolated cloud. In the top two panels, blue (yellow) shading denotes positive values greater (less) than 2 K day^{-1}, while solid (dashed) contours denote heating rates of plus (minus) 4, 8, 16, and 32 K day^{-1}. In d), blue (yellow) filled contour intervals are plus (minus) 1.5 m^2 s^{-3} day^{-1}, starting at this same value. The contour levels in c) are *twice* those in d).

$[EAPE_n^{non}]$, and $[EKE_n]$ (not shown), reveals that the production of $[E_n]$ due to non-linearities and SGS-transport processes is typically an order of magnitude smaller than that due to microphysical processes.

Comparing Figs. 2.10c and d, we that the evolutions of $[EAPE_n]$ and $\partial[E_n]/\partial t$ are in qualitative agreement with one another; Fig. 2.10d illustrates that $[E_n]$ increases at roughly the "correct" times and in roughly the correct spectral locations as predicted by $[EAPE_n]$. Unlike Fig. 2.10c, however, Fig. 2.10d also shows periods when $\partial[E_n]/\partial t$ is negative. The amplitudes of the latter quantity are also much weaker than those of $[EAPE_n]$, especially considering that the shading levels in Fig. 2.10d are a factor of two smaller than those in Fig. 2.10c. This difference implies that the simulated amplitudes of u_n and ϕ_n are roughly 40% smaller than those expected on the basis of linear hydrostatic theory.

Pandya et al. (1993) observe a similar amplitude difference when comparing the linear responses of a stably stratified atmosphere to a convective heat source with and without the hydrostatic approximation. The authors also observe that the non-hydrostatic gravity wave pulses excited by the source: 1) travel slightly slower than their hydrostatic counterparts and 2) are followed by series of trailing pulses that are both weaker in amplitude and narrower in width than their predecessor. The sign of the temperature perturbations etc. associated with each trailing pulses is also reversed from one to the next. Thus, the relatively broad area of deep subsidence associated with the first internal mode's response to the heating is immediately followed by a narrower region of deep ascent.

Figs. 2.11a-c are Hovmoller diagrams depicting the space-time evolution of $\mathrm{Log}_{10}(E_n)$ in the 47, 20, and 14 m s^{-1} modes, respectively. The diagrams are broadly consistent with

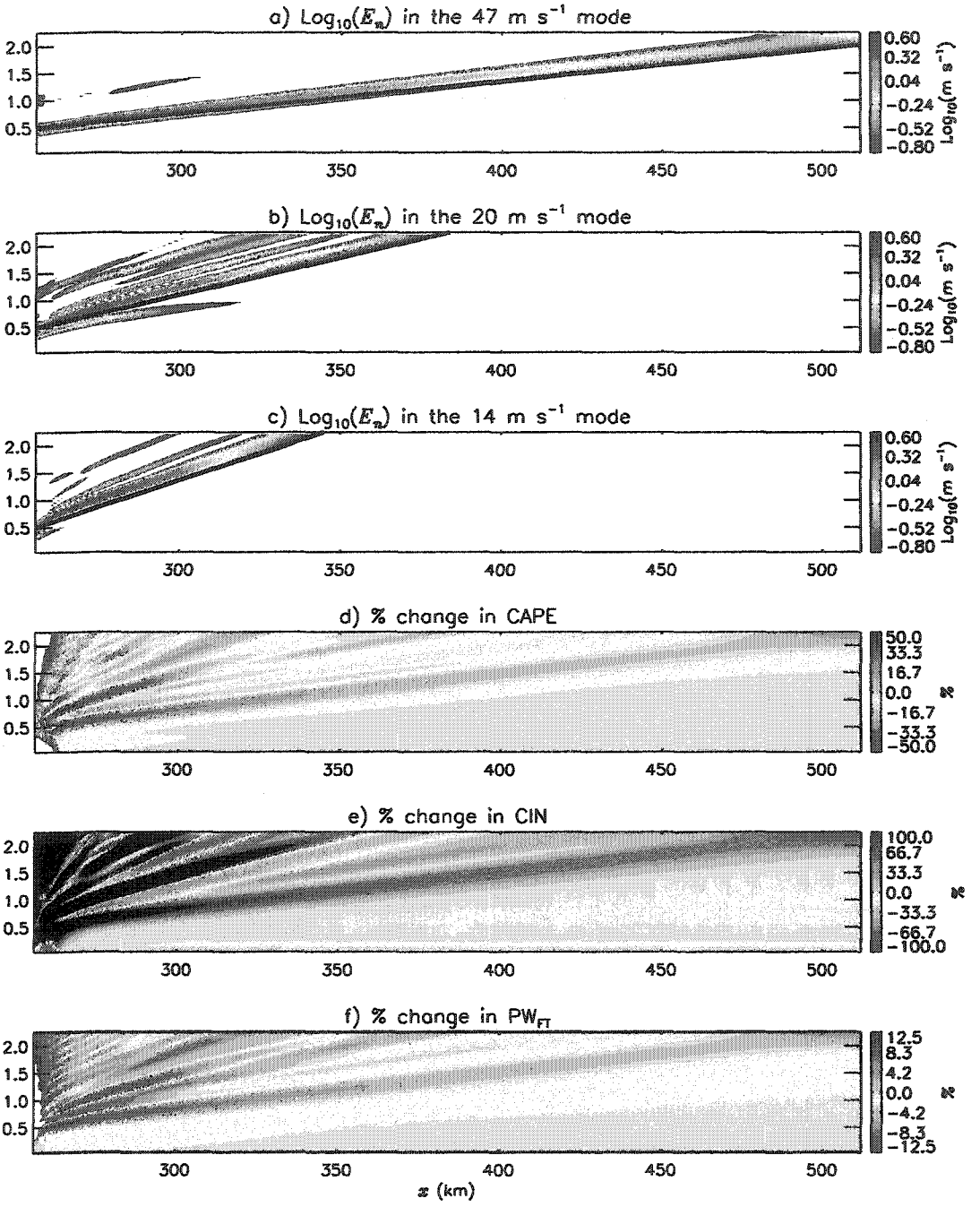

Figure 2.11 Hovmoller diagrams (diagnosed from the 2D CRM simulation) of $Log_{10}(E_n)$ in modes with c_n = 47 (a), 20 (b), and 14 (c) m s^{-1} and of the percentage change in background values of CAPE (d), CIN (d), PW_{FT} (f). The thick solid lines in a)-c) denote the theoretically expected phase speed of the vertical normal mode.

the diagnosed evolution of $[EAPE_n]$ and also with the theory outlined in Section 1.3; they show evidence for the generation and emission of gravity packets between 15 and 65 mins with strongest emission occurring between 25 and 35 mins. In Figs. 2.11b and c, we see that the strongest gravity wave packets are followed by one or more trailing packets. The latter first become apparent some distance away from the cloud and are both weaker in amplitude and more narrow in width than the former. The thick solid lines in each panel, corresponding to the phase speed of the respective vertical normal mode, show that the individual gravity wave packets propagate at speeds slightly slower than that theoretically expected on the basis of hydrostatic theory.

The energy of the packets is seen to decrease with time in Figs. 2.11a-c, consistent with the negative values of $\partial[E_n]/\partial t$ appearing in Fig. 2.10d. Because the magnitudes of the energy dissipation terms, $[EAPE_n^{sgs}]$ and EKE_n^{sgs}, were both found to be negligible, it is speculated here that this damping is due to the effects of implicit numerical diffusion.

The evolution of the CAPE, CIN, and PW_{FT} in the isolated cloud simulation, depicted in the bottom three panels of Fig 2.11, appears qualitatively similar to that theoretically predicted in Section 2.3 (see Fig. 2.6). The 47 m s^{-1} mode, for example, appears as a relatively broad region where values of CAPE and PW_{FT} are both strongly reduced from their background values, while CIN is strongly increased. The 20 m s^{-1} mode, on the other hand, appears as a narrower region where values of CIN and PW_{FT} are both strongly increased, while CAPE is largely unaffected.

There is an important difference between the results of the cloud simulation and those obtained analytically. In the cloud simulation, the impact of the higher-order modes on the

CAPE and PW_{FT} is comparable in magnitude to that of the lower-order modes; the theoretical predictions, on the other hand, show the latter to be much weaker. This is possibly explained by the fact the vertical profile of the latent heating within the simulated cloud is top-heavy during the later stages of its lifetime. As demonstrated in Section 2.3, an elevated (positive-only) convective heat source, with a maximum heating rate in the upper-troposphere, will more efficiently excite higher-order modes than a deep convective source with a maximum heating rate in the middle troposphere (compare Figs. 2.5c and f).

2.5 Summary and discussion

This chapter investigated the gravity wave response of a stably stratified atmosphere to a deep convective heat source of finite duration. In Section 2.3, the problem was studied analytically in the context of linear hydrostatic theory. Results showed that: 1) an isolated deep convective cloud is more efficient (relative to impulsive heating) at generating energy in higher-order vertical normal modes and 2) the passage of these modes is accompanied by low-level cooling and column-integrated moistening. The implications are that a *transient,* deep convective heat source tends to create a region around itself where conditions are favorable for further convective development. If the convection is either especially long-lived or propagates at speeds significantly different than that of the background flow, then this region may be many times larger than the size of the convective heat source. This suggests a possible mechanism for the development of large-scale convectively coupled gravity waves.

Section 2.4 used the vertical normal mode transform algorithm of FS85 to analyze output from a 2D CRM simulation of an isolated cloud. Results showed qualitative agreement

between the theoretical predictions outlined in Section 2.3 and the simulation. Quantitative differences were most likely due to the effects of: 1) non-hydrostatic dynamics and 2) implicit numerical diffusion in the CRM.

The results of this chapter suggest that the stratiform instability models of Mapes (2000) and Majda and Schefter (2001) may be over-simplified. Indeed, they provide evidence that deep convective heating processes, as well as stratiform processes, play a direct role in the development and maintenance of convectively coupled Kelvin (gravity) waves. Further evidence to support this idea is presented in the next chapter which performs a linear stability analysis of an inviscid, 2D tropical wave model.

CHAPTER 3

A SIMPLE MODEL OF CONVECTIVELY COUPLED GRAVITY WAVES

3.1 Introduction

The previous chapter investigated the 2D response of a non-rotating tropical atmosphere to a finite-duration convective heat source. Results showed that an isolated deep convective cloud tends to strongly excite either a second or third internal mode, depending on the depth of the heating, and that the passage of this mode is accompanied by moistening of the free troposphere, a reduction in CIN, and a slight increase in CAPE. This suggests that tropical deep convection may spontaneously become organized through inviscid gravity wave dynamics, even in the absence of stratiform precipitation processes. This could happen via a stratiform instability-type mechanism, in which the higher-order mode promotes enhanced amounts of deep convection owing to a reduction in CIN. Alternatively, the passage of this mode might favor the development of deep convection owing to its positive impact on the moisture content of the free troposphere. The increased moisture would tend to offset the detrimental effects of dry air entrainment, thereby allowing clouds to develop towards higher levels.

As a first step towards testing this idea, Section 3.3 of the present chapter develops an inviscid, 2D tropical wave model in which: 1) deep convective heating anomalies are directly related to column-integrated water vapor anomalies and 2) vertical structure is truncated to include two vertical normal modes: a deep (fast moving) mode and a shallow (slow moving) mode. The model, later referred to as the moisture relaxation model, predicts that convectively coupled gravity waves should tend to spontaneously develop from random initial conditions, even in the absence of a mean flow. The unstable waves, referred to here as moisture instability- or MI-modes, are found to propagate at speeds close to that of the slower moving vertical normal mode and to exhibit a westward tilt with height in the troposphere. Similar to the predictions of classical wave-CISK models, the largest growth rates are found to occur at the smallest scales. The degree of the "ultraviolet catastrophe" is generally not as severe in this case, however, and is shown to be completely eliminated when the effects of a delayed adjustment between stratiform and deep convective heating processes are included.

In order to distinguish the dynamics and energetics of MI-modes from those of "classical" wave-CISK modes, the following section first discusses a simple tropical wave model in which the convective heating is directly related to the column-integrated moisture convergence. As we shall soon see, the predictions of this model, later referred to as the moisture convergence model, are in broad agreement with those previously obtained by Crum and Stevens (1983), who analyze a wave-CISK model with a similar type of convective parameterization but with a higher vertical resolution.

The results obtained herein set the stage for Chapter 4, in which output from direct numerical simulations are used to assess theories of coupled wave instability.

3.2 The Moisture Convergence Model

3.2.1 Model development

The solutions to the meteorological (hydrostatic) primitive equations can be expressed as a superposition of $n = 0...N$ vertical normal modes (Ψ_ns), where the dynamics of each mode is governed by a system of shallow-water equations. In the absence of friction and rotation, and assuming 2D geometry, these equations are given by

$$\frac{\partial u_n}{\partial t} = -\frac{\partial \phi_n}{\partial x} \text{ and} \tag{3.1}$$

$$\frac{\partial \phi_n}{\partial t} + c_n^2 \frac{\partial u_n}{\partial x} = \frac{\partial \Phi_n}{\partial t}, \tag{3.2}$$

where $\partial \Phi_n / \partial t$ is related to the convective heating, Q, by

$$\frac{\partial \Phi_n}{\partial t} = \left\langle \int_{\ln p}^{\ln p_S} \kappa Q(x, p, t) d\ln p, \Psi_n(p) \right\rangle. \tag{3.3}$$

Conservation of energy is given by

$$\frac{\partial}{\partial t}\left(\frac{1}{2}u_n^2 + \frac{1}{2}\frac{\phi_n^2}{c_n^2}\right) = -\frac{\partial}{\partial x}(u_n \phi_n) + \frac{\phi_n}{c_n^2}\frac{\partial \Phi_n}{\partial t}, \tag{3.4}$$

where $\frac{1}{2}u_n^2$ is the kinetic energy, $\frac{1}{2}\frac{\phi_n^2}{c_n^2}$ is the available potential energy, $-\frac{\partial}{\partial x}(u_n \phi_n)$ is an energy flux divergence, and $\frac{\phi_n}{c_n^2}\frac{\partial \Phi_n}{\partial t}$ is the eddy generation of the available potential energy potential energy.

Separation of variables is undertaken by assuming

$$Q = Q_0 f(x, t) \Omega(p) \text{ and} \tag{3.5}$$

$$\omega = f(x,t)\varpi(p), \tag{3.6}$$

where $\Omega(p)$ is a prescribed, non-dimensional heating profile. Substitution of (3.5) into (3.3) yields

$$\frac{\partial \Phi_n}{\partial t} = \kappa Q_0 f(x,t)\Omega_n, \tag{3.7}$$

where

$$\Omega_n = \left\langle \int_{\ln p}^{\ln p_S} \Omega(p) d\ln p, \Psi_n(p) \right\rangle . \tag{3.8}$$

3.2.1.1 Convective parameterization

The linearized statement expressing conservation of the column-integrated water vapor mixing ratio can be expressed as

$$\int_{p_T}^{p_s} L\left[\frac{\partial r}{\partial t} + \omega(x,p,t)\frac{d\bar{r}}{dp}\right]dp = \int_{p_{CT}}^{p_B} Q_0 f(x,t)\Omega(p)dp, \tag{3.9}$$

where L is the latent heat of condensation, p_{CT} and p_B denote the top and bottom of the heating, respectively, and anomalies in the surface evaporation have been neglected. Following Crum and Stevens (1983), we assume that the vertical integral of the convective heating is proportional to the column-integrated convergence moisture convergence, i.e.,

$$\int_{p_{CT}}^{p_B} Q_0 f(x,t)\Omega(p)dp = -\alpha L \int_{p_T}^{p_s} \omega(x,p,t)\frac{d(\bar{r})}{dp}dp, \tag{3.10}$$

where α is a precipitation efficiency factor ranging between 0 and 1.

What is the physical justification for writing down (3.10)? Actually, there is none, since (3.10) does not directly relate the intensity of convection to the buoyancy of air parcels within clouds, i.e., the quantity that directly controls the intensity of cumulus convection. There is, however, some indirect justification, since moistening of the *free*

atmosphere by column-integrated moisture convergence should tend to offset the detrimental effects of dry air entrainment, thereby enhancing the intensity of the convection. In addition, moisture convergence in the boundary layer should provide the convection with a continuous supply of air with high moist static energy and thus, CAPE.

Running a CRM with imposed time-varying large-scale forcing, Xu and Randall (1997) indeed demonstrate that the intensity of simulated cumulus ensembles is strongly modulated by changes in large-scale moisture convergence, as well as by changes in the large-scale thermal destabilization rate. Crum and Stevens (1983) also find that the predictions of their simple tropical wave model with (3.10) used as a convective parameterization are qualitatively similar (at least with regards to the *mechanism* of coupled wave instability) to those of a model in which convection is parameterized following the more physically justifiable (but also much more complicated) approach of Arakawa and Schubert (1974), later referred to as AS74. Stark (1976) obtained similar findings using a different tropical wave model. In light of the results of Crum and Stevens (1983) and Stark (1976) (and also because of its simplicity), (3.10) is adopted here as a convective parameterization over that of AS74.

Substitution of (3.10) into (3.7) gives

$$\frac{\partial \Phi_n}{\partial t} = -\alpha\left(\frac{L\Omega_n}{\eta}\right)\int_{p_T}^{p_s} \omega(x, p, t)\frac{d\bar{r}}{dp}dp, \tag{3.11}$$

where $\eta \equiv \int_{p_{CT}}^{p_B} \Omega(p)dp/\kappa$. Use of the continuity equation, together with the inverse transform, shows that ω can be expressed as

$$\omega(x, p, t) = -\sum_{n=0}^{N} \frac{\partial u_n}{\partial x}\varpi_n(p), \tag{3.12}$$

where $\varpi_n(p) \equiv \int_{p_T}^{p} \Psi_n(p)dp$. Substitution of this expression into (3.11) yields

$$\frac{\partial \Phi_n}{\partial t} = \alpha\Omega_n \sum_{m=0}^{N} R_m^* \frac{\partial u_m}{\partial x} = \alpha \sum_{m=0}^{N} K_{nm} \frac{\partial u_m}{\partial x}, \tag{3.13}$$

where

$$R_m^* = \frac{L}{\eta}\int_{p_T}^{p_s} R_m(p)dp = \frac{L}{\eta}\int_{p_T}^{p_s} \varpi_n(p)\frac{d\bar{r}}{dp}dp. \tag{3.14}$$

Thus, we have parameterized $\partial\Phi_n/\partial t$ in terms of a weighted sum of $\partial u_n/\partial x$. This parameterization leads to a set of N vertical normal modes that are coupled to one another.

Using (3.10), (3.12) and (3.14), we can express (3.9) as

$$\frac{\partial}{\partial t}R^* - \sum_{n=0}^{N} R_n^*(1-\alpha)\frac{\partial u_n}{\partial x} = 0, \tag{3.15}$$

where

$$R^* = \frac{L}{\eta}\int_{p_T}^{p_s} r(p)dp. \tag{3.16}$$

Thus, for each vertical normal mode we can write

$$\frac{\partial r_n}{\partial t} - (1-\alpha)\frac{\partial u_n}{\partial x} = 0, \tag{3.17}$$

where r_n is the amplitude of the moisture perturbations of the nth mode and

$$r(x, p, t) = \sum_{n=0}^{N} r_n(x, t)R_n(p). \tag{3.18}$$

3.2.1.2 Convective heating profile

The convective heating profile is expressed in z-coordinates as

$$\Omega(z) = \Omega_{dc}(z) + s\Omega_s(z), \tag{3.19}$$

where the first and second terms on the RHS represent the deep convective and stratiform components of the heating, respectively, and s is a constant amplitude factor. The two components are idealized as follows

$$\Omega_{DC}(z) = \left(\pi \frac{z - z_B}{z_{CT} - z_B}\right) \text{ and} \tag{3.20}$$

$$s\Omega_S(z) = -s \sin\left(2\pi \frac{z - z_B}{z_{CT} - z_B}\right), \tag{3.21}$$

where $z_B = 1$ km and $z_{CT} = 14$ km. Two different profiles are considered: a deep convective heating profile with $s = 0$ and a MCS-type heating profile with $s = 0.5$ (given by the dotted curve). These profiles are hereafter to as DC1 and MCS2, respectively.

Figs. 3.1b and c depict the vertical normal mode spectra of Ω_{DC} and Ω_S, respectively. The spectra were computed using the GATE sounding described in Chapter 2 with $z_T = 16$ km and $N = 128$. Positive (negative) values imply low-level cooling (warming) induced by the heating. Note: The sign convention leads to u_n having the same sense as the horizontal winds at the surface. The spectrum for the deep convective heating profile shows a peak negative and peak positive projection at 51 and 20 m s^{-1}, respectively, with the amplitude of the former roughly ten times greater than the latter. The stratiform spectrum, on the other hand, shows a strong positive peak at 27 m s^{-1} with a much smaller positive projection on the 50 and 20 m s^{-1} modes. Because the amplitude of the projection at 20 m s^{-1} is only about 50% larger than the peak appearing in the deep convective heating spectra, we can conclude that stratiform *and* deep convective heating processes both tend to strongly

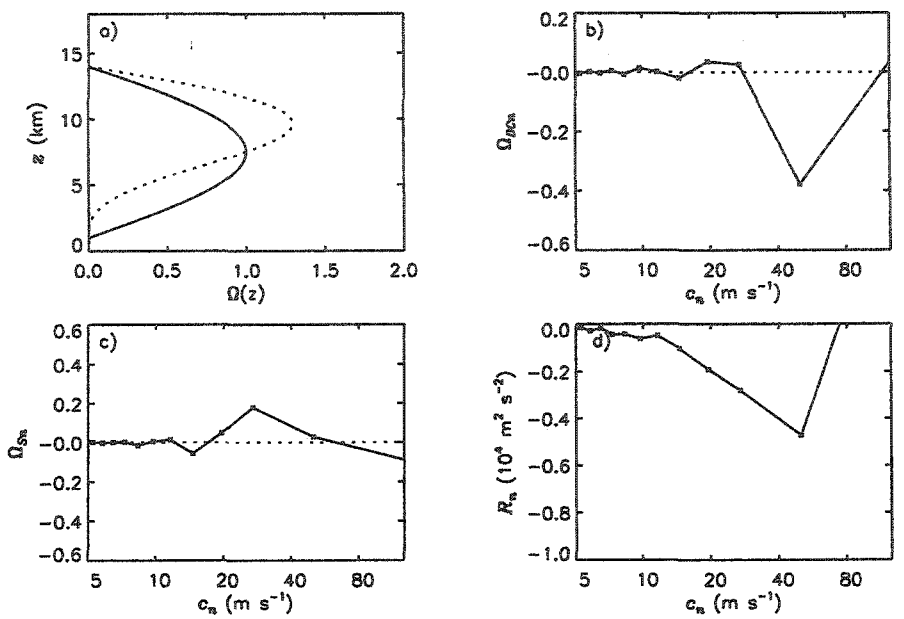

Figure 3.1 Vertical normal mode spectra of deep convective heating profile (b) and stratiform heating profile (c) and vertical normal mode spectra of R_n (d). The plotting symbols denote the actual spectra, while, the curves have been added for viewing purposes. The solid and dotted curves in a) depict the vertical structure of the DC1 and MCS2 heating profiles, respectively.

excite this mode. The 51 m s^{-1} (27 m s^{-1}) mode, on the other hand, is primarily excited by deep convective (stratiform) heating processes.

The spectrum of R_n* for the DC1 heating profile, depicted in Fig. 3.1d, measures the relative change in the column-integrated moisture content caused by $\varpi_n(p)$ (with divergence at the surface). The spectrum shows negative values across all c_ns with a sharp peak at 51 m s^{-1}. The universal drying can explained by the fact that $\bar{r}(p)$ decays rapidly with height, while $\varpi_n(p)$ varies quasi-sinusoidally with height. Thus, the magnitude of column-integrated drying caused by low-level ascent is always greater than the moistening due to upper-level descent.

3.2.1.3 Solution procedure

We seek wave-like solutions of the form, $u_n = \hat{u}_n \exp(i[kx - vt])$ and $\phi_n = \hat{\phi}_n \exp(i[kx - vt])$, where k is real and v has real and imaginary parts, ν_r and ν_i, respectively. The transformed shallow water system can thus be written as

$$c\hat{u}_n = \hat{\phi}_n \text{ and} \tag{3.22}$$

$$-c\hat{\phi}_n + c_n^2 \hat{u}_n = \alpha \sum_{m=0}^{N} K_{nm} \hat{u}_m, \tag{3.23}$$

where $c = \nu/k$ is a complex phase speed. This system can be solved "exactly", with n ranging continuously from 0-N, or approximately, with n ranging over a discrete subset of the continuous spectrum. Here, the latter approach is taken with the subset chosen to consist of two particular modes: a deep mode with $c_n = 51$ m s^{-1} and a shallow mode with $c_n =$ 20 m s^{-1}. These two modes correspond to the most positive and most negative values of Ω_{DCn}, respectively.

With the aforementioned spectral truncation, (3.22) and (3.23) can be expressed as the eigenvalue problem:

$$\begin{bmatrix} -c & 1 & 0 & 0 \\ c_1^2 - \alpha K_{11} & -c & -\alpha K_{12} & 0 \\ 0 & 0 & -c & 1 \\ -\alpha K_{12} & 0 & c_2^2 - \alpha K_{22} & -c \end{bmatrix} \begin{bmatrix} \hat{u}_1 \\ \hat{\phi}_1 \\ \hat{u}_2 \\ \hat{\phi}_2 \end{bmatrix} = 0, \tag{3.24}$$

where the subscripts, 1 and 2, now refer to the deep and shallow modes, respectively, and $c = \nu/k$ is the phase speed of the waves.

Setting the determinant of the matrix in (3.24) equal to zero and requiring $c_r > 0$, yields the eigenvalue pair

$$c_{+/-} = \left(\frac{\tilde{c}_1^2 + \tilde{c}_2^2}{2} \pm \frac{\sqrt{(\tilde{c}_1^2 - \tilde{c}_2^2)^2 - 4\alpha^2 K_{12} K_{21}}}{2} \right)^{1/2} , \tag{3.25}$$

where $\tilde{c}_1^2 \equiv c_1^2 - \alpha K_{11}$, $\tilde{c}_2^2 \equiv c_2^2 - \alpha K_{22}$ and c_+ and c_- refer to the '+' and '-' eigenvalues respectively. The corresponding eigenvectors, later referred to as $\mathbf{U}_+$ and $\mathbf{U}_-$, are each expressed as

$$\begin{bmatrix} u_1 \\ \phi_1 \\ u_2 \\ \phi_2 \end{bmatrix} = \hat{u}_1 \exp(i[kx - vt]) \begin{bmatrix} 1 \\ |c| \exp(i\Theta_\phi) \\ \frac{\hat{u}_2}{\hat{u}_1} \exp(i\Theta) \\ \frac{\hat{u}_2}{\hat{u}_1} |c| \exp(i[\Theta + \Theta_\phi]) \end{bmatrix} , \tag{3.26}$$

where $\hat{u}_1$ and $\hat{u}_2$ are both real. Here, Θ measures the phase shift between the slow and fast modes, while

$$\Theta_\phi = \operatorname{atan}\left(\frac{c_i}{c_r}\right) \tag{3.27}$$

measures the phase shift between ϕ_n and u_n. (3.27) shows that propagating wave-CISK modes are characterized by $0° < \Theta_\phi < 90°$, while stationary wave-CISK modes are characterized by $\Theta_\phi = 90°$.

Using (3.13) and (3.26), the amplitude of the total heating field can be written as

$$\frac{\partial}{\partial t}\hat{\Phi} = \alpha i k \hat{u}_1 K^* \exp[i(\Theta_Q)] , \tag{3.28}$$

where K^* is real (with units of $m^2\ s^{-2}$) and Θ_Q measures the phase shift between $\partial\Phi/\partial t$ and $\partial u_1/\partial x$.

Table 3.1 lists values of K_{11}, K_{12}, K_{21}, and K_{22} for the DC1 and MCS2 heating profiles. In both cases, we see that: 1) $K_{11} > 0$ and $K_{12} > 0$, while, $K_{21} < 0$ and $K_{22} < 0$, and 2) the magnitude of K_{11} is several or more times larger than that of the remaining coefficients.

Table 3.1: Values K_{11}, K_{12}, K_{21}, and K_{22} (where $K_{ij} = \Omega_i R_j$) computed for the DC1 and MCS2 heating profiles. Units are 10^3 m^2 s^{-2}.

Q Profile	K_{11}	K_{12}	K_{21}	K_{22}
DC1	1.79	0.72	-0.17	-0.07
MCS2	2.93	1.16	-0.60	-0.24

3.2.2 Analysis

Before examining the stability of the two-mode system, let's first consider that of a single-mode system with $c_1 = 51$ m s^{-1}. Inspection of (3.25) shows that the phase speed of the waves is given by

$$c = \sqrt{c_1^2 - \alpha K_{11}}. \tag{3.29}$$

When $0 < \alpha < c_1^2/K_{11}$, this expression implies that the waves are neutral and that they propagate more slowly than uncoupled waves. When $\alpha > c_1^2/K_{11}$, on the other hand, it implies that the waves are both unstable and stationary. Apparently, wave-CISK modes cannot propagate in a single-mode system.

CP88 explain this behavior as follows. When $\alpha < c_1^2/K_{11}$, the terms $\partial\Phi_1/\partial t$ and ϕ_1 are 90° out of phase, and thus $\left\{\frac{\phi_1 \partial \Phi_1}{c_1^2 \partial t}\right\} = 0$, where the brackets denote an average over a wavelength. When $\alpha > c_1^2/K_{11}$, on the other hand, the convective heating is strong enough

to overcome the adiabatic cooling due to rising motion, and thus $\left\{\frac{\phi_1 \partial \Phi_1}{c_1^2 \partial t}\right\} > 0$. The unstable waves cannot propagate in this case, however, because the static stability of the fluid has been destroyed by the heating.

The expression for c in a single-mode system with $c_2 = 22$ m s^{-1}, i.e.,

$$c = \sqrt{c_2^2 + \alpha |K_{22}|}, \tag{3.30}$$

shows that the waves are neutral and that their speed *increases* with increasing α. The effect of the heating on c is much weaker in this case, however, since $|K_{22}| \ll K_{11}$.

We now consider the stability of the two-mode system under the DC1 heating profile. The solid and dotted curves in Figs. 3.2a respectively show how the real and imaginary parts of c_+ (thick) and c_- (thin) change as α varies between 0 and 1. As with the models of Crum and Stevens (1983) and Chang and Lim (1988), we see that propagating wave-CISK modes arise through a "coalescence" of the deep and shallow modes. The coalescence occurs here when $\alpha = 0.85$ and $c_{r+} = c_{r-} = 28$ m s^{-1}. As α is increased above this threshold, c_{r+} and c_{r-} both decrease, while values of c_{i+} and c_{i-} diverge from one another, the former (latter) being positive (negative). Thus, $\mathbf{U}_+$ becomes a propagating wave-CISK mode, while $\mathbf{U}_-$ becomes a propagating damped mode.

The curves in Fig. 3.2b illustrate how Θ (solid), Θ_ϕ (dotted), Θ_Q (dashed), and $|\hat{u}_2|/\hat{u}_1$ (dot-dashed) of the propagating wave-CISK mode depend on α. The onset of instability is seen to coincide with the development of a phase shift between the shallow and deep modes, where the sign of the shift implies that the former *leads* the latter. Values

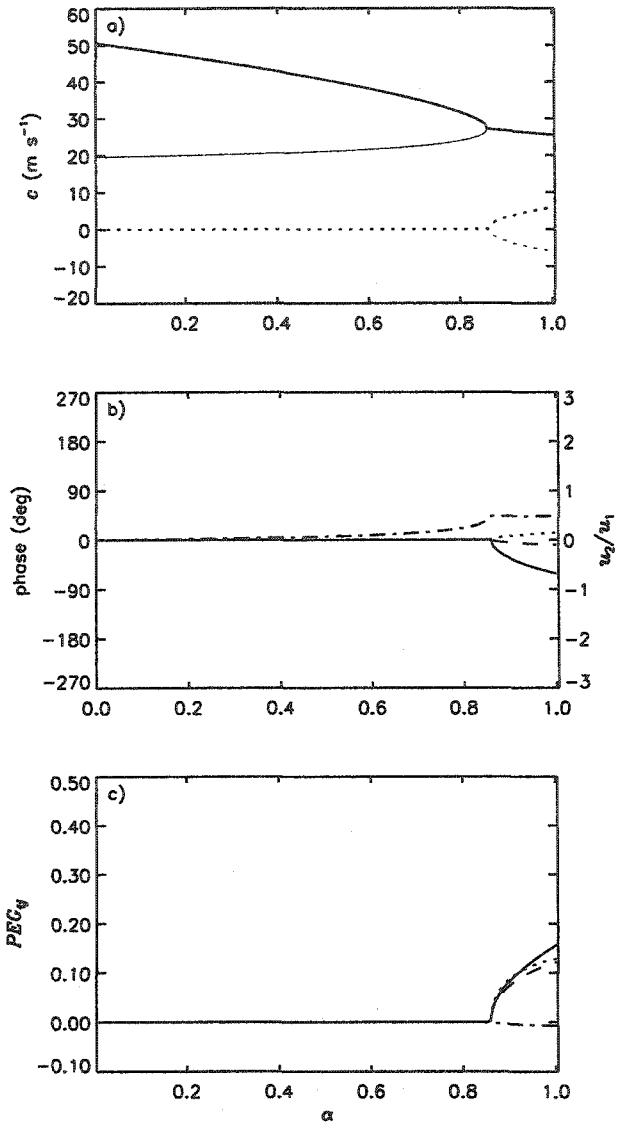

Figure 3.2 a) Real (solid) and imaginary (dotted) parts of c_+ (thick) and c_- (thin) predicted by the moisture convergence model with the DC1 heating profile. b) Normal mode structure of $\mathbf{U}_+$ where the solid, dotted, dashed, and dot-dashed curves denote Θ, Θ_ϕ, Θ_Q, and $\hat{u}_2/\hat{u}_1$, respectively. c) PEG-matrix of $\mathbf{U}_+$ where the solid, dotted, dashed, and dot-dashed curves denote PEG_{11}, PEG_{12}, PEG_{21}, and PEG_{22}, respectively. See text for details

of Θ_ϕ are positive implying that ϕ_n *lags* u_n by less than a quarter wave-cycle. Interestingly, while the magnitudes of Θ and Θ_ϕ both tend to increase with increasing α, values of u_2/u_1 remain constant at about 0.5. Owing to the fact that K_{II} is several times greater

than the remaining K_{ij}s, the convective heating field is largely in phase with, but slightly ahead of, the fast mode's moisture convergence.

3.2.2.1 Energetics

Conservation of energy can be expressed in matrix notation as

$$\begin{bmatrix} \frac{\partial}{\partial t}\{E_1\} \\ \frac{\partial}{\partial t}\{E_2\} \end{bmatrix} = \frac{\alpha k |c| \hat{u}_1^2 \exp(2\nu_i t)}{2} \begin{bmatrix} PEG_{11} & PEG_{12} \\ PEG_{21} & PEG_{22} \end{bmatrix} \begin{bmatrix} 1 \\ 1 \end{bmatrix}, \tag{3.31}$$

where

$$\{E_n\} = \frac{u_n^2}{2}\left(1 + \frac{|c|^2}{c_n^2}\right)\exp(2\nu_i t) \tag{3.32}$$

and

$$\begin{bmatrix} PEG_{11} & PEG_{12} \\ PEG_{21} & PEG_{22} \end{bmatrix} = \begin{bmatrix} \frac{K_{11}}{c_1^2}\sin(\Theta_\phi) & \frac{\hat{u}_2}{\hat{u}_1}\frac{K_{12}}{c_1^2}\sin(\Theta_\phi - \Theta) \\ -\frac{\hat{u}_2}{\hat{u}_1}\frac{|K_{21}|}{c_2^2}\sin(\Theta_\phi + \Theta) & -\left(\frac{\hat{u}_2}{\hat{u}_1}\right)^2\frac{|K_{22}|}{c_2^2}\sin(\Theta_\phi) \end{bmatrix} \tag{3.33}$$

is referred to as the "parameterized energy generation (PEG)-matrix". The diagonal elements of the PEG-matrix, i.e., PEG_{nm} with $n = m$, represent the generation of $\{E_n\}$ caused by moisture convergence of the nth mode being in phase with the thickness field of the nth mode. Since $\Theta_\phi = \text{atan}(c_i/(c_r))$, (3.33) shows that these elements will be non-zero only when c_i is non-zero. The off-diagonal elements, i.e., PEG_{nm} with $n \neq m$, on the other hand, represent the generation of $\{E_n\}$ caused by moisture convergence of the mth mode being in phase with the thickness field of the nth mode. Provided that $-180° < \Theta < 0°$, these elements will generally be positive when $|\Theta_\phi|$ is small.

Fig. 3.2d shows how the energetics of the propagating wave-CISK mode depend on α. Consistent with the above discussion, we see that the terms, PEG_{12} and PEG_{21}, given by the dashed and dotted curves, respectively, each generally serve to maintain the energy of the disturbance. The non-zero lag of ϕ_n with respect to u_n also leads to relatively strong generation of energy in the deep mode by PEG_{11} and weak damping in the shallow mode by PEG_{22}. A surprising result is that the generation of energy in the shallow mode is comparable to that of the deep mode, even though the convective heating couples most strongly with the deep mode.

3.2.2.2 The effects of stratiform heating

Fig 3.3 is identical to Fig 3.2 but for the MCS2 heating profile. In this case, we see that the onset of instability occurs at a significantly lower value of α and that the growth rates are much larger. Owing to the fact that the shallow mode is more efficiently excited by the heating, u_2/u_1 of the unstable mode is roughly twice that found previously and the production of energy is dominated by PEG_{21}, i.e., convergence anomalies of the deep mode being in phase with the thickness field of the shallow mode. The larger values of Θ_ϕ, owing to the larger imaginary phase speeds, leads to a decline of PEG_{12} with increasing α when the latter exceeds a value of roughly 0.55.

The upper two panels of Fig. 3.4 depict the longitude-height structure of the horizontal wind and temperature anomalies associated with the propagating wave-CISK mode for α = 0.65. The phase shift between the fast and slow modes ($\Theta = -85°$) leads to the unstable waves having a boomerang-like structure with the elbow of the boomerang located in the upper troposphere. The amplitude of the convective heating, given by the solid curve in

each panel, is largest when air is anomalously cool in the lower troposphere, anomalously warm in the upper troposphere, and anomalously cool at the level of the tropopause. The maximum in the convective heating leads the divergence at 10 km by roughly 30°, while slightly leading the convergence at low-levels. The water vapor mixing ratio anomalies, depicted in the bottom panel of Fig. 3.4, show a much less dramatic westward tilt with height in the troposphere than either the horizontal wind and temperature anomalies. Owing to the fact that $\hat{u}_2/\hat{u}_1 < 1$, the magnitude of the anomalies are largest at mid-levels.

3.3 The moisture relaxation model

A problem with the moisture convergence model is that it predicts the largest growth rates to occur at the smallest scales and thus, cannot explain the large-scale organization of convection. As discussed in Chapter 1, Davies (1979) suggested that this problem could be avoided by introducing a time lag (τ_a) between the convective heating and the large-scale moisture convergence. Using a linear β-plane model (continuous in the vertical), he demonstrated that Kelvin wave-CISK modes, with synoptic to planetary scale wavelengths and realistic phase speeds, are rendered unstable when τ_a exceeds 6 hrs.

Davies (1979) introduced a time-lag between convection and large-scale forcing by modifying his wave-CISK closure to include a simple time-dependent cloud ensemble model. Taking a somewhat simpler approach, Goswami and Rao (1994) introduced a time-lag by assuming that the strength of the heating is proportional to the column-integrated moisture anomaly; the constant of proportionality is a moisture relaxation time (τ_r). They suggested that a realistic value of τ_r is about 0.5 days. Using a linear β-plane model, with

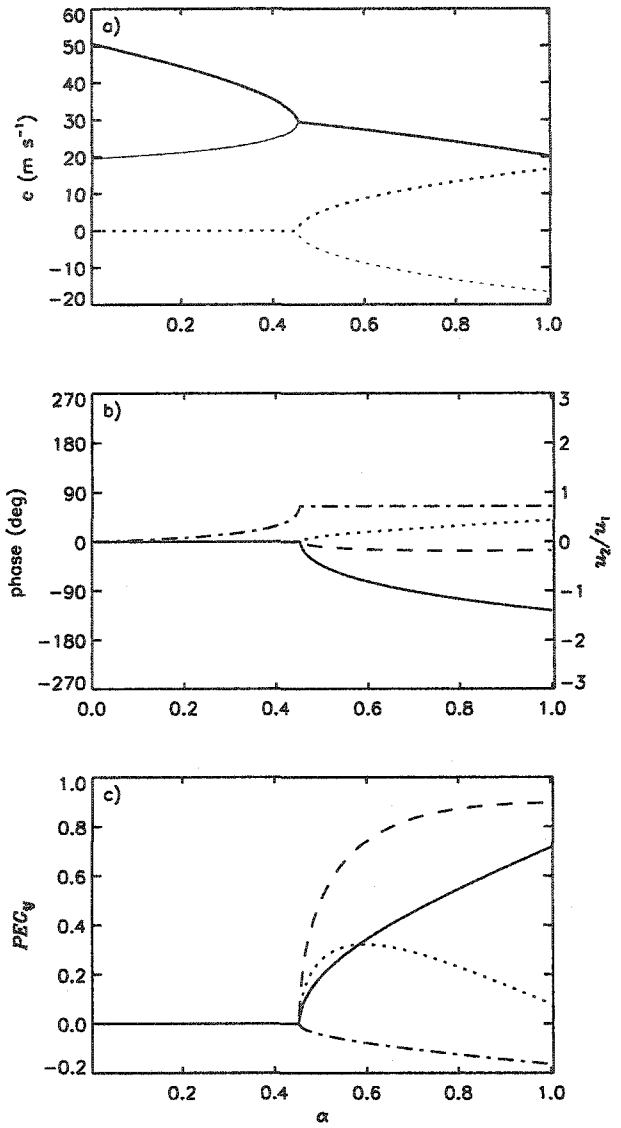

Figure 3.3 Similar to Fig. 3.2 but for the MCS2 heating profile.

vertical structure truncated at the first internal mode, the authors found that planetary-scale Kelvin waves with periods on the order of 30-50 days are rendered unstable in the presence of a mean easterly flow. All waves were found to be damped, on the other hand, in the presence of mean westerlies. Goswami and Rao (1994) did not examine the stability of

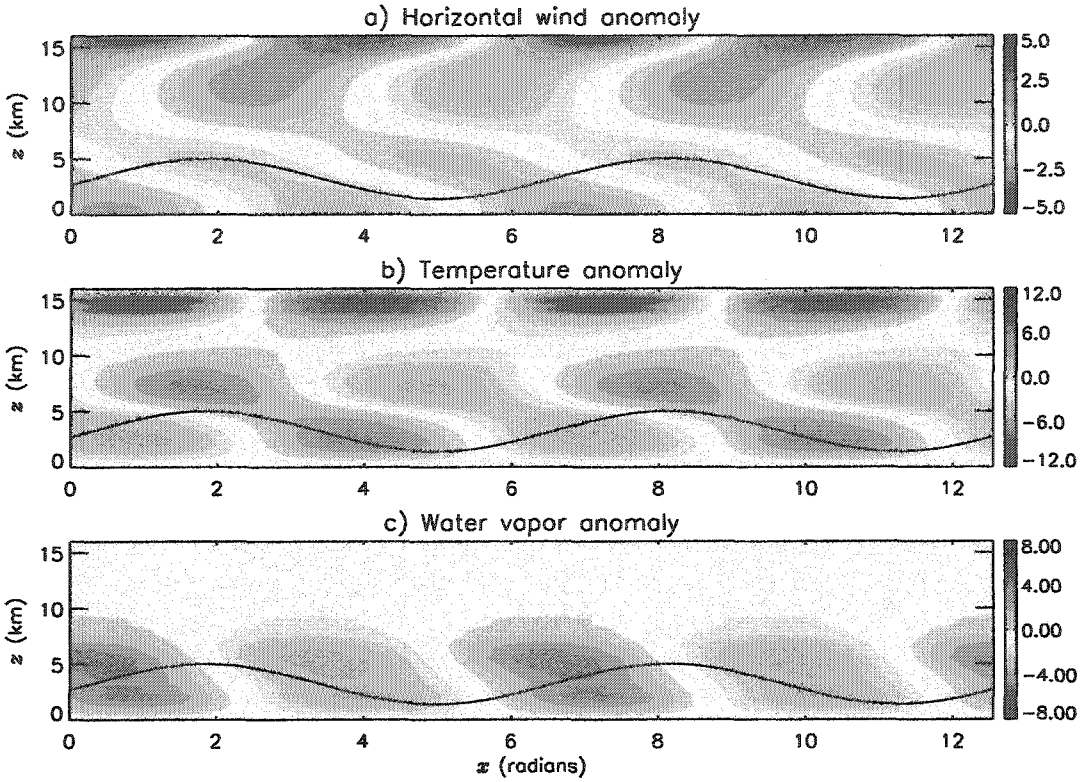

Figure 3.3 Horizontal wind (a), temperature (b), and water vapor mixing ratio anomalies (c) of a propagating wave-CISK mode produced under the MCS2 heating profile with α = 0.65 and $\Theta = -85°$. Horizontal wind anomalies have been non-dimensionalized by $\hat{u}_1$, while temperature anomalies have been non-dimensionalized by $(|c|\hat{u}_1)/R$. Solid curves in each panel denote the amplitude of convective heating anomalies.

their model when vertical resolution is truncated to include two or more vertical normal modes.

3.3.1 Model development

Here, the approach of Goswami and Rao (1994) is adopted by assuming

$$\int_{p_{CT}}^{p_B} Q_0 f(x,t)\Omega(p)dp = \frac{L}{\tau_r}\int_{p_T}^{p_s} r(x,t,p)dp = \frac{\eta}{\tau_r}R(x,t). \qquad (3.34)$$

As with the moisture convergence model developed previously, there is no "rigorous" physical justification for writing down (3.35), since it does not explicitly relate the inten-

sity of the cumulus convection to the in-cloud buoyancy. Once again, however, there is some crude justification, since relatively dry (moist) atmospheres should tend to favor (inhibit) the development of cumulus convection. Furthermore, observations presented in Fuchs and Raymond (2002) demonstrate that there is indeed a strong relationship between monthly averaged values of tropical precipitation and those of precipitable water. As demonstrated in the next chapter, a relationship similar to that observed by Fuchs and Raymond (2002) also holds true on much shorter time scales in explicit numerical simulations of convectively coupled gravity waves.

Following the procedure outlined in Section 3.2.1, we arrive at the following system of ordinary differential equations

$$c\hat{u}_n = \hat{\phi}_n \ , \tag{3.35}$$

$$-c\hat{\phi}_n + c_n^2\hat{u}_n = -ic_\tau \sum_{m=0}^{N} K_{nm}\hat{r}_m \tag{3.36}$$

$$-c\hat{r}_n - \hat{u}_n = ic_\tau\hat{r}_n , \tag{3.37}$$

where the K_{nm}s are identical to those defined previously and $c_\tau \equiv (k\tau_r)^{-1}$. (3.37) shows that, unlike the moisture convergence model, the moisture variable now plays a direct role in the dynamics.

The above system of equations is solved as an eigenvalue problem with the eigenvectors expressed as

$$\begin{bmatrix} u_1 \\ \phi_1 \\ r_1 \\ u_2 \\ \phi_2 \\ r_2 \end{bmatrix} = \hat{u}_1 \exp(i[kx - vt]) \begin{bmatrix} 1 \\ |c| \exp(i\Theta_\phi) \\ \frac{-1}{c_r} \exp(i\Theta_r) \\ \frac{\hat{u}_2}{\hat{u}_1} \exp(i\Theta) \\ |c| \frac{\hat{u}_2}{\hat{u}_1} \exp(i[\Theta + \Theta_\phi]) \\ \frac{-1}{c_r} \frac{\hat{u}_2}{\hat{u}_1} \exp(i[\Theta + \Theta_r]) \end{bmatrix}. \tag{3.38}$$

Here, $c_r = \sqrt{c_r^2 + (c_i + c_\tau)^2}$ is a characteristic phase speed, while

$$\Theta_r = -\text{atan}\left(\frac{c_i + c_\tau}{c_r}\right) \tag{3.39}$$

measures the phase shift between r_n and $-u_n$. The last expression shows that propagating disturbances are characterized by low-level moisture anomalies that *lead* low-level horizontal wind anomalies by less than $90°$, while stationary modes are characterized by moisture anomalies that are either in phase or out of phase with the low-level convergence.

It is convenient to express the solution for r_n in the form

$$r_n = \frac{-\phi_n}{|c| c_r} \exp(i\Theta_{r\phi}) \ , \tag{3.40}$$

where

$$\Theta_{r\phi} = \Theta_r - \Theta_\phi . \tag{3.41}$$

For relatively small values of c_τ, (3.41) shows that propagating neutral modes are characterized by an in-phase relationship between r_n and $-\phi_n$. Unstable waves, on the other hand, are characterized by moisture anomalies leading geopotential anomalies with the magnitude of the phase-shift increasing as c_i and/or c_τ increases.

3.3.1.1 Energetics

Conservation of energy is given by

$$\begin{bmatrix} \frac{\partial}{\partial t}\{E_1\} \\ \frac{\partial}{\partial t}\{E_2\} \end{bmatrix} = \frac{|c|\hat{u}_1^2 \exp(2\nu_i t)}{2\tau_r c_r} \begin{bmatrix} PEG_{11} & PEG_{12} \\ PEG_{21} & PEG_{22} \end{bmatrix} \begin{bmatrix} 1 \\ 1 \end{bmatrix}, \tag{3.42}$$

where the PEG-matrix is now of the form

$$\begin{bmatrix} PEG_{11} & PEG_{12} \\ PEG_{21} & PEG_{22} \end{bmatrix} = \begin{bmatrix} -\frac{K_{11}}{c_1^2}\cos(\Theta_{r\phi}) & -\frac{\hat{u}_2}{\hat{u}_1}\frac{K_{12}}{c_1^2}\cos(\Theta_{r\phi}-\Theta) \\ \frac{\hat{u}_2}{\hat{u}_1}\frac{|K_{21}|}{c_2^2}\cos(\Theta_{r\phi}+\Theta) & \left(\frac{\hat{u}_2}{\hat{u}_1}\right)^2\frac{|K_{22}|}{c_2^2}\cos(\Theta_{r\phi}) \end{bmatrix}. \tag{3.43}$$

Here, the diagonal elements represent the generation of $\{E_n\}$ caused by moisture anomalies of the *n*th mode being in phase with the thickness field of the *n*th mode. When $\Theta_{r\phi}$ is close to zero, we expect amplification (damping) of the shallow (deep) mode. The off-diagonal elements, on the other hand, represent the generation of $\{E_n\}$ caused by moisture anomalies of the *m*th mode being in phase with the thickness field of the *n*th mode. These elements will tend to be small when $\Theta_{r\phi}$ is close to zero and Θ is close to $90°$.

3.3.2 Analysis

We first analyze the stability of the model under the DC1 heating profile with λ = 20,000 km. The curves appearing in Fig. 3.5a illustrate how c_+ (thick) and c_- (thin) change as τ_r varies between 0.5 and 24 hrs. Somewhat different from the moisture convergence model, instability of U_+ (the shallow mode) and damping of U_- (the deep mode) is predicted to occur for *all* choices of τ_r. Owing to the effects of an increased static stability, the

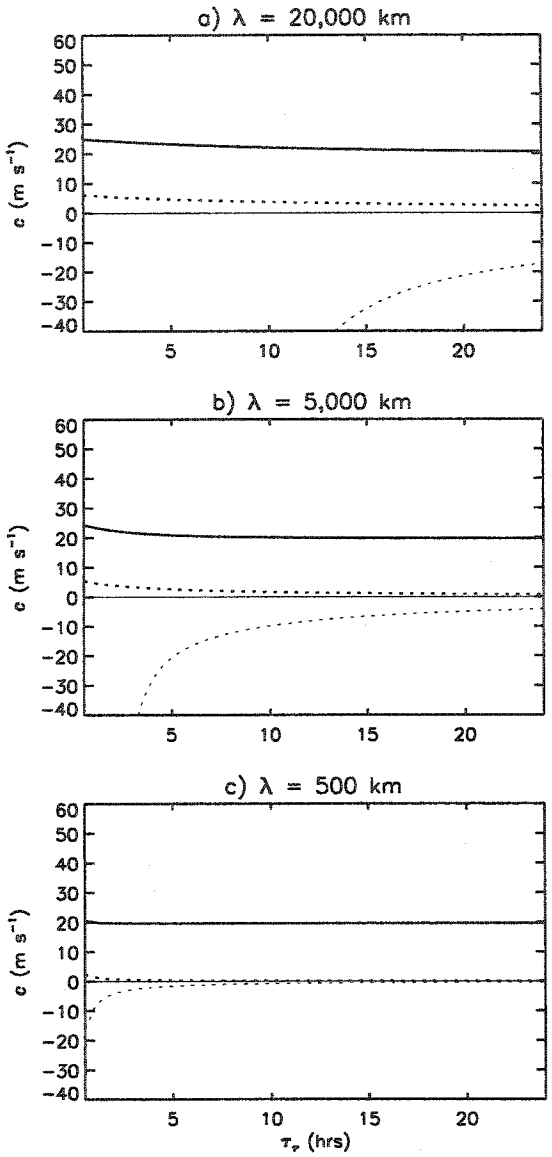

Figure 3.5 Real (solid) and imaginary (dotted) of c_+ (thick) and c_- (thin) predicted by the moisture relaxation model with the DC1 heating profile for three different choices of λ: 20,000 (a), 5,000 (b), and 500 km (c).

propagation speed of the MI-mode increases from 20 to 24 m s^{-1} as τ_r decreases from 24 to 0.5 hrs. The damped mode, on the other hand is stationary. For smaller choices of λ, Fig. 3.5b and c show that the effects of an increased static stability on coupled wave propagation is less dramatic.

The solid, dotted, and dashed curves in Fig. 3.6 illustrate the relationship between λ and the growth rate (μ) of MI-modes for $\tau_r = 0.5$, 8, and 24 hrs, respectively. Similar to the predictions of the moisture convergence model, given by the dot-dashed curve, the largest growth rates occur at the smallest scales. The moisture relaxation model can therefore not explain the preferred horizontal scale of convectively coupled Kelvin waves. For τ_r greater than about 0.5 hrs, however, Fig 3.6 shows that the degree of the ultraviolet catastrophe is not as nearly as severe as that associated with the moisture convergence model.

Fig. 3.7 is similar to Figs. 3.2 and 3.3 but for moisture instability modes with $\lambda = 5{,}000$ km. Much like propagating wave-CISK modes, the MI-modes are characterized by $\Theta < 0°$ and $\Theta_Q \approx 0°$ implying, firstly, that the slow mode leads the fast mode and, secondly, that the convective heating is largely in phase with the convergence field of the fast mode. In this case, however, the magnitude of the phase shift increases asymptotically from 60° towards 84° as τ_r increases from 0.25 to 24 hrs. The relative amplitude of the shallow mode is also generally larger than that predicted by the moisture convergence model, especially for larger values of τ_r.

We can understand this last result by considering the energetics of MI-modes. Fig. 3.7c shows that when τ_r exceeds 12 hrs, energy production in the shallow mode is considerably larger than in the deep mode. This is because PEG_{22} and PEG_{12} are both positive, while PEG_{11} is negative. Consistent with (3.43), the magnitudes of PEG_{11} and PEG_{22} are largest when the magnitude of the phase shift between r_n and $-\phi_n$ is smallest, i.e., at τ_r = 24 hrs.

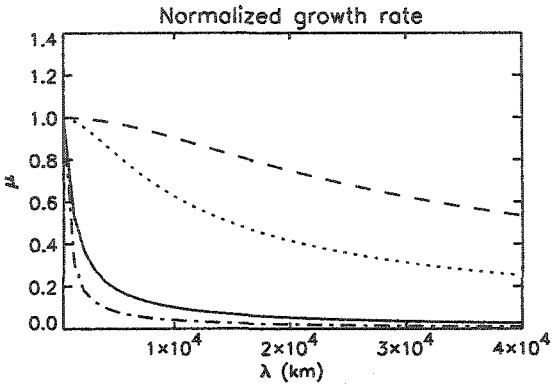

Figure 3.6 Normalized growth rates of MI-modes with τ_r = 0.5 (solid), 8 (dotted), and 2 dashed) hrs and wave-CISK modes (dot-dashed) for λ ranging between 500 and 40,00 km.

Although PEG_{11} acts to remove energy from the deep mode, the slightly stronger source due to PEG_{12} leads to a net production of $\{E_1\}$ (given by the thick solid curve). Moisture anomalies of the shallow mode therefore play a key role in the maintenance of the deep mode. Fig. 3.7b along with (3.43) shows that this mutual interaction occurs partly because $-90° < \Theta < -60°$, implying that the phase shift between the two modes is large enough such that moisture field of the slow mode is partially in phase with thickness field of the fast mode, and partly because $40° < \Theta_{q\phi} < 90°$, implying that moisture anomalies of the slow mode are shifted forward into the thickness field of the fast mode. A similar set of arguments explains the energy source due to PEG_{21}.

3.3.3 The effects of stratiform precipitation processes

The moisture relaxation model suffers from an ultraviolet catastrophe and thus, cannot explain the preferred scale of convectively coupled Kelvin waves. This contrasts with the findings of Davies (1979).

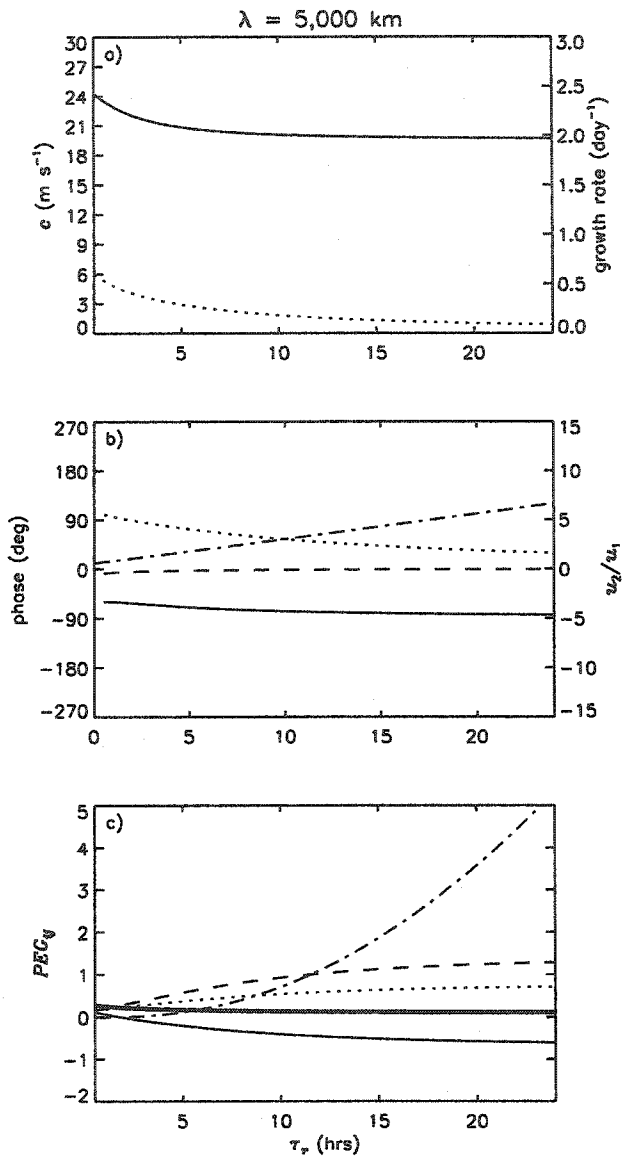

Figure 3.7 a) Propagation speed and growth rate of $\mathbf{U}_+$ predicted by the moisture convergence model under the DC1 heating profile with λ = 5,000 km. b) Normal mode structure of $\mathbf{U}_+$ where the solid, dotted, dashed, and dot-dashed curves denote Θ, $\Theta_{r\phi}$, Θ_Q, and $|\hat{u}_2|/\hat{u}_1$, respectively. c) PEG-matrix of $\mathbf{U}_+$ where the solid, dotted, dashed, and dot-dashed curves denote PEG_{11}, PEG_{12}, PEG_{21}, and PEG_{22}, respectively, and the thick solid line denotes PEG_{11}+PEG_{12}.

As discussed in Chapter 1, Mapes (2000) developed an intermediate tropical wave model in which stratiform precipitation processes are assumed to lag deep convective heating processes and to decay exponentially on a time-scale, τ_S = 3 hrs. When deep con-

vection amount is primarily controlled by the ratio of CIN to subgrid-scale triggering energy, his simulations reveal the spontaneous development of "stratiform instability" waves with phase speeds of about 20 m s^{-1} and zonal wavelengths greater than 1500 km. He suggested that the delayed adjustment of stratiform heating with respect to deep convective is crucial for the development of large-scale waves.

3.3.3.1 Parameterization of stratiform precipitation processes

Following the approach of Mapes (2000), variations in the stratiform heating component are now parameterized as a delayed adjustment process, i.e.,

$$\frac{\partial q_S}{\partial t} = \frac{1}{\tau_S}(s q_{DC} - q_S), \tag{3.44}$$

where $q_{DC}(x,t) = Q_0 f(x,t)$ and $q_S(x,t) = Q_0 g(x,t)$ represent the components of deep convective and stratiform heating, respectively, $s = 0.5$ is the fraction of q_{DC} towards which q_S adjusts, and $\tau_S = 2$ hrs is the time scale of the adjustment process.

Since variations in deep convection are controlled by fluctuations in the column-integrated moisture, i.e.,

$$q_{DC} = \frac{R(x,t)}{\tau_r}, \tag{3.45}$$

conservation of R is now given by

$$\frac{\partial R}{\partial t} - R_1 * \frac{\partial u_1}{\partial x} - R_2 * \frac{\partial u_2}{\partial x} = -\frac{R}{\tau_r} - \eta * q_S \ , \tag{3.46}$$

where

$$\eta^* = \int_{z_B}^{z_{CT}} \frac{\Omega_S}{\Omega_{DC}} dz = -0.35 \ . \tag{3.47}$$

(3.47) together with (3.48) shows that stratiform precipitation processes act to offset the drying effect of deep convection.

3.3.3.2 Model equations

Assuming wave-like solutions, the moisture relaxation model can be written as

$$c\hat{u}_n = \hat{\phi}_n, \tag{3.48}$$

$$-ic\hat{\phi}_n + c_n^2 i\hat{u}_n = c_\tau R\Omega_{nd} + \frac{q_S}{k}\Omega_{ns}, \tag{3.49}$$

$$\left(-ic + \frac{1}{c_S}\right)q_S = \frac{sc_\tau Rk}{c_S}, \text{ and} \tag{3.50}$$

$$\left(-ic + \frac{1}{c_\tau}\right)R = R_n^*\hat{u}_n - \eta^*\frac{q_S}{k}, \tag{3.51}$$

where $c_S \equiv (k\tau_S)^{-1}$. This system of equations differs from that of Mapes (2000), as well as that of Majda and Schefter (2001), in two important respects. First, here, variations in deep convective heating are controlled by column-integrated moisture anomalies, rather than CIN or shallow-CAPE. Second, the current model allows deep convective heating to excite energy in the shallow mode and stratiform heating to excite energy in the fast mode, i.e., Ω_{2d} and Ω_{1s} are both non-zero.

(3.49)-(3.52) are solved as an eigenvalue problem with the solutions for r_1 and r_2 diagnosed from (3.49) together with (3.18). These solutions are written in a form similar to those appearing in (3.35) but with the expressions for c_r and Θ_r now given by

$$c_r = \sqrt{[c_r(1 + c_\tau/c_S^*)]^2 + [c_i(1 - c_\tau/c_S^*) + c_\tau(1 - c_s/c_S^*)]^2} \tag{3.52}$$

and

$$\Theta_r = -\text{atan}\left[\frac{c_i(1-c_\tau/c_S^*)+c_\tau(1-c_s/c_S^*)}{c_r(1+c_\tau/c_S^*)}\right], \tag{3.53}$$

respectively, where

$$c_S^* \equiv |\eta^*|\frac{[c_r^2+(c_i+c_S)^2]}{sc_S}. \tag{3.54}$$

Assuming $c_r > 0$, (3.53) shows that stratiform precipitation processes act to reduce the magnitude of Θ_r with the strongest reduction occurring when c_S^* is smallest, i.e when $c_S = \sqrt{c_r^2 - c_i^2}$.

The solution for the stratiform heating component is written as

$$q_S = \frac{-u_n c_S \exp(i\Theta_{rS})}{c_r\sqrt{c_r^2+(c_i+c_S)^2}}, \tag{3.55}$$

where $\Theta_{rS} \equiv \Theta_r + \Theta_S$ and

$$\Theta_S = \text{atan}\left(\frac{c_i+c_S}{c_r}\right) \tag{3.56}$$

measures the phase shift between the deep convective and stratiform heating components.

3.3.3.3 Analysis

Fig. 3.8 is similar to Fig. 3.6 but for the moisture relaxation model under stratiform adjustment. When $\tau_r = 0.5$ hrs, the behavior is similar to that obtained previously with the largest growth rates occurring at the smallest scales. For larger values of τ_r, on the other hand, the maximum growth rates are seen to occur at intermediate wavelengths in the range 2000-4000 km.

To understand the mechanisms responsible for this scale selection, we first write conservation of energy in the form

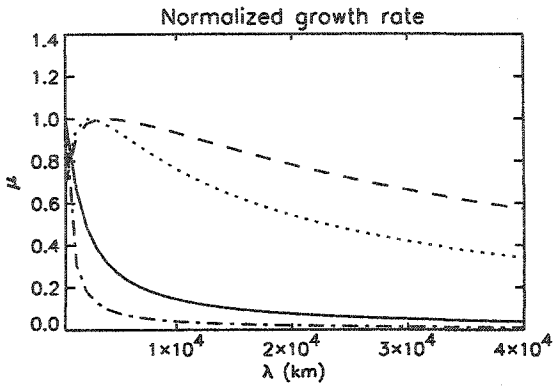

Figure 3.8 Identical to Fig. 3.6 but for the moisture relaxation model under stratiform adjustment.

$$\left(\frac{1}{\{E_1\}+\{E_2\}}\right)\frac{\partial}{\partial t}\{\mathbf{E}\} = \frac{2|c|}{\tau_r c_r e_{tot}}[\mathbf{PEG_{DC}} + \mathbf{PEG_S}]\mathbf{I}\,, \tag{3.57}$$

where

$$e_{tot} = \left(1+\frac{|c|^2}{c_1^2}\right)+\frac{\hat{u}_2^2}{\hat{u}_1^2}\left(1+\frac{|c|^2}{c_2^2}\right). \tag{3.58}$$

Here, $\mathbf{PEG_{DC}}$ is identical to the PEG-matrix appearing in (3.40) and represents the source of energy due to parameterized deep convection; $\mathbf{PEG_S}$, on the other hand, represents the source due to parameterized stratiform heating and is given by

$$\begin{bmatrix} PEG_{S11} & PEG_{S12} \\ PEG_{S21} & PEG_{S22} \end{bmatrix} = \begin{bmatrix} \dfrac{|K_{S11}|}{c_1^2}\cos(\Theta_{rS\phi}) & \dfrac{\hat{u}_2}{\hat{u}_1}\dfrac{|K_{S12}|}{c_1^2}\cos(\Theta_{rS\phi}-\Theta) \\ \dfrac{\hat{u}_2}{\hat{u}_1}\dfrac{|K_{S21}|}{c_2^2}\cos(\Theta_{rS\phi}+\Theta) & \left(\dfrac{\hat{u}_2}{\hat{u}_1}\right)^2\dfrac{|K_{S22}|}{c_2^2}\cos(\Theta_{rS\phi}) \end{bmatrix}. \tag{3.59}$$

Here, $\Theta_{rS\phi} \equiv \Theta_{rS} - \Theta_{\phi}$ measures the phase shift between q_s and ϕ_n, and

$$K_{Snm} = \left(\frac{sc_S}{\sqrt{c_r^2+(c_i+c_S)^2}}\right)\Omega_{Sn}R_m^*. \tag{3.60}$$

The fractional rate of change of the total disturbance energy is given by

$$\frac{1}{\{E_1\}+\{E_2\}}\frac{\partial}{\partial t}[\{E_1\}+\{E_2\}] = 2\nu_i. \tag{3.61}$$

Thus, we can regard the two matrices appearing in (3.57):

$$\mathbf{PGR_{DC}} \equiv \frac{|c|}{\tau_r c_r e_{tot}}\mathbf{PEG_d} \text{ and } \mathbf{PGR_S} \equiv \frac{|c|}{\tau_r c_r e_{tot}}\mathbf{PEG_S}, \tag{3.62}$$

as measuring the relative contributions of parameterized deep convective and stratiform heating processes to the growth of the disturbance.

The heavy solid and dotted curves in Fig 3.9b illustrate how the sums of the elements of $\mathbf{PGR_S}$ and $\mathbf{PGR_{DC}}$, respectively, depend on λ with τ_r held fixed at 11 hrs. The contribution to disturbance growth by parameterized deep convective heating processes increases monotonically with decreasing λ. The contribution by stratiform heating processes, on the other hand, displays a peak at λ_{max} = 3,000 km with values decreasing rapidly to the left of λ_{max} and more slowly to the right.

The dot-dashed curve appearing in the same panel shows that this peak is mainly due to PGR_{S22}, i.e., stratiform heating processes of the shallow mode being in phase with thickness anomalies of the shallow mode. Referring back to (3.38), we see that PGR_{S22} should be large when $\Theta_{rS\phi} = 0°$, an expectation that is confirmed by the thin dotted curve in Fig. 3.9c. Because $\Theta_{r\phi}$, given by the thick dotted curve, is equal to ~ 30° when $\Theta_{rS\phi} = 0°$, we conclude that the existence of a phase shift between r_n and $-\phi_n$, with the former leading the latter, is crucial for the existence of the peak in PGR_{S22} at λ_{ma}. This phase shift leads to a situation in which stratiform heating anomalies parameterized by r_2 fall perfectly in

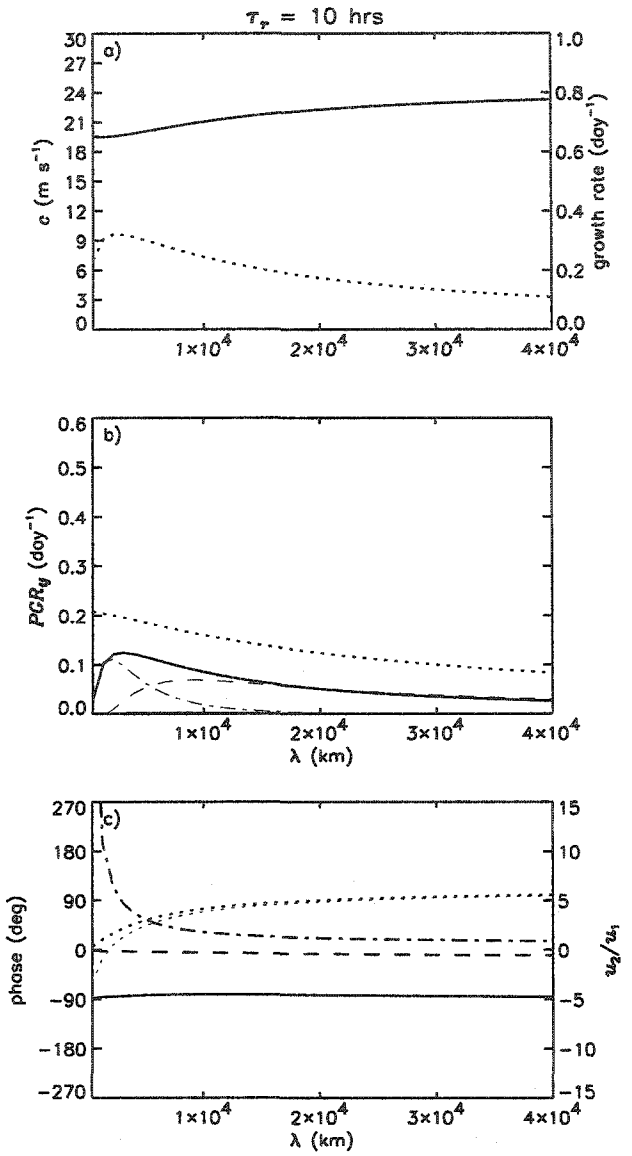

Figure 3.9 a) Phase speed (solid) and growth rate (dotted) of MI-modes under stratiform adjustment with τ_r held fixed at 8 hrs and λ ranging between 500 and 40,000 km. b) Sum of elements of $\mathbf{PGR_{DC}}$ (dotted) and $\mathbf{PGR_S}$ (solid) along with PGR_{S21} (thin dashed) and PGR_{S22} (thin dot-dashed). c) Normal mode structure of MI-modes where the solid, dotted, thick dotted, dashed, and dot-dashed curves denote Θ, $\Theta_{r\phi}$, $\Theta_{rS\phi}$, Θ_Q, and $\hat{u}_2/\hat{u}_1$, respectively

phase with $-\phi_2$. When τ_r is increased to 24 hrs, the wavelength at which q_S and $-\phi_2$ fall perfectly in phase with one another increases to roughly 4000 km (not shown).

Choosing λ = 5,000 km and τ_r = 10 hrs, Figs. 3.10a-c respectively depict the longitude-height structure of the horizontal wind, temperature, and water vapor mixing ratio anomalies associated with the MI-modes under stratiform adjustment. As before, the phase shift between the fast and slow modes leads to the waves having a boomerang-like structure with the elbow the boomerang located in the upper troposphere. In this case, however, the angles of the tilts are slightly larger, especially for the water vapor perturbations. Given that the phase shift between the fast and slow modes is comparable to that of the wave-CISK mode appearing Fig. 3.3, the aforementioned difference can primarily be attributed to the larger amplitude ratio of the slow mode to the fast mode. We also see that, in this case, the phase-lag (-lead) of the heating with respect to the low-level convergence (upper-level divergence) is considerably larger and that the heating is more in phase with the temperature anomalies.

3.4 Summary and conclusions

This chapter discussed the stability and energetics of a linear, inviscid, 2D tropical wave model under two fundamentally different types of convective parameterizations: one in which the convective heating was assumed to be proportional to the column-integrated moisture convergence and one in which the convective heating was assumed to be proportional to the column-integrated moisture anomaly. Following the approach of Mapes (2000) and Majda and Schefter (2001), vertical structure was truncated to include just two vertical normal modes: a deep (first internal) and a shallow (second internal mode). The vertical profile of the heating was assumed rather than being explicitly calculated.

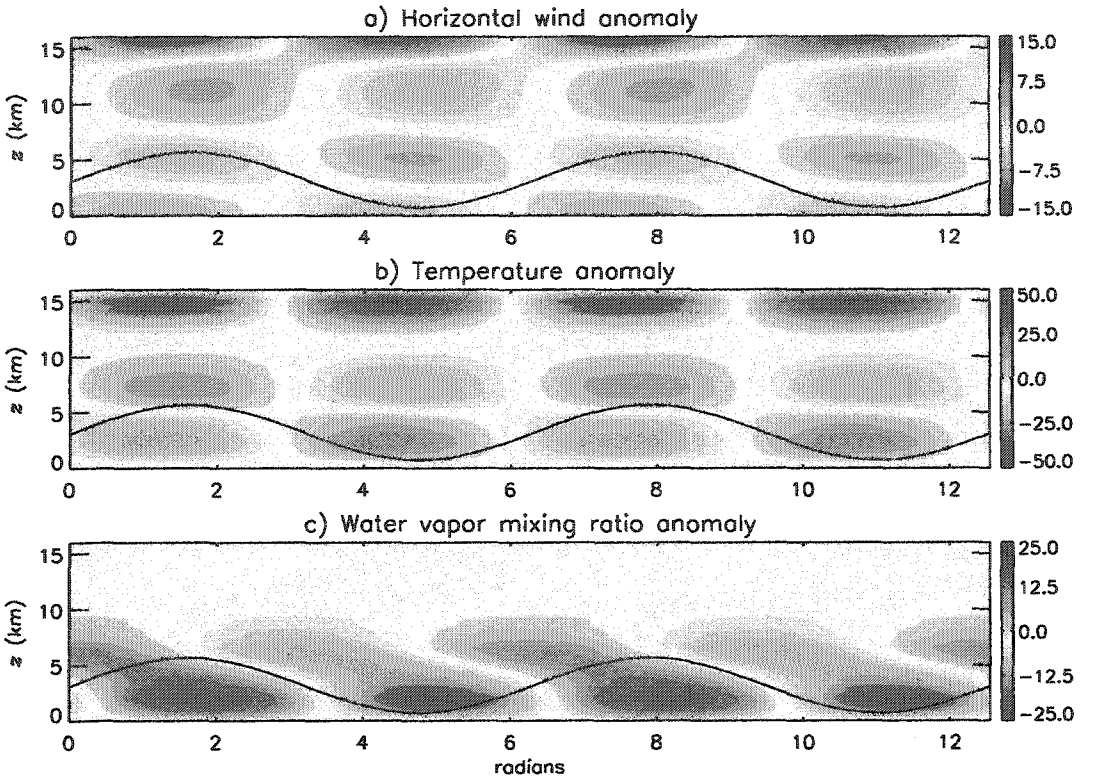

Figure 3.8 Similar to Fig. 3.3 but for the moisture relaxation model under stratiform adjustment with $\lambda = 5{,}000$ km, $\tau_r = 10$ hrs, and $\Theta = -84°$.

Both models predict that convectively coupled gravity waves should spontaneously amplify from random initial conditions, even in the absence of a mean flow or stratiform precipitation processes. The unstable waves predicted by the moisture convergence model were found to resemble the wave-CISK modes previously studied by Francis and Crum (1983) and Chang and Lim (1988). The unstable waves predicted by the moisture relaxation model were referred to as here MI-modes and have not been previously studied. The similarities and differences between the wave-CISK modes and MI-modes are discussed below.

In both types of disturbances, there exists a phase lag between the slow and fast modes with the former leading the latter. As a result, the temperature and horizontal wind

anomalies exhibit a boomerang-like structure with the elbow of the boomerang located in the upper troposphere. The deep convection associated with the waves is strongest when air is anomalously cool in the lower troposphere, anomalously warm in the upper troposphere, and cool at the level of the tropopause. Upper-level divergence (low-level convergence) lags (leads) the region of strongest heating.

The wave-CISK modes arise as a coalescence of the deep and shallow modes. The coalescence is made by possible the relatively strong reduction in the phase speed of the deep mode; the reduction eventually allows an in-phase relationship between the thickness field of the shallow (deep) mode and the convergence field of the deep (shallow) mode, i.e., $PEG_{21} > 0$ and $PEG_{12} > 0$. Both the propagation speed of the unstable waves and the phase shift between the slow and fast modes is highly sensitive to changes in the strength of the heating. This sensitivity is due to the waves feeling the effects of a reduced static stability.

The MI-modes, on the other hand, arise through a strong coupling with the shallow mode and may occur even in the absence of the deep mode (results not shown). The dominant energy production term is generally PEG_{22}, representing moisture anomalies of the shallow mode promoting a convective heating field that is in phase with thickness anomalies of the shallow mode. The propagation speed of the waves and the phase shift between the slow and fast modes are both relatively insensitive to changes in the strength of the heating. Owing to a strong destruction of energy by PEG_{11}, the amplitude ratio of the slow mode to the fast mode is several times larger than that predicted by the moisture convergence model.

In the absence of a delay in stratiform heating, the moisture relaxation model suffers from an "ultraviolet catastrophe" whereby the largest growth rates occur at the smallest scales. The degree of the catastrophe, however, is not as severe as that suffered by the moisture convergence model. When the effects of a delay in stratiform heating are included, the largest growth rates of MI-modes occur at wavelengths in the range 2000-4000 km, depending on the moisture relaxation time.

The results of this chapter provide a set of theoretical predictions for the structure, energetics, and phase speed of convectively coupled gravity waves. A primary goal of the next chapter is to assess these predictions using output from direct numerical simulations.

CHAPTER 4

CONVECTIVELY COUPLED GRAVITY WAVES IN A TWO-DIMENSIONAL CLOUD RESOLVING MODEL

4.1 Introduction

This chapter presents an in-depth analysis of convectively coupled gravity waves simulated using a 2D CRM. The structure and energetics of the waves are analyzed both in physical space and in spectral space (i.e., from a perspective of vertical normal modes). The relative roles of various types of cloud processes, i.e., deep convection, stratiform precipitation, and mid-level convection, in the maintenance of the simulated waves are assessed. This chapter's primary goal is to determine the extent to which the theoretical concepts outlined in Chapters 2 and 3, along with those embodied in the stratiform instability models of Mapes (2000) and Majda and Schefter (2001), are consistent with the results of the simulation. This will lay the groundwork for future studies aimed at improving the representation of convectively coupled equatorial waves in general circulation models.

Before offering a general overview of the simulation (Section 4.5), the following three sections briefly describe the experimental setup, the methodology for classifying different types of convection in the model output, and the methodology for implementing the verti-

cal normal mode transform algorithm. Section 4.6 then discusses the time-mean structure and energetics of the convectively coupled gravity waves in physical space; a parallel discussion in spectral space is given thereafter in Section 4.7. The transient structure of the waves is discussed in Section 4.8. The main findings of the chapter are summarized in Section 4.9.

4.2 Experimental setup

The computational domain is 8192 km wide and 27 km deep with periodic lateral boundary conditions. The horizontal grid spacing is a uniform 2 km, while the vertical grid spacing stretches from 50 m near the surface to 500 m at and above 5 km. The radiative cooling profile is constant at 1.5 K day^{-1} between the surface and 250 mb, decaying linearly to zero at 200 mb. The SST is spatially uniform and held fixed at 300 K. To eliminate possible interactions between convection and a mean flow, the horizontal winds are uniformly relaxed to zero on a 4 hr time scale. Rayleigh damping is applied in the uppermost 8 km to remove energy from gravity waves reflected off of the rigid upper lid. Rotational effects are not considered.

The simulation begins with random small-scale temperature and moisture perturbations added to an otherwise resting and stably stratified atmosphere. The initial temperature and moisture profiles are representative of the equilibrium conditions simulated during a previous 45-day run identical to the one described above but with a smaller 1024 km computational domain. The simulation lasts for 15 days and all fields are saved at 30 min intervals.

4.3 A convection classification scheme

This section describes a scheme for objectively classifying four different types of convection in the simulation: 1) deep, 2) stratiform, 3) mid-level, and 4) non-precipitating shallow convection. The scheme is made up of a series of three steps. The first step consists of masking all deep convective and all mid-level convective regions in the simulation. Inspired by the approach of Tao and Simpson (1989), a deep convective region consists of a "core" grid-point and four neighboring grid-points. Deep convective core grid-points must satisfy one of two criteria: 1) their surface precipitation rate (P) exceeds 5 mm hr^{-1} *and* is more than twice the average value over their four nearest neighbors or, 2) their P exceeds 20 mm hr^{-1}. Mid-level convective regions include a core grid point and two neighboring points, where core grid points satisfy the first of the above criteria but with $P < 5$ mm hr^{-1}.

The second step involves masking all stratiform regions in the simulation. Here, stratiform regions are defined as those grid-points where the latent heating rate (Q_{mic}), integrated from the surface to the melting level (~ 4 km), is less than zero. This definition is based on the notion that deep layers of evaporative cooling in the lower-troposphere, along with relatively low and spatially uniform Ps, are what distinguish stratiform regions of precipitation from convective regions.

In the third step, all remaining grid points with $P > 0$ are masked as additional mid-level convective regions, while non-precipitating grid points with a vertically integrated cloud liquid water content exceeding 1 g m^{-2} are masked as non-precipitating shallow convective regions.

4.4 The vertical normal mode transform: implementation

In the previous chapter, the FS85 vertical normal mode transform algorithm was used to study the interaction between tropical convection and gravity waves in a simplified (i.e., linear and hydrostatic) model framework. Here, the algorithm is employed as a tool for analyzing the structure and energetics of convectively coupled waves produced in a non-linear and non-hydrostatic CRM. The analysis methodology consists of projecting profiles of simulated data onto the vertical normal modes (Ψ_ns) of the model's base-state atmosphere. Considering specific examples, the spectral coefficients, $u_n(x)$ and $\partial\Phi_n^{mic}(x)/\partial t$, are calculated as

$$u_n(x) = \langle \tilde{u}(x, p), \Psi_n(p) \rangle \quad \text{and} \tag{4.1}$$

$$\frac{\partial}{\partial t}\Phi_n^{mic}(x) = \left\langle \int_p^{p_B} \tilde{Q}_{mic}(x, p) d\ln p, \Psi_n(p) \right\rangle , \tag{4.2}$$

respectively, where the '~' indicates interpolation from the z-level coordinate system of the CRM to the p-level coordinate system of the Ψ_ns (equally spaced in log-p to help prevent spectral aliasing).

As discussed in Chapter 2, the Ψ_ns and c_ns represent the eigen-solutions (eigenfunctions and eigenvalues, respectively) of the vertical structure problem, given by

$$\begin{aligned} -\frac{d}{dp}\left(\frac{1}{\bar{\sigma}}\frac{d\Psi_n}{dp}\right) &= \frac{1}{c_n^2}\Psi_n \\ p\frac{d\Psi_n}{dp}\bigg|_{p_T} &= \left[p\frac{d\Psi_n}{dp} + \frac{p^2\bar{\sigma}}{R\bar{T}}\frac{d\Psi_n}{dp}\right]\bigg|_{p_B} = 0 \end{aligned} \tag{4.3}$$

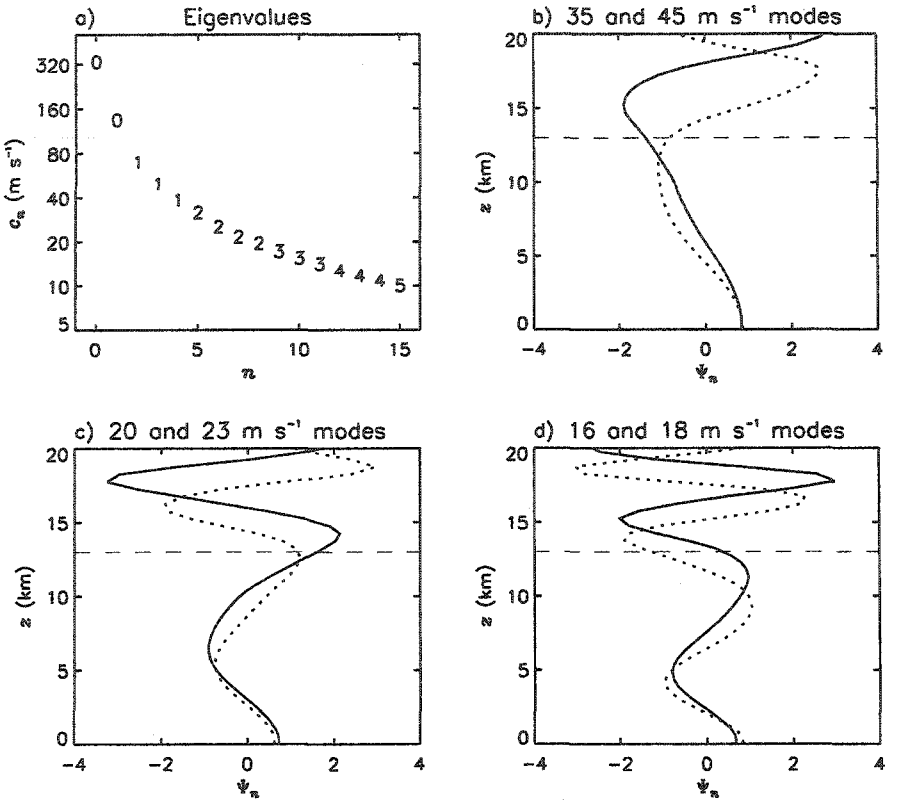

Figure 4.1 Distribution of c_ns for n = 0-15 (a) and selected vertical normal modes (b-d) of the model's base-state atmosphere. Plotting symbols in a) denote the number of times the corresponding vertical normal mode crosses the zero axis between the surface and the tropopause (~13 km). In b)-d), solid (dotted) curve denotes the faster (slower) moving mode, while the dashed line denotes the level of the tropopause.

where $\bar{\sigma}$ is a measure of the base-state static stability. (4.3) was solved using the vertical normal mode transform algorithm with $\bar{T}$ and $\bar{\sigma}$ given by the domain- and time-averaged profiles in the simulation.

Fig. 4.1a shows the calculated distribution of c_ns for n in the range 0-15. Here, as in Fig. 2.1a, the plotting symbols indicate the number of times the corresponding Ψ_n crosses the zero axis between the surface and the tropopause (~ 13 km). A comparison of Figs. 4.1a and 2.1a shows that the distribution of c_ns is quite similar to that obtained for the

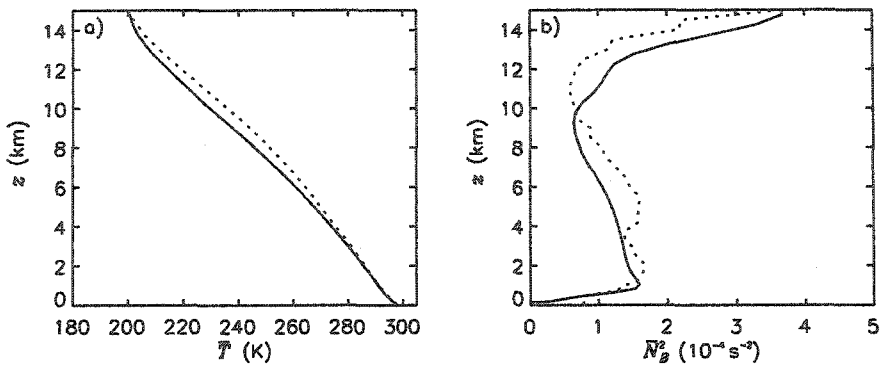

Fig. 4.2 Comparison of the domain- and time-averaged temperature (a) and static stability (b) profiles in the simulation (solid) with the time-mean profiles recorded during GATE (dotted).

GATE temperature sounding with $z_T = 27$ km. This is true even though the vertical temperature structure of the model's base-state atmosphere is somewhat different from that observed during GATE, especially above 4 km (see Fig. 4.2a).

4.5 General features of the simulation

4.5.1 Space-time evolution

Fig. 4.3 depicts the space-time evolution of P during the 15 day simulation. Starting from a state of initially random convection on day 1, deep convection spontaneously becomes organized within two large-scale convectively coupled gravity waves that propagate eastward at phase speeds of about 16 m s^{-1}. The waves are clearly evident by day 4 and persist throughout the remainder of the simulation (although one appears to grow stronger, while the other becomes weaker). The large-scale convective envelope associated with each wave extends roughly 1000 km in the horizontal and is made up of numerous

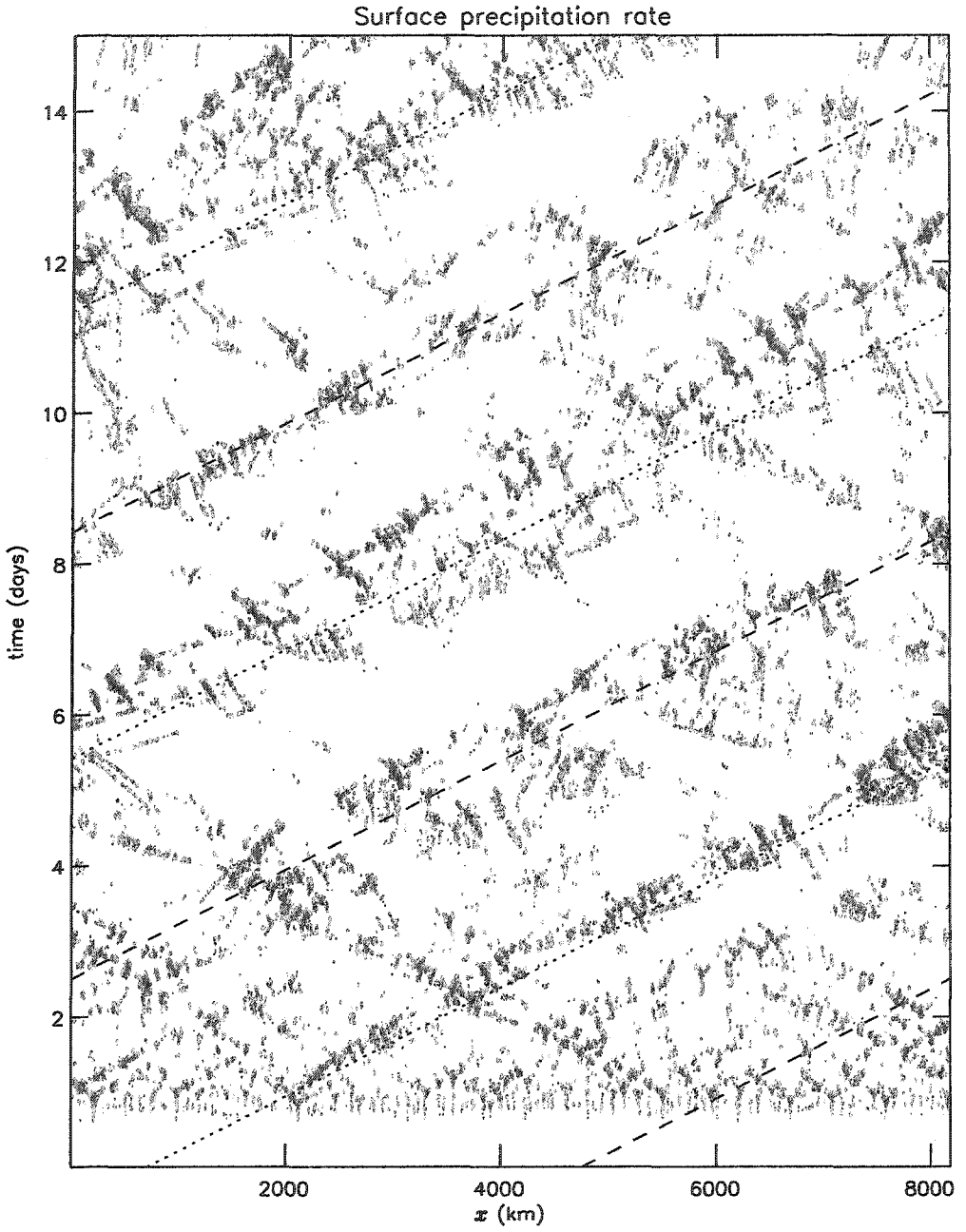

Figure 4.3 Space-time evolution of simulated surface precipitation rate. Shading increments increase logarithmically from 0.02 (light blue) to 20 mm hr^{-1} (black). Solid and dashed lines each denote a phase speed of 16 m s^{-1}.

mesoscale 'cloud clusters'. In general, the cloud clusters develop in succession to the east but propagate to the west at speeds typically in the range 7-11 m s^{-1}.

The space-time evolution of the precipitable water (*PW*), depicted in Fig. 4.4, provides evidence for the excitation of mesoscale gravity wave-packets by the cloud clusters. The packets appear as spatially localized regions of enhanced moisture and they travel at speeds in the range, 16-21 m s^{-1}. One can identify numerous instances where the passage of the packets coincides with the development of deep convection, suggesting that the former promote latter. Additional evidence to support the initiation of convection by gravity wave packets is presented later in Section 4.8.

4.5.2 Convective partitioning

The mass weighted and vertically integrated radiative cooling profile implies a net energy sink of about 138.0 W m^{-2}. This sink is balanced to within 4%, in a domain- and time-averaged sense, by a surface precipitation rate of 4.23 mm day^{-1} (122.0 W m^{-2}) and by a surface sensible heat flux of 11.4 W m^{-2}.

How much of the total rain volume falls in deep convective, stratiform, and mid-level convective regions of the simulation and what are the fractional areas covered by these different regions? As detailed in Table 4.1, deep convective regions typically cover just 1.3% of the domain but generate a substantial fraction (75%) of the total rain volume. The latter value is within 5% of that observed during the 80-day TOGA-COARE IOP (Rickenbach and Rutledge 1998) but about 15% larger than that observed during GATE (Cheng and Houze, 1979). Of the remaining 25% of the total rain volume, 11% falls in mid-level convective regions covering 4% of the domain, while 14% falls from more wide-spread stratiform regions covering 16% of the domain.

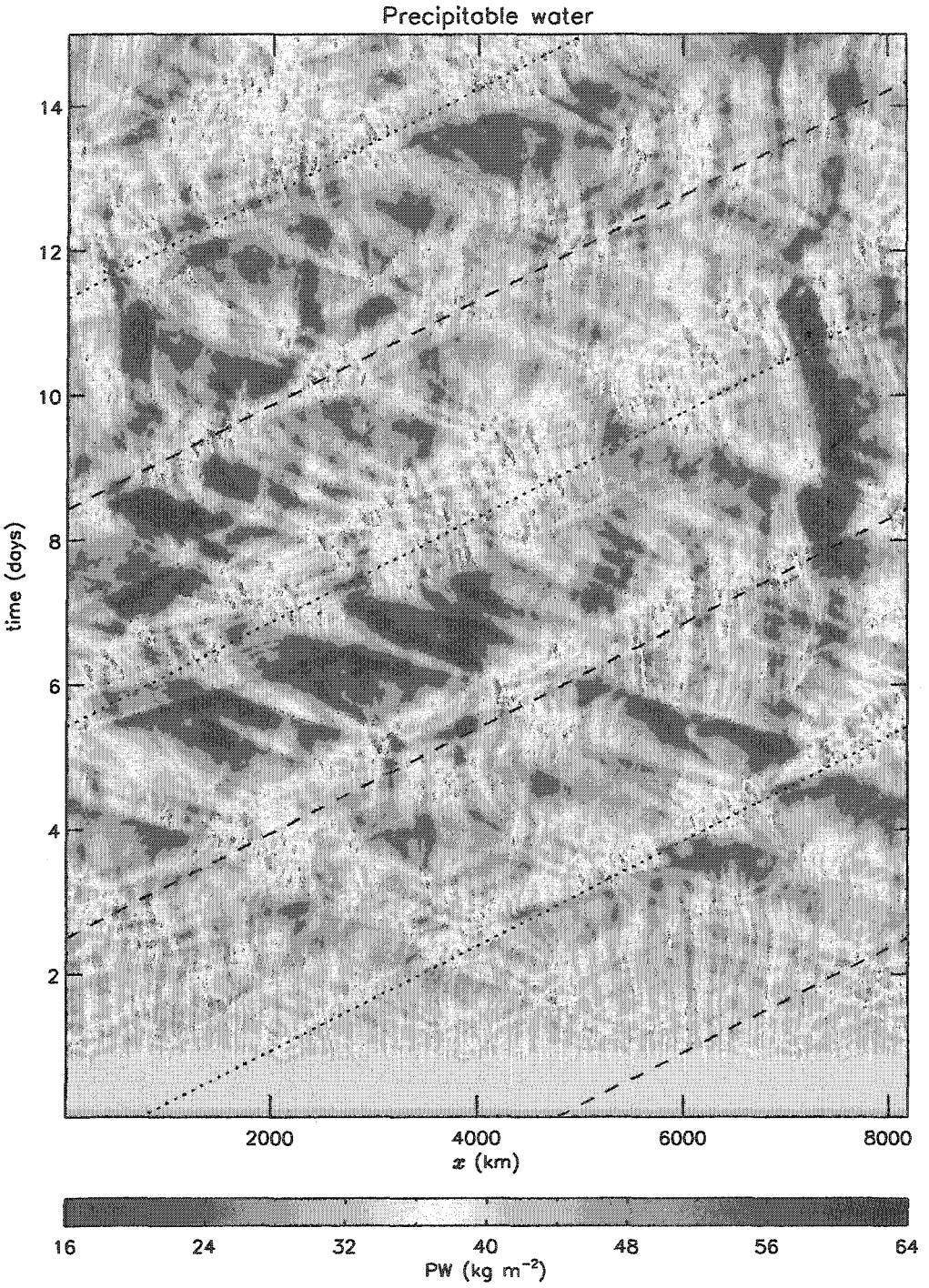

Figure 4.3 Similar to Fig. 4.2 but for precipitable water.

Table 4.1: Fraction of domain covered by (top row) and fraction of total surface precipitation volume (middle row) generated in deep convective, stratiform, mid-level convective, and shallow convective regions.

	Deep convective	Stratiform	Mid-level convective	Shallow convective
Area fraction (%)	1.3	16.0	3.7	18.2
P_{vol} fraction (%)	75.3	13.5	11.2	0.0

4.5.2.1 Convective heating profiles

The domain- and time-averaged latent heating profile in deep convective regions, given by the solid curve in Fig. 4.5a, shows warming in the layer, 1-12 km, and cooling near the surface. The implied top-height of deep convective cores, roughly 12 km, is similar to that observed in the tropical Atlantic during GATE (Houze and Cheng 1977), a region where the SSTs are comparable those imposed in the simulation. On the other hand, it is about 3-4 km below that observed over the equatorial western Pacific during TOGA-COARE (Demott and Rutledge 1998), where the SSTs are typically several degrees warmer.

The stratiform profile, given by the dotted curve in Fig. 4.5a, shows relatively strong cooling in the lower troposphere and weak warming in the upper troposphere. The shape of the profile, with intense destabilization at low-levels and moderate stabilization at mid-levels, suggests that stratiform heating processes should tend to strongly promote the development of mid-level convection (e.g. Mapes 2000). The averaged latent heating profile in mid-level convective regions, given by the dashed curve, is not inconsistent with this idea. The profile shows warming across the depth the lower troposphere with a peak in

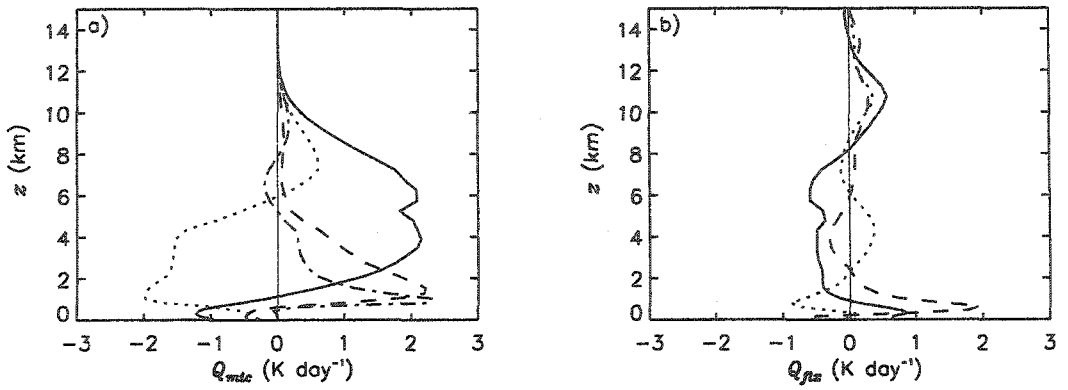

Figure 4.5 a) Domain- and time-averaged profiles of Q_{mic} in deep convective (solid), stratiform (dotted), mid-level convective (dashed), and shallow convective (dot-dashed) regions of the simulation. b) Similar to a) but for the heating due to the convergence of the sensible heat flux (Q_{1flx}) and where the profiles of Q_{1flx} in shallow convective and mid-level regions have been combined to give the dashed curve.

roughly the same location and of roughly the same magnitude as the stratiform profile. The implied penetration depth of mid-level convection is at roughly the same level as where the stratiform heating profile first changes from positive to negative (~ 6 km).

The averaged latent heating profile in shallow convective regions, given by the dot-dashed curve, also shows warming in the lower troposphere but with values decaying more rapidly upwards above a sharp low-level maximum at about 1 km; there is also a weak warming-over-cooling signature in the upper troposphere. The latter feature is presumably associated with mesoscale circulations in non-precipitating anvil clouds. The sharp low-level maximum, on the other hand, is thought to reflect the existence of shallow cumuli in their initial stages of development. This idea is supported by the fact that the averaged P in regions previously diagnosed (i.e, 0.5 hrs earlier) as shallow convective is 0.9 mm day^{-1}. Note: owing to the similarities between the heating profiles in non-precipitating shallow convective and in mid-level convective regions, the former type of convection is hereafter subsumed into the latter.

Fig. 4.5b is similar to Fig. 4.5a but showing the apparent heating due to the convergence of the sensible heat flux, i.e., $Q_{1flx} = -\nabla \cdot (\bar{\rho}\underset{\sim}{u}'T')/\bar{\rho}$, where the primes hereafter denote perturbations about the domain-average at each level. In deep convective regions, there is relatively strong warming in the upper-troposphere and in the lowest 1 km with cooling in between. The heating profiles in mid-level convective and stratiform regions also both exhibit warming in the upper-troposphere between 8 and 14 km. Below 8 km, the profiles are almost mirror opposites of each other, such that the sum of the two (not shown) primarily consists of warming in the lowest 1 km.

4.5.2.2 Convective heating spectra

The curves in Fig. 4.4a depict the domain- and time-averaged spectra of $\partial\Phi_n^{mic}/\partial t$, i.e., the forced geopotential due to latent heating, in the three different convective regions of the simulation. The sign convention is chosen such that negative values of the forced geopotential imply a negative pressure tendency at the surface. The averaged spectrum in deep convective regions shows a peak positive projection at c_n = 45 m s^{-1} (a first internal mode) and a peak negative projection at c_n = 16 m s^{-1} (a third internal mode). The stratiform spectrum shows a relatively broad positive projection across c_ns in the range, 9-60 m s^{-1}, with the largest response occurring between 16 and 23 m s^{-1}. Since the amplitude of the response at 16 m s^{-1} is only about twice that in deep convective regions, we can conclude that deep convective and stratiform latent heating processes both tend to excite this mode. The averaged spectrum in mid-level convective regions is qualitatively similar to that in stratiform regions but with opposite sign.

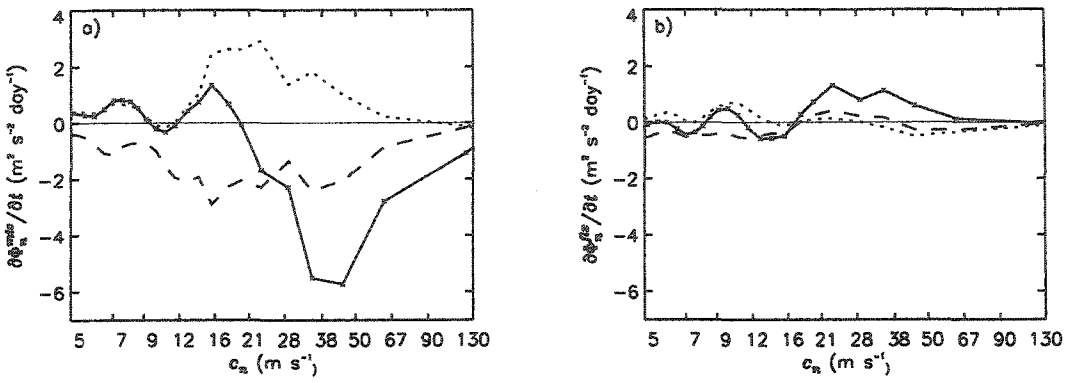

Figure 4.6 Domain- and time-averaged spectra of $\partial\Phi_n^{mic}/\partial t$ (a) and $\partial\Phi_n^{1flx}/\partial t$ (b) in deep convective (solid), stratiform (dotted), and mid-level convective (dashed) regions. Note: plotting symbols denote actual location of eigenvalues, while curves have been added for viewing purposes.

Fig. 4.6b is similar to Fig. 4.6a but showing the spectra of $\partial\Phi_n^{1flx}/\partial t$, i.e., the forced geopotential due to the convergence of sensible heat flux. Comparing the solid line in Figs. 4.6b with the dotted line in Fig. 4.6a, we see that for $c_n > 20$ m s^{-1} the averaged spectrum of $\partial\Phi_n^{1flx}/\partial t$ in deep convective regions is very similar to the spectrum of $\partial\Phi_n^{mic}/\partial t$ in stratiform regions. This is explained by the fact that the vertical profile of Q_{flx} in deep convective regions is characterized by warming (cooling) at upper- (lower-) levels and thus, is "stratiform-like" in appearance. For higher mode numbers, both the deep convective and mid-level convective spectra show a relatively strong negative projection in the range 12-16 m s^{-1}. The significance of this negative projection will become evident in Section 4.6 which discusses the vertical normal mode-energetics of the simulation. First, however, we examine the structure and energetics of the large-scale waves in physical space.

4.6 Time-mean wave structure and energetics: analysis in physical space

4.6.1 Wave structure

The time-mean structure of the large-scale waves is assessed by averaging model output between days 2 and 15 in a reference frame moving at 16 m s^{-1}. Figs. 4.7a and b depict the resulting spatial distributions of $\{u'\}$ and $\{T'\}$, respectively, where brackets hereafter denote a time-average in the moving frame of reference. The curves appearing at the bottom of each panel depict the spatial distribution of $\{P\}^*$, where the '*' hereafter denotes the application of a low-pass (Lanczos) filter with a cutoff wavelength of 400 km. Fig. 4.7 clearly reveals the existence of two convectively coupled gravity waves. The convective envelope associated with the first wave, later referred to as Envelope S (where S strands for strong) extends between roughly 1500 and 3700 km, while that of the second, later referred to as Envelope W (where W stands for weak) extends between roughly 6500 and 500 km. As with observations of convectively coupled Kelvin waves, the horizontal wind and temperature perturbations associated with each wave exhibit boomerang-like structures with the elbow of the boomerang located in the upper troposphere. Convection is strongest when air is anomalously cool in the lower troposphere, anomalously warm in the upper troposphere, and anomalously cool at the level of the tropopause. At low-levels, convergence of the horizontal winds leads convection by about a quarter wave-cycle, while at upper-levels, divergence lags convection by about the same amount. Water vapor mixing ratio anomalies, depicted in Fig. 4.4c, show relatively large amplitude fluctuations in the lower troposphere and weaker fluctuations aloft (unlike the predictions of the mois-

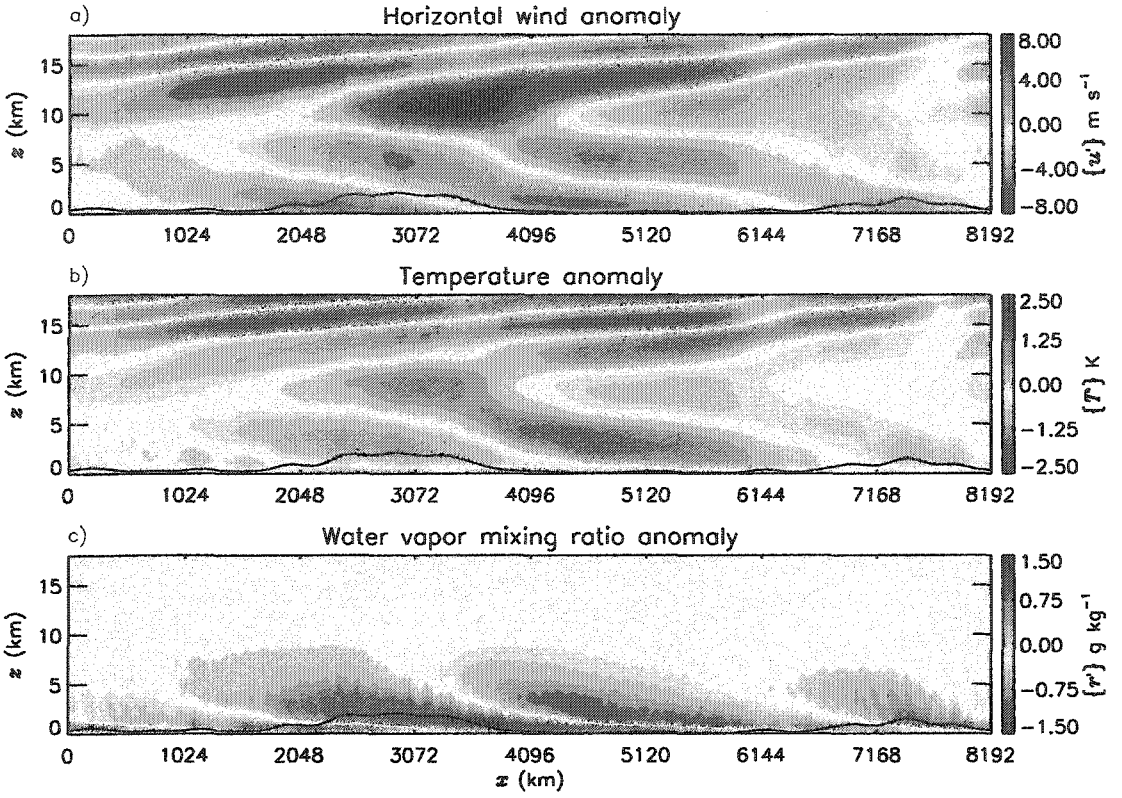

Figure 4.7 Longitude-height cross-sections of $\{u'\}$ (a), $\{T'\}$ (b), and $\{r'\}$ (c). Solid curves at the bottom of each panel denote $\{P\}^*$ (maximum amplitude of 0.58 mm hr^{-1}).

ture convergence model; see Fig. 3.4c). The anomalies tilt westward with height in a fashion similar to that of the low-level temperature field. Convection is strongest (weakest) when air is relatively dry (moist) in the boundary layer and moist (dry) aloft.

Comparing Fig. 4.7 with Fig. 3.10, we see that the structure of the dynamical signals associated with the waves is broadly consistent with that of the MI-modes under stratiform adjustment. The two most notable differences are that, in the simulation, the tilting of the horizontal wind anomalies is much "smoother" and, also, the tilting of the moisture anomalies increases dramatically near the surface. Presumably, the latter difference is due to the

fact that boundary layer processes and convective downdrafts are not represented in the moisture relaxation model.

4.6.1.1 Surface precipitation

Fig. 4.8a shows that $\{P_{st}\}^*$, i.e., the averaged surface precipitation rate in stratiform regions, is highly correlated with, but lags slightly behind, that in deep convective regions, $\{P_{dc}\}^*$. A typical magnitude of the phase shift is assessed here by calculating the lagged cross-correlation between $\{P_{dc}\}^*$ and $\{P_{st}\}^*$ for lags in the range -200 to +200 km. The results, given by the solid curve in Fig. 4.8c, suggest that deep convection typically leads stratiform heating by about 100 km (or approximately 9°, assuming a wavelength of 4,000 km). This phase shift implies a stratiform adjustment time of about 1.75 hrs. Fig. 4.5b, along with the dotted curve in Fig. 4.8c, shows that $\{P_{mc}\}^*$, i.e., the averaged surface precipitation rate in mid-level convective regions, is also highly correlated with, but in this case, is in phase with (or slightly leads) that in deep convective regions.

The existence of a lag between stratiform and deep convective heating processes supports the simple model parameterization of stratiform heating processes proposed by Mapes (2000).

4.6.1.2 Precipitable water and moisture convergence

The moisture relaxation model developed in Chapter 3 is based on the assumption that variations in deep convection are linearly related to variations in the column-integrated moisture anomalies. While Figs. 4.9a and b demonstrate that there is indeed a strong relationship between $\{PW\}$ and $\{P_{dc}\}^*$, they also show that former distribution typically lags

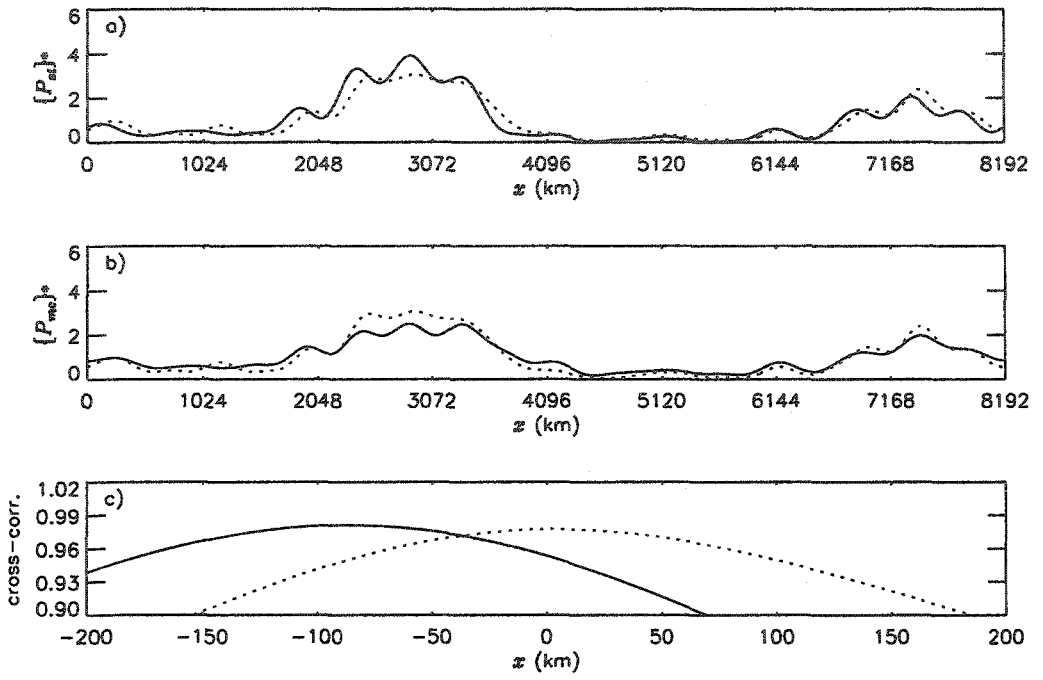

Figure 4.8 a) Normalized distributions of $\{P_{st}\}^*$ (solid) and $\{P_{dc}\}^*$ (dotted). b) Similar to a) but showing $\{P_{mc}\}^*$. c) Lagged cross-correlation between $\{P_{st}\}^*$ and $\{P_{dc}\}^*$ (solid) and between $\{P_{st}\}^*$ and $\{P_{mc}\}^*$ (dotted).

the latter by about 50-100 km. The existence of such a lag implies that fluctuations in column-integrated moisture anomalies may be a result, rather than a cause, of deep convection. In Fig. 4.9c, we also see that, rather than being described by a simple linear expression, the relationship between $\{P_{dc}\}^*$ and $\{PW\}$ can instead be well fitted, in a least-squares sense, by the second-order polynomial:

$$P_{fit} = \overline{\{P_{dc}\}} + \frac{(\{PW\} - PW_0)}{\tau_r}\left[1 + \frac{\{PW\} - PW_0}{PW_1}\right], \tag{4.4}$$

where the bar denotes a domain average and PW_0 = 33.3 kg m^{-2}, τ_r = 10.8 hrs, and PW_1 = 4.95 kg m^{-2}.

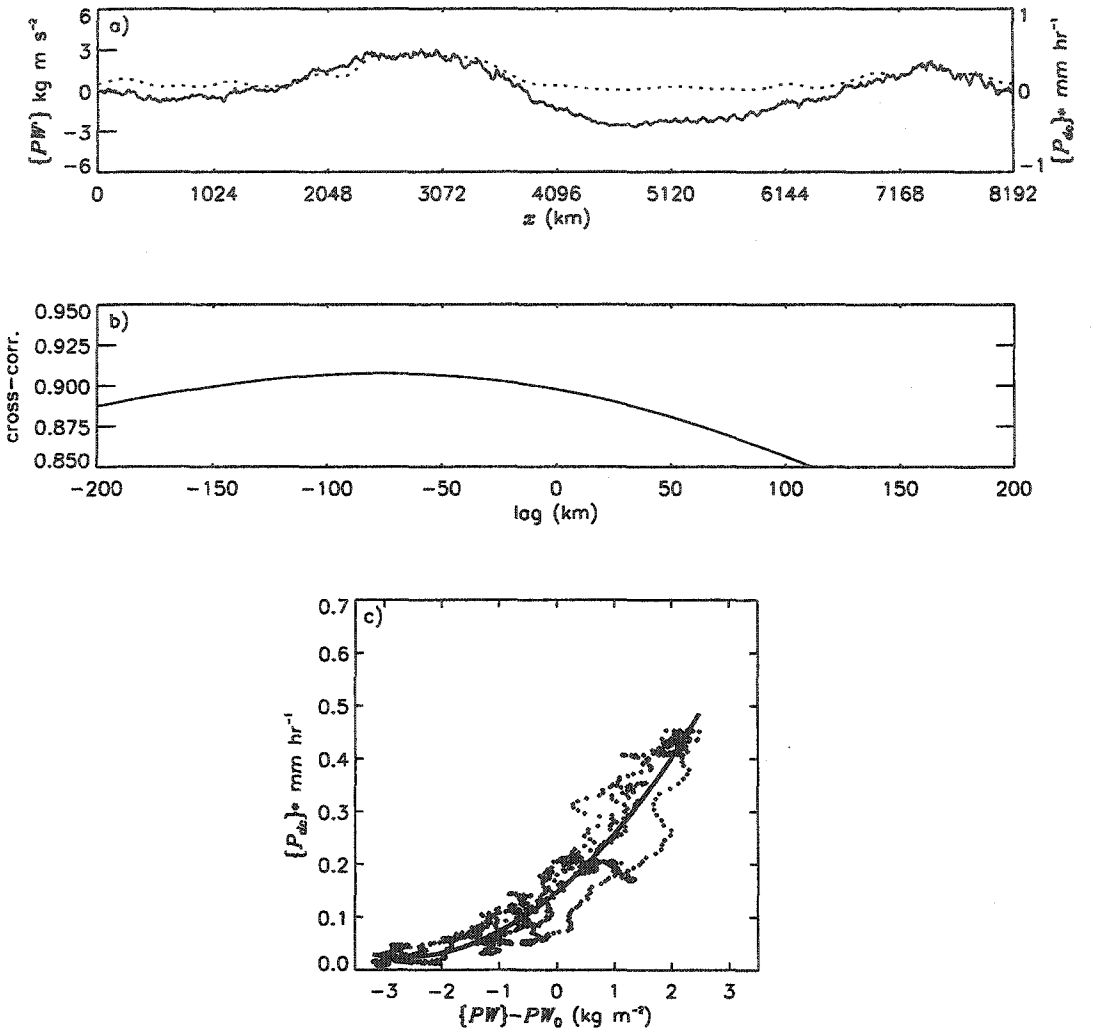

Figure 4.9 a) Spatial distributions of $\{PW'\}$ (solid) and $\{P_{dc}\}^*$ (dotted). b) Lagged cross-correlation between $\{PW'\}$ and $\{P_{dc}\}^*$.c) Scatter-plot of $\{P_{dc}\}^*$ versus $\{PW'\}$, where the solid line depicts a second-polynomial curve-fit of the data given by (4.4). See text for details.

Figs. 4.10a and b are similar to Figs. 4.9a and b but showing the relationship between $\{P_{dc}\}^*$ and the column-integrated moisture convergence, $\{R_{conv}\}^*$. Note: a cutoff wavelength of 600 km, rather than 400 km, was used when filtering R_{conv}, since the standard distribution was still somewhat noisy. Fig. 4.10b shows that the correlation between $\{R_{conv}\}^*$ and $\{P_{dc}\}^*$ is strongest when the former leads the latter by about 300 km, implying that

fluctuations in deep convection typically lag those in the column-integrated moisture convergence by about 5 hrs. Thus, the assumption that the convective heating and moisture convergence are directly related to one another at each moment in time, as made in "classical" wave-CISK models, as well as the moisture convergence model developed in Chapter 3, is not valid in the simulation.

4.6.1.3 CAPE, CIN, and surface heat flux

Phase relationships between deep convection and other variables, i.e., {CAPE}, {CIN}, and the total (latent + sensible) surface heat flux {*SHF*}, are depicted in Fig. 4.12. {CAPE} is seen to be largest (smallest) out ahead of (towards the rear) of the convective envelopes, while {CIN} is smallest (largest) towards the front (just behind) the convective envelopes. The distribution of {*SHF*} is qualitatively similar to that of $\{P_{dc}\}^*$ but with the former lagging the latter.

The phase relationships between deep convection, CAPE, and CIN are consistent with those predicted by the stratiform instability model of Mapes (2000). A rigorous assessment of this model, however, requires a knowledge of the distribution of his "deep convective triggering energy" variable *K*. This is because in Mapes' model, variations in deep convective heating are parameterized as

$$q_{dc} = M \exp\left[\frac{-\mathrm{CIN}}{K}\right] \sqrt{\frac{\mathrm{CAPE}}{\mathrm{CAPE}_0}}\, q_{rad}^{dc} , \tag{4.5}$$

where the subscript 0 denotes a climatological background value, M is a normalization factor that determines how inhibited the convection is on average, and q_{rad}^{dc} is the projec-

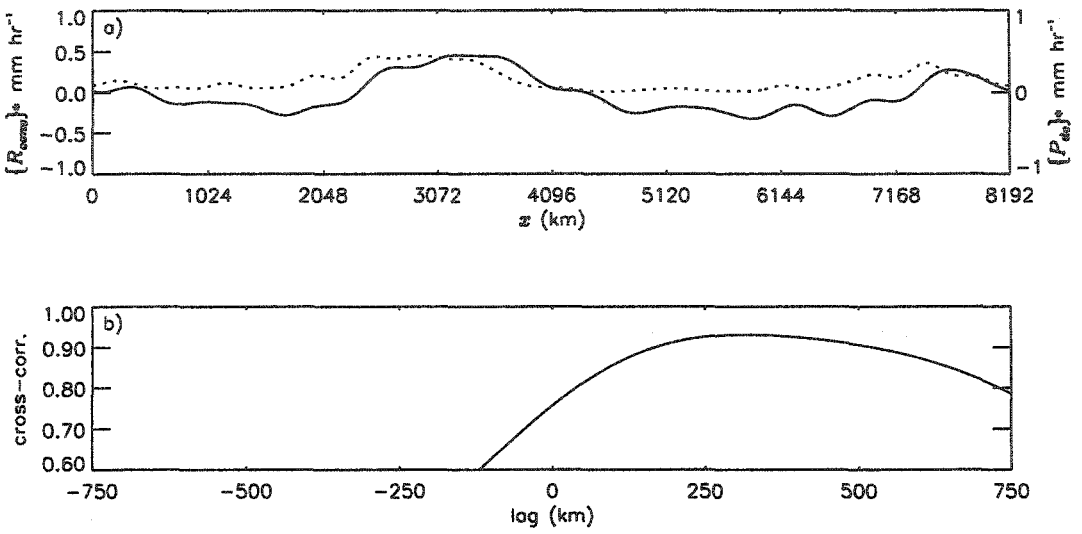

Fig. 4.10 Similar to Figs. 4.9a and b but for column-integrated moisture convergence, $\{R_{conv}\}^*$. Note that a cut-off wavelength of 600 km, rather than 400 km, was used when filtering R_{conv}

tion of the radiative cooling rate onto the first tropospheric internal mode. (4.5) can be tested using model output, provided that we have a definition of K.

Mapes states that, in addition to its climatological background value, K should have four main parts: "gust front vigor; fluctuations of θ_e (the equivalent potential temperature) about its grid-box mean value; density fluctuations in the lower-tropospheric inhibition layer; and convective organization". Since it is not clear how to objectively measure each of these components in the simulation (and then convert them into a bulk value of K), the following quantity is used here instead:

$$E_b = \frac{\int_0^{500\text{ m}} \left[\frac{\bar{\rho}}{2}\underset{\sim}{u}' \cdot \underset{\sim}{u}' + \frac{\bar{\rho}}{2}\left(\frac{b_v}{\bar{N}_v}\right)^2\right] dz}{\int_0^{500\text{ m}} \bar{\rho}\, dz}, \tag{4.6}$$

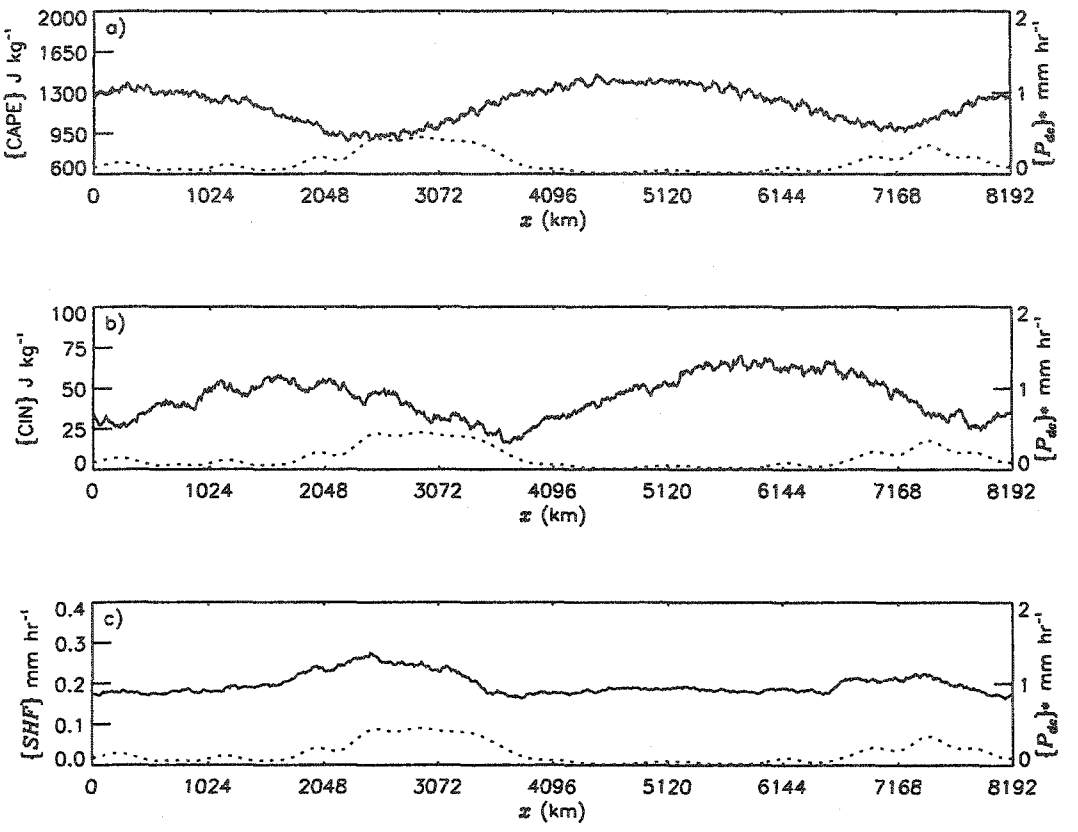

Fig. 4.11 Phase relationships between $\{P_{dc}\}^*$ (dotted) and {CAPE} (a), {CIN} (b), and {*SHF*} (c).

where $b_v = g(T'/\overline{T} + 0.61r')$ is the virtual buoyancy in the anelastic system and $\overline{N}_v^2$ is a measure of the Brunt-Vaisala frequency including the effects of moisture on density, given by

$$\overline{N}_v^2 \equiv g\left(\frac{1}{\bar{\theta}}\frac{d}{dz}\bar{\theta} + 0.61\frac{d}{dz}\bar{r}\right). \tag{4.7}$$

As discussed in the next section, the first and second terms in square brackets on the RHS of (4.6) are the kinetic energy (*KE*) and available potential energy (*APE*), respectively. Thus, E_b can be regarded as a bulk measure of the energy in the boundary layer that is available for overcoming CIN.

In Fig. 4.12a, we see that the distribution of $\{E_b\}$, given by the solid curve, is qualitatively similar to that of $\{P_{dc}\}^*$ but with the former slightly lagging the latter. This relationship suggests that convection acts to strongly generate energy in the boundary layer, an idea that is confirmed later in the next section. Comparing the solid and dotted curves in Fig. 4.12a, we see that, within the heavily precipitating portions of the two convective envelopes, values of $\{E_b\}$ are greater than {CIN}, while outside of these regions, they are smaller than {CIN}. While this distribution is consistent with Mapes' theory, the results are highly sensitive to the choice of averaging depth used in the calculation E_b and CIN. For example, when these variables are calculated using output from only the lowest model layer, $\{E_b\}$ is found to exceed {CIN} everywhere (not shown).

The solid line in Fig. 4.12b depicts the distribution of deep convective precipitation expected on the basis of (4.7), i.e.,

$$P_{test1} = M \exp\left[-\frac{\{\mathrm{CIN}\}}{\{E_b\}}\right] \sqrt{\frac{\{\mathrm{CAPE}\}}{\overline{\{\mathrm{CAPE}\}}}}\,\overline{\{P_{dc}\}}, \tag{4.8}$$

where, following Mapes (2000), the normalization constant M has been computed as

$$M = \exp\left[\frac{\overline{\{\mathrm{CIN}\}}}{\overline{\{E_b\}}}\right] = 3.5. \tag{4.9}$$

There is marginally good agreement between P_{test1} and $\{P_{dc}\}^*$, except in the range, 2400-5000 km, where P_{test1} is too small (large) within (out ahead of) Convective Envelope S.

A possible explanation for this failure is that (4.5) does not account for the effects of moisture on deep convective development[1]. One way of testing this idea would be to mod-

1. Mapes (2000) formally recognized that the effects of moisture on convective development should be included in his stratiform instability model, although his study neglected them for simplicity.

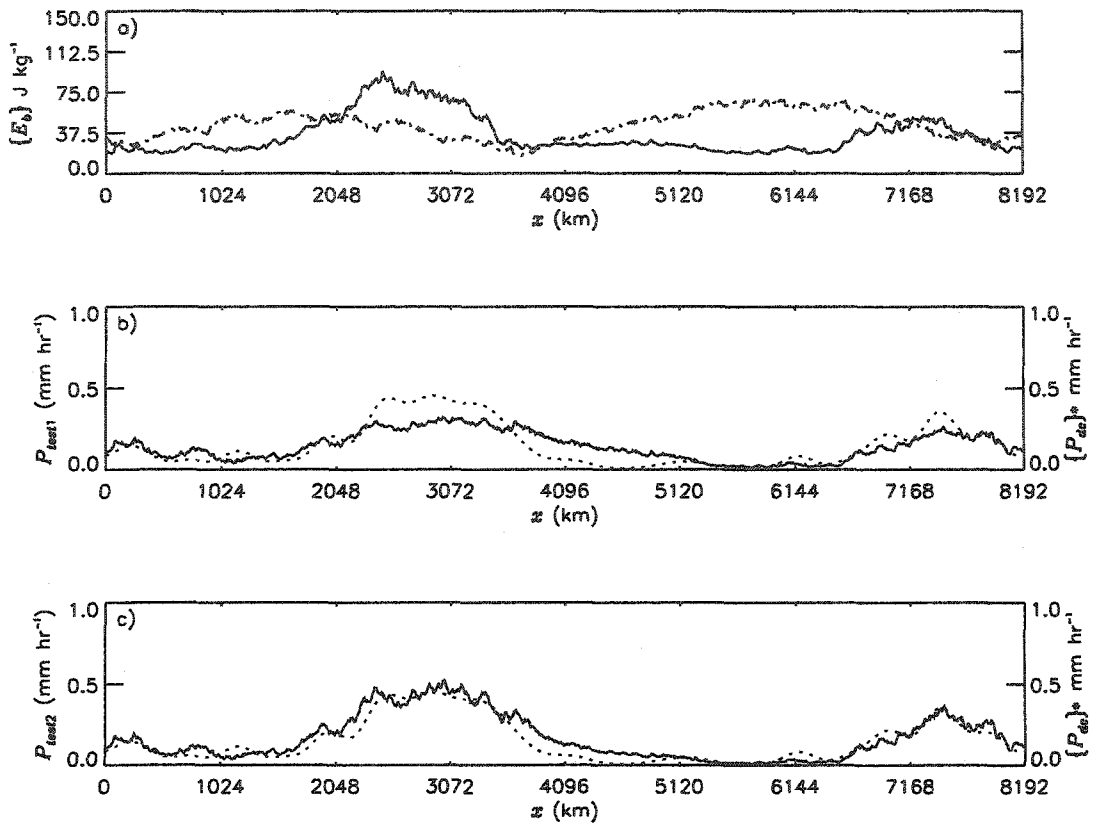

Figure 4.12 a) Distributions of $\{E_b\}$ (solid) and {CIN} (dotted). b) Distributions of P_{test1} (solid) and $\{P_{dc}\}^*$ (dotted). c) Similar to b) but for P_{test2}.See text for details.

ify (4.7) by replacing its dependence on CAPE with that of a variable that accounts for the the effects of entrainment on parcel buoyancy. Since such a task lies beyond the scope of the current research, let's instead simply modify (4.8) as follows

$$P_{test2} = M\left(\frac{\{PW\}}{\overline{\{PW\}}}\right)^6 \exp\left[-\frac{\{\mathrm{CIN}\}}{\{E_b\}}\right]\sqrt{\frac{\{\mathrm{CAPE}\}}{\overline{\{\mathrm{CAPE}\}}}}\,\overline{\{P_{dc}\}}. \tag{4.10}$$

While this modification is arbitrary, Fig. 4.12c shows that it leads to much better agreement within the heavily raining portions of the two convective envelopes. On the other hand, there is still a slight discrepancy between P_{test2} and $\{PR_{dc}\}^*$ towards the leading edge of Envelope S, where the atmosphere is relatively dry.

4.6.2 Energetics

The inviscid statement expressing conservation of (*KE*) in the moist anelastic system is given by

$$\frac{D}{Dt}KE = p_w + G_T + G_p + G_L \tag{4.11}$$

Here, $D()/Dt$ is the material derivative, $p_w = -\nabla \cdot p'\underset{\sim}{u}'$ is the pressure work, and G_T, G_p, and G_L are buoyancy generation terms associated with virtual temperature, pressure, and loading effects, respectively. The generation terms are given by

$$G_T = wg\left(\frac{T'}{\overline{T}} + 0.61r'\right), \tag{4.12}$$

$$G_p = -wg\frac{p'}{\overline{p}}, \text{ and} \tag{4.13}$$

$$G_L = -wg(r_p + r_c), \tag{4.14}$$

where r_p and r_c are the mixing ratios of precipitation and cloud condensate.

In the CRM, the dry static energy ($s = c_pT + gz$) and water vapor mixing ratio are both conserved quantities in the absence of sources and sinks. That is,

$$\frac{D}{Dt}s = c_pQ_{mic} \text{ and} \tag{4.15}$$

$$\frac{D}{Dt}r = -C + E, \tag{4.16}$$

where C and E are the rates of condensation and evaporation in the interior of the fluid, respectively, and the effects of surface sensible and latent heat fluxes and radiative cooling have been neglected for simplicity.

Considering perturbations about a time-invariant base state, (4.15) and (4.16) can be combined to obtain the following statement expressing approximate conservation of the available potential energy (*APE*)

$$\frac{D}{Dt}APE = -G_T + EAPE_{mic} + \varepsilon . \tag{4.17}$$

Here, ε is a non-linear correction term that arises from bringing $\overline{T}$ and $\overline{N}_v^2$ inside the vertical derivative, while $EAPE_{mic}$ is the eddy generation of *APE* due to latent heating, given by

$$EAPE_{mic} = \frac{gb_v(1 - c_p\overline{T}/L)Q_{mic}}{\overline{T}\overline{N}_v^2} . \tag{4.18}$$

Combining (4.11) and (4.17), we arrive at a statement expressing approximate conservation of the total energy, i.e.,

$$\frac{D}{Dt}E = p_w + EAPE_T^{mic} + EAPE_r^{mic} + G_P + G_L + \varepsilon \tag{4.19}$$

where $EAPE_T^{mic}$ and $EAPE_r^{mic}$ represent the parts of $EAPE_{mic}$ due to temperature and moisture effects on buoyancy, respectively.

Fig. 4.13a depicts the domain-averaged evolution of *KE* and *APE* during the 15-day simulation. Shortly after convection begins, *KE* and *APE* both increase more-or-less linearly with time out to day 6, decrease by roughly 30-40% between days 6 and 10, and then remain fairly steady thereafter. A comparison of the solid and dashed curves in Fig. 4.13b shows that, between days 1 and 4, the total energy ($E = KE + APE$) increases exponentially at a rate of about 0.52 day^{-1}, implying a growth rate of about 0.25 day^{-1}. Referring back to Fig. 3.9b, we see that the latter value is close to that predicted by the moisture relaxation

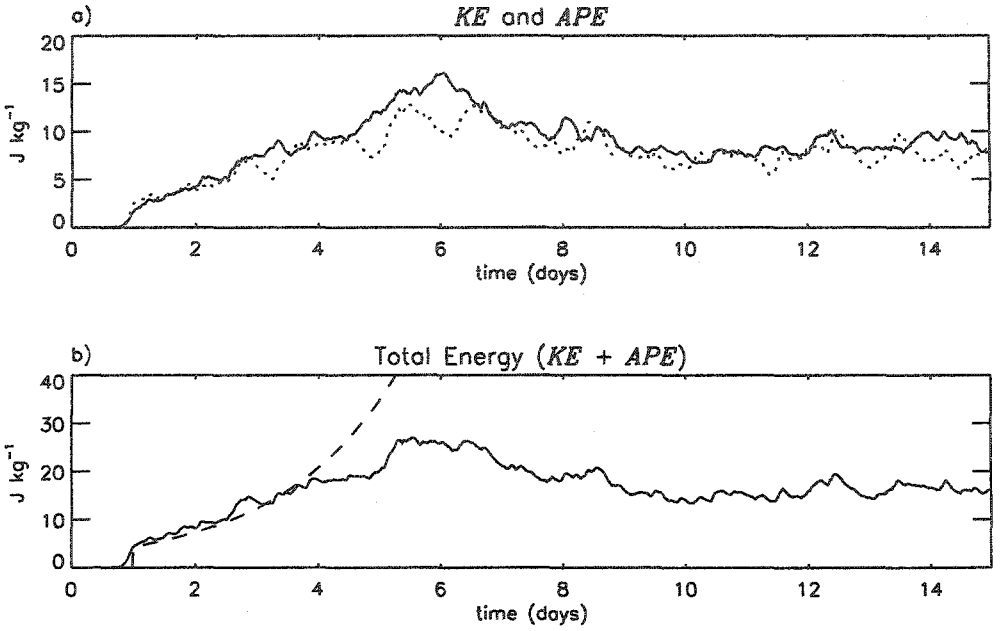

Figure 4.13 a) Domain-averaged evolution of *KE* (solid) and *APE* (dotted). b) Sum of curves in a) along with exponential (dashed) growth rate of 0.52 day^{-1}starting on day 1.

model under stratiform adjustment for MI-modes with wavelengths in the range 3,000-5,000 km and τ_r = 10 hrs.

4.6.2.1 Energy production

The solid curve in Fig. 4.14a depicts the domain- and time-averaged profile of $EAPE_T^{mic}$ diagnosed in deep convective regions of the simulation. Owing to a positive correlation between Q_{mic} and T' (e.g. Fig. 4.14c), the profile shows a strong source of energy both in the upper-troposphere and near the surface. The comparatively larger production near the surface can be explained by the fact that $\overline{N}_v^2$ is roughly an order of magnitude smaller in the boundary layer than aloft. In the lower free troposphere, the sink due to $EAPE_T^{mic}$ is largely offset by the source due to $EAPE_r^{mic}$, i.e., latent heating being posi-

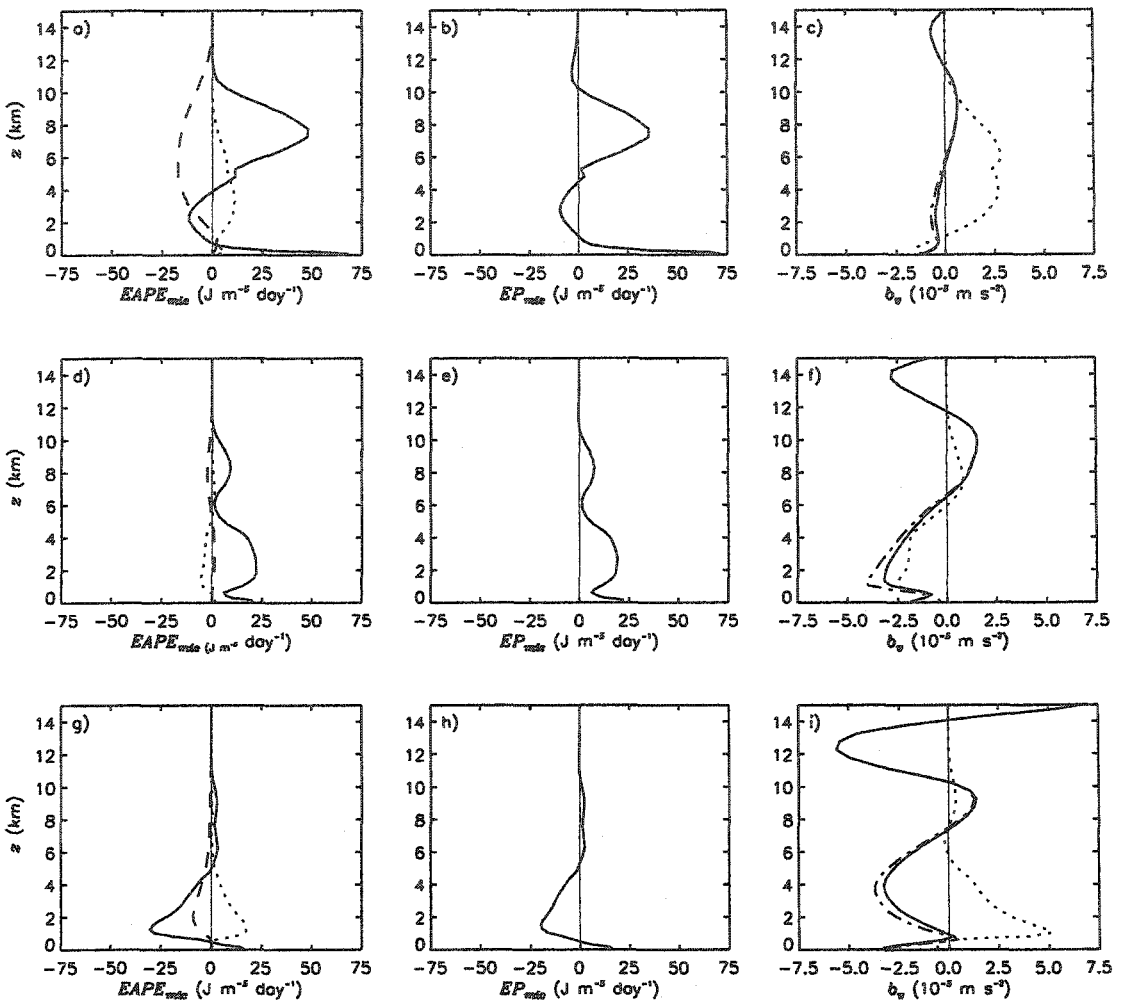

Figure. 4.14 Left column: Domain- and time-averaged profiles of $EAPE_T$ (solid), $EAPE_t$ (dotted), and W_t (dashed) in deep convective (top), stratiform (middle), and mid-level convective (bottom) regions. Middle column: Sum of the profiles appearing in the left column. Right column: Domain- and time-averaged profiles of b_v (solid) and $b_T = gT'/\overline{T}$ (dot-dashed) along with Q_{mic} (dotted).

tively correlated with moisture anomalies. Owing to the effects of hydrometeor loading, however, the shape of the total energy production profile, i.e., $EP_{mic} = EAPE_{mic} + G_L$, depicted in Fig. 4.14b, is broadly similar to that of $EAPE_T^{mic}$.

Figs. 4.14c and d show that, in stratiform regions, the energy production is generally positive at all levels and is dominated by $EAPE_T^{mic}$. Above about 6 km, the production is a result of air being heated where it is already warm, while, below this level, it is due to air being cooled where it is already cold (Fig. 4.14e).

The profile of EP_{mic} in mid-level convective regions, depicted in Fig. 4.14h, shows a strong sink of energy in the lower free troposphere with the largest destruction occurring at about 1.5 km. Between 0.5 and 2 km, the sink is mainly due to $EAPE_T^{mic}$, while, between 2 and 5 km, both $EAPE_T^{mic}$ and W_l are important (Fig. 4.14g). As in deep convective regions, the source due to $EAPE_r^{mic}$ plays an important role in offsetting the sinks due to $EAPE_T^{mic}$ and W_l.

Overall, Fig. 4.14 suggests that moist processes associated with deep convection and stratiform precipitation both act to maintain the energy of the large-scale waves, while those associated with mid-level convection act to remove it.

In addition to generating and destroying energy, convection can also act to re-distribute energy on regional scales via convective transports. The advective tendencies of *APE* and KE_u (i.e., the horizontal part of *KE*) can be written, without approximation, as apparent eddy generation terms of the form

$$EAPE_{flx} = \frac{g\bar{\rho}}{\overline{T}\overline{N}_v^2} b_v \left[Q_{1flx} + 0.61\overline{T}\frac{Q_{2flx}}{L} \right] \text{ and} \tag{4.20}$$

$$EKE_{flx} = -\bar{\rho}u'F_{flx}. \tag{4.21}$$

respectively. Here, $Q_{2flx} = -\nabla \cdot (\bar{\rho}\underline{u}'Lr')/\bar{\rho}$ is the apparent moistening due to convergence of the turbulent moisture flux, while $F_{flx} = -\nabla \cdot (\bar{\rho}\underline{u}'u')/\bar{\rho}$ is the apparent acceler-

ation of the horizontal flow due to convergence of the turbulent horizontal momentum flux. A comparison of the first and second terms appearing on the RHS of (4.21) (not shown) reveals that the former is typically much larger than the latter. Thus, to a good degree of approximation,

$$EAPE_{flx} \cong \frac{g\bar{\rho}}{\bar{T}\bar{N}_v^2} b_v Q_{1flx}. \tag{4.22}$$

The curves appearing in Fig. 4.15a depict the domain- and time-averaged profiles of $EAPE_{flx}$ in deep convective (solid), stratiform (dotted), and mid-level convective (dashed) regions of the simulation. The deep convective profile shows a relatively strong source of energy at 10 km and strong sinks near the surface and at 7 km. Comparing Fig. 4.5b with the right panel of 4.14, we see that the shape of the profile in deep convective regions, as well as those in stratiform and mid-level convective regions, is generally consistent with that expected on the basis of the averaged profiles of Q_{1flx} and b_v. Owing to an almost perfect cancellation between $EAPE_{flx}$ in stratiform and mid-level convective regions (in the layer, 1-7 km), Fig. 4.15b shows that sum of the profiles in the three regions is broadly similar to that in deep convective regions. The shape of this profile suggests that convection acts to remove large amounts of *APE* from mid-levels and deposit it at upper-levels between 8 and 12 km.

The dotted line in Fig. 4.16b depicts the domain- and time-averaged profile of the horizontal wind in all convective (i.e., deep + stratiform + mid-level) regions of the simulation. Consistent with Fig. 4.7a, the profile shows that cloud clusters tend to occur in the presence of mid-level easterlies sandwiched between upper- and lower-level westerlies. The averaged profile of EKE_{flx}, given by the solid line, shows that convection acts to

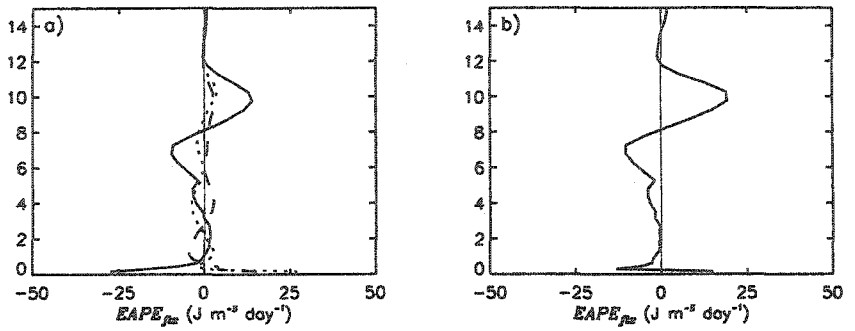

Fig. 4.15 a) Domain- and time-averaged profiles of $EAPE_{flx}$ in deep convective (solid), stratiform (dotted), and mid-level convective (dashed) regions of the simulation. b) Sum of the profiles in a).

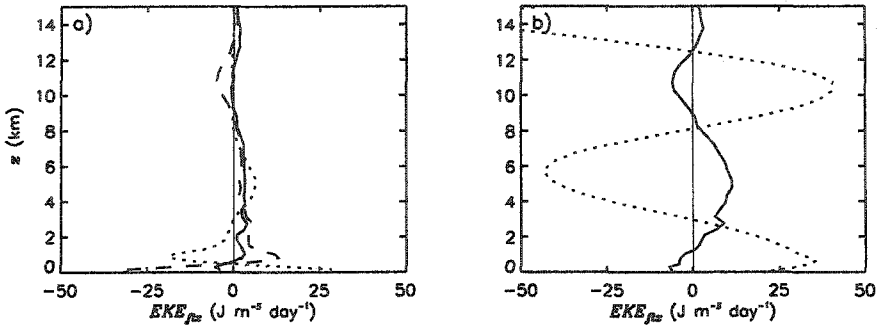

Figure 4.16 Similar to Fig. 4.15 but for EKE_{flx} and with domain- and time-averaged profile of u in all convective regions (i.e., deep convective + stratiform + mid-level convective) given by the dotted curve in b).

increase KE_u between ~ 1-8 km while decreasing it both in the lowest 1 km and between 8 and 12 km. In Fig. 4.16a, we see that horizontal momentum transports in each of three convective regions are important for producing the apparent source of KE_u in the middle troposphere. The sink between 8-12 km, on the other hand, is primarily due to transports in mid-level convective regions.

Taken together, Figs. 4.15 and 4.16 suggest that convective transports of heat and momentum may play an important role in the dynamics of the simulated waves. The con-

vective transport of momentum is, however, neglected in most simple tropical wave models including the ones developed here.

4.7 Time-mean wave structure and energetics: analysis in spectral space

4.7.1 Wave structure

We now examine the time-mean structure of the large-scale waves from a perspective of vertical normal modes. Figs. 4.17b and c depict the zonal distributions of $\{u_n\}$ and $\{\phi_n\}$, respectively. The sign convention is chosen such that u_n has the same sense as the horizontal winds at the surface. To aid the interpretation of the spectra, the spatial distribution of $\{u'\}$ appearing in Fig. 4.7a has been replotted in Fig. 4.17a. Taken together, Figs. 4.17a-c suggest that the boomerang-like structure of the waves is a result of the superposition of two pairs of vertical normal modes that are phase shifted with respect to one another: a pair of first internal modes with phase speeds of 35 and 45 m s^{-1} and a pair of third internal modes with phase speeds of 16 and 18 m s^{-1}. These two pairs of modes are hereafter referred to as the "fast" and "slow" modes, respectively.

The dotted and solid curves in Fig. 4.18a depict the zonal distributions of

$$\{u_{fst}\} = \{u_{35} + u_{45}\}/2 \text{ and} \tag{4.23}$$

$$\{u_{slw}\} = \{u_{16} + u_{18}\}/2, \tag{4.24}$$

respectively, where the subscripts on the RHS refer to the phase speed (rather than mode index) of the particular normal mode. Both curves exhibit two wave-like oscillations. The first oscillation occurs between roughly 2,000 and 7,000 km, while the second occurs between about 7,000 and 2,000 km. The amplitude of the first oscillation is more than

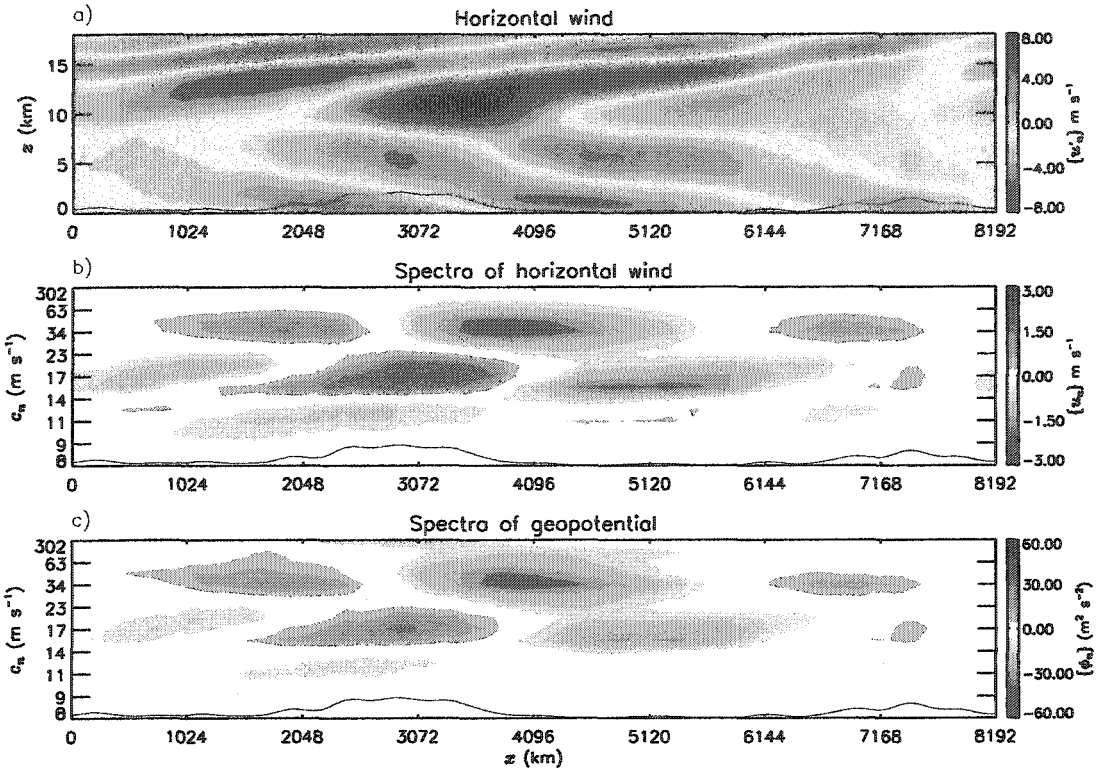

Figure 4.17 Longitude-height cross-sections of $\{u'\}$ (a), $\{u_n\}$ (b) and $\{\phi_n\}$ (c). Solid curves at the bottom of each panel denote $\{P\}^*$ (maximum amplitude of 0.58 mm hr^{-1}).

twice that of the second. The distribution of $\{P_{dc}\}^*$, given by the dot-dashed curve, is more-or-less in phase with $\{u_{slw}\}$, while being in quadrature with $\{u_{fst}\}$. A comparison of Figs. 4.18a and b shows that the horizontal wind anomalies of the fast and slow modes are in phase with their respective geopotential anomalies. We also see that: 1) the slow modes lead the fast modes by roughly 90°, and 2) the amplitudes of the slow and fast modes are comparable to one another.

The above results are consistent with the predictions of the moisture relaxation model in two respects. First, the simulated waves travel at roughly the same speed as the slow modes. Second, the phase shift between the fast and slow modes is close to 90°. Unlike

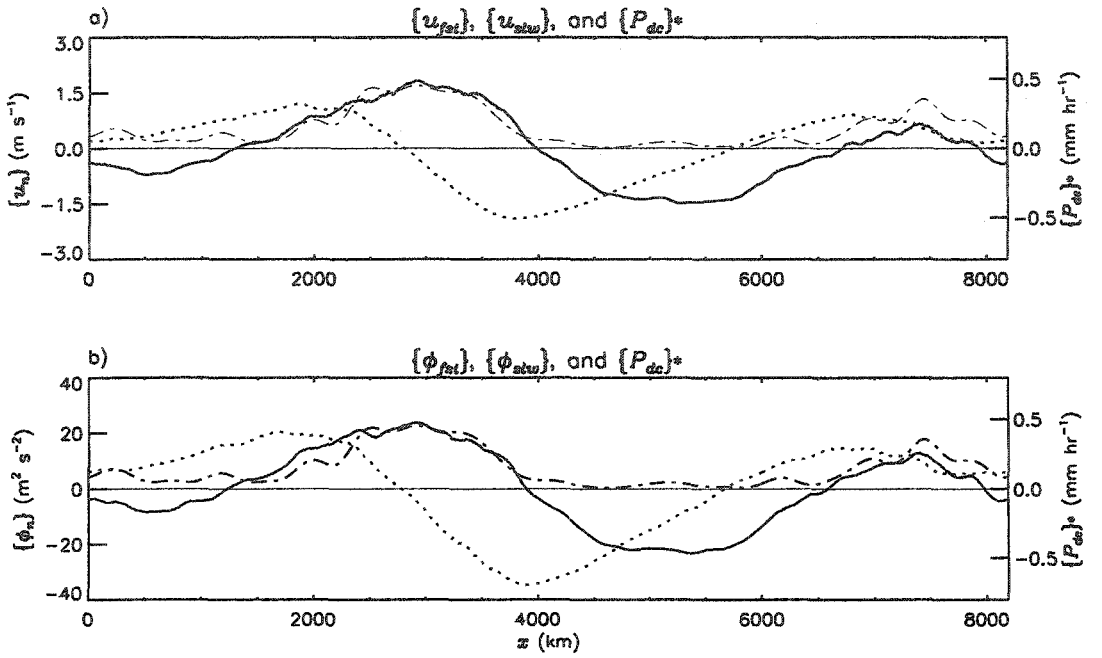

Figure. 4.18 a) Zonal distributions of $\{u_{slw}\}$ (solid), $\{u_{fst}\}$ (dotted), and $\{P_{dc}\}^*$ (dot-dashed). b) Similar to a) but for geopotential anomalies.

the predictions of this model, however, the amplitude ratio of the slow and fast modes in the simulation is close to unity.

4.7.2 Energetics

FS85's theory of the vertical normal mode transform is formulated in the context of the dry meteorological (hydrostatic and compressible) primitive equations. For perturbations about a time-invariant base-state and neglecting the effects of friction and rotation, the physical-space-statement expressing approximate conservation of energy in this system is given by

$$\frac{\partial}{\partial t}\left[\frac{1}{2}u^2+\frac{1}{2\overline{N}_B^2}\left(\frac{gT'}{\overline{T}}\right)^2\right]=-\frac{\partial}{\partial x}u\phi'+\frac{\partial}{\partial p}\omega\phi'+\frac{g[Q_{mic}+Q_{1flx}]}{\overline{T}\overline{N}_B^2}\left(\frac{gT'}{\overline{T}}\right)+uF_{flx}, \qquad (4.25)$$

where ω is the vertical p-velocity and $\overline{N}_B^2$ is the dry Brunt-Vaisala frequency. A comparison of this expression with the (4.19) shows that conservation of energy in the dry, hydrostatic compressible system is very similar to that in the dry, non-hydrostatic anelastic system. The main differences are that here: 1) the derivatives are expressed in p-coordinates, and 2) the kinetic energy does not include the component associated with vertical motion.

The statement expressing conservation of energy in the transformed system can be written as

$$\frac{\partial}{\partial t}\left(\frac{1}{2}u_n^2+\frac{1}{2}\frac{\phi_n^2}{c_n^2}\right)=-\frac{\partial}{\partial x}(u_n\phi_n)+\frac{\phi_n}{c_n^2}\left(\frac{\partial \Phi_n^{mic}}{\partial t}+\frac{\partial \Phi_n^{1\,flx}}{\partial t}\right)+u_nF_n^{flx}, \tag{4.26}$$

where the first and second terms on the LHS are the kinetic energy (KE_n) and available potential energy (APE_n) of the nth mode, respectively, while the second and third terms on the RHS represent the eddy generation of APE_n ($EAPE_n$) and KE_n (EKE_n), respectively. Since the vertical normal modes are orthonormal in the inner product, the energetics of the transformed system is related to the that of the stratified system (i.e., 4.26) by the following set of expressions:

$$\sum_{n=0}^{\infty}KE_n=\frac{1}{p_B-p_T}\int_{p_T}^{p_S}KE_u dp, \tag{4.27}$$

$$\sum_{n=0}^{\infty}APE_n=\frac{1}{p_B-p_T}\int_{p_T}^{p_S}\frac{1}{2\overline{N}_B^2}\left(\frac{gT'}{\overline{T}}\right)dp=\frac{1}{p_B-p_T}\int_{p_T}^{p_S}APE_D dp, \tag{4.28}$$

$$\sum_{n=0}^{\infty}(EAPE_n^{mic}+EAPE_n^{flx})=\frac{1}{p_B-p_T}\int_{p_T}^{p_S}\frac{g[Q_{mic}+Q_{1\,flx}]}{\overline{T}\overline{N}_B^2}\left(\frac{gT'}{\overline{T}}\right)dp, \text{ and} \tag{4.29}$$

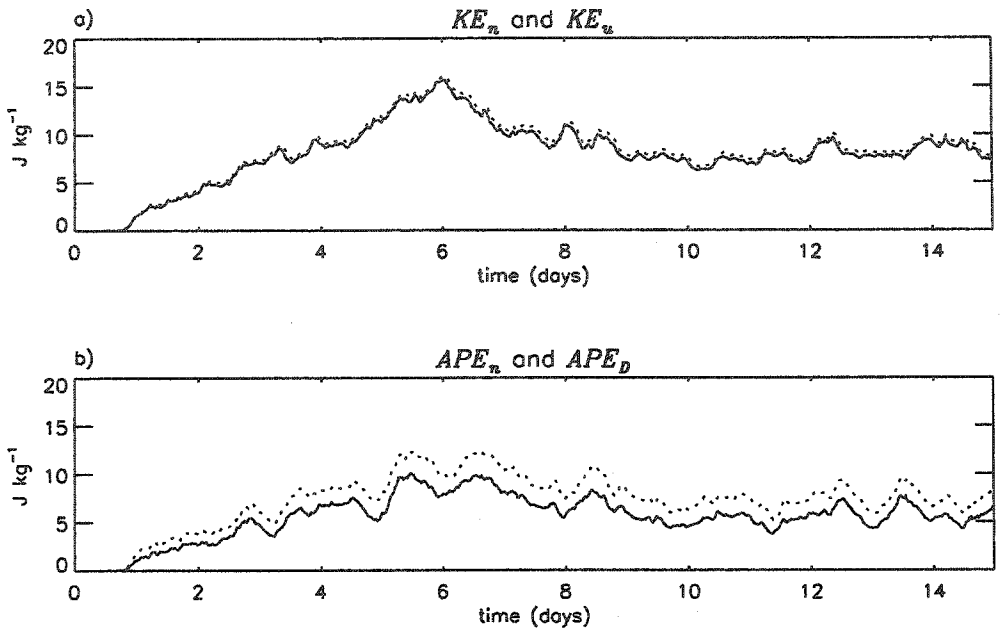

Figure 4.19 a) Domain-averaged evolution of KE_n (summed over the $N = 64$ modes; solid) and KE_u (dotted). b) Similar to a) but for APE_n (solid) and APE_D (dotted).

$$\sum_{n=0}^{\infty} EKE_n^{flx} = \frac{1}{p_B - p_T} \int_{p_T}^{p_S} uF_{flx} dp . \tag{4.30}$$

Fig. 4.19a shows that the domain-averaged evolution of $\sum KE_n$ and KE_u are virtually identical but with the former systematically about 5% smaller than latter. This systematic offset is most likely due to errors associated with the spectral truncation. A comparison of the dotted and solid curves in Fig. 4.19b, on the other hand, shows that $\sum APE_n$ is systematically about 25% smaller than the RHS of (4.29). The larger discrepancy in this case is most likely explained by the fact that the dry version of the hydrostatic approximation, i.e.,

$$-\frac{\partial}{\partial z} p' = \bar{\rho} g \frac{T'}{\bar{T}}, \tag{4.31}$$

is not always well satisfied in the simulation. This is perhaps most true in the lower troposphere, where moisture anomalies have a relatively large impact on density.

4.7.2.1 Energy production

The curves appearing in Fig. 4.20a depict the domain- and time-averaged spectra of $EAPE_n^{mic}$ in deep convective (solid), stratiform (dotted), and mid-level convective regions (dashed) of the simulation. The deep convective spectrum shows relatively strong production of energy in both the slow and fast modes and weak destruction of the 23 m s^{-1} mode. The stratiform spectrum also shows strong energy production in the slow modes, but with additional production in modes with phase speeds of c_n = 20 and 23 m s^{-1}. Owing to the shape of the heating profile, however, stratiform heating generates very little energy in the deep modes. The averaged spectrum of $EAPE_n^{mic}$ in mid-level convective regions is remarkably similar to that in stratiform regions but with the sign of the spectrum reversed. Thus, while deep convective and stratiform latent heating processes *both* generate energy in the slow modes, mid-level convective processes tend to destroy it.

The dotted line in Fig. 4.20d depicts the averaged spectrum of $EAPE_n^{flx}$ in all convective regions of the simulation. The spectrum exhibits a relatively strong sink of energy in the 16 m s^{-1} mode and a strong source in the 20 and 23 m s^{-1} modes. In Fig. 4.20b, we see that deep convective and mid-level convective transport processes both play an important role in producing the sink at 16 m s^{-1}. The strong source at 20 and 23 m s^{-1}, on the other hand, is mainly due to deep convective transports and can be explained by the fact that the profile of Q_{1flx} in deep convective regions is typically stratiform-like in appearance.

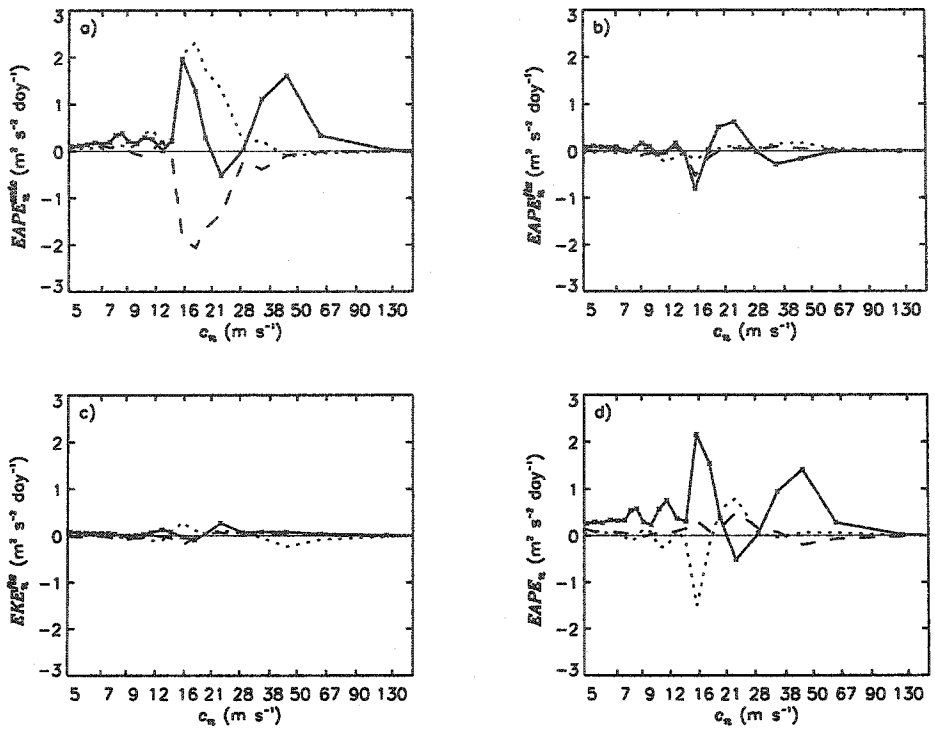

Figure 4.20 Domain- and time-averaged spectra of $EAPE_n^{mic}$ (a), $EAPE_n^{flx}$ (b), and EKE_n^{flx} (c) in deep convective (solid), stratiform (dotted), and mid-level convective regions (dashed) of the simulation. d) Sum of curves appearing in a) (solid), b) (dotted), and c) (dashed).

A comparison of the solid and dashed curves in Fig. 4.20d shows that the sources and sinks of energy due to EKE_n^{flx} (averaged over all convective regions) are generally much smaller than those due to $EAPE_n^{mic}$. The one exception occurs at 23 m s^{-1}, where the spectrum of EKE_n^{flx} is positive and thus, tends to offset the destruction of energy by latent heating in deep convective regions. In Fig. 4.20c, we see that convective momentum transports in deep convective regions are primarily responsible for this offset.

Fig. 4.21 compares the domain- and time-averaged energy spectrum (E_n = KE_n + APE_n), given by the solid curve, with that of the net energy production spectrum (EP_n =

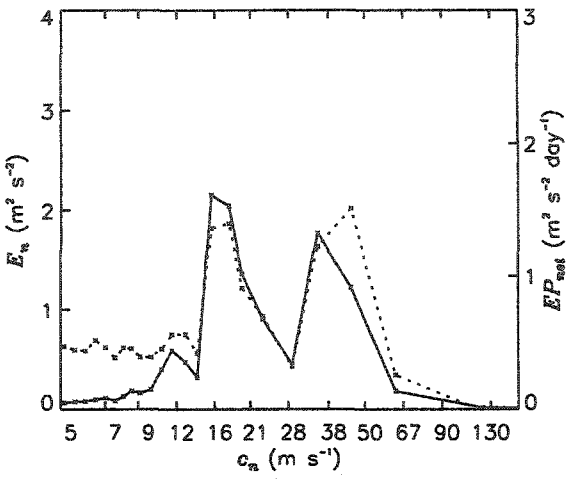

Figure 4.21 Domain- and time-averaged spectra of E_n (solid) and EP_{net} (dotted).

$EAPE_n^{mic} + EAPE_n^{flx} + EKE_n^{flx}$), given by the dotted curve. For steady-state conditions and assuming the effects of dissipation can be represented by simple Newtonian damping (independent of *n)*, one expects the shapes of the two spectra to be similar to one another. This is what Fig. 4.21 shows although the agreement is not perfect. Presumably, some of the discrepancy is due to higher-order modes being more efficiently damped than lower-order modes. The explanation for the over-prediction of energy production in the 45 m s^{-1} mode, however, is not clear.

4.7.2.2 Distribution of energy production

The distribution of $\{EAPE_n^{mic}\}$ can be written as

$$\{EAPE_n^{mic}\} = \left\{\frac{\phi_n}{c_n^2}\right\}\left\{\frac{\partial \Phi_n^{mic}}{\partial t}\right\} + \left\{\frac{\phi_n''}{c_n^2}\frac{\partial}{\partial t}\Phi_n^{mic_{\eta\eta}}\right\}, \qquad (4.32)$$

where double-primed quantities denote departures about the time-average. The first and second terms on the RHS of (4.32) represent the "stationary" and "transient" components of $\{EAPE_n^{mic}\}$, respectively.

The solid and dotted curves in Figs. 4.22a depict the low-pass filtered distributions of the stationary component of $\{EAPE_{fst}^{mic}\}$ and $\{EAPE_{slw}^{mic}\}$, respectively. While the latter shows production across both envelopes, the former shows destruction (production) towards the rear (front) of Envelope S and destruction across Envelope W. On the basis of these distributions alone, one should expect the energy of the slow modes to be considerably larger than that of the fast modes. In Fig. 4.22b, however, we see that the transient components of $\{EAPE_{fst}^{mic}\}$ and $\{EAPE_{slw}^{mic}\}$ both represent strong sources of energy. As a result, the vast majority of the destruction in the deep mode by the stationary component is offset by the transient component (Fig. 4.22c).

The above results provide a possible explanation for why the moisture relaxation model fails to predict the correct amplitude ratio of the fast and slow modes. Referring back to Fig. 3.7c, we see that, in the moisture relaxation model, the production of energy in the slow mode is considerably larger than that of the fast mode, primarily because moisture anomalies of the fast mode promote a convective heating field that is *out of phase* with its thickness field and thus, destruction of APE (i.e., $PEG_{11} < 0$). This prediction is consistent with Fig 4.22a which shows destruction of energy in the fast mode towards the rears of both Envelope S and Envelope W, i.e., in the "cold" phase of the fast modes. The strong production of energy in the deep mode towards the front of Envelope S is also consistent with the energetics of the moisture relaxation model. Fig. 3.7c shows that the destruction

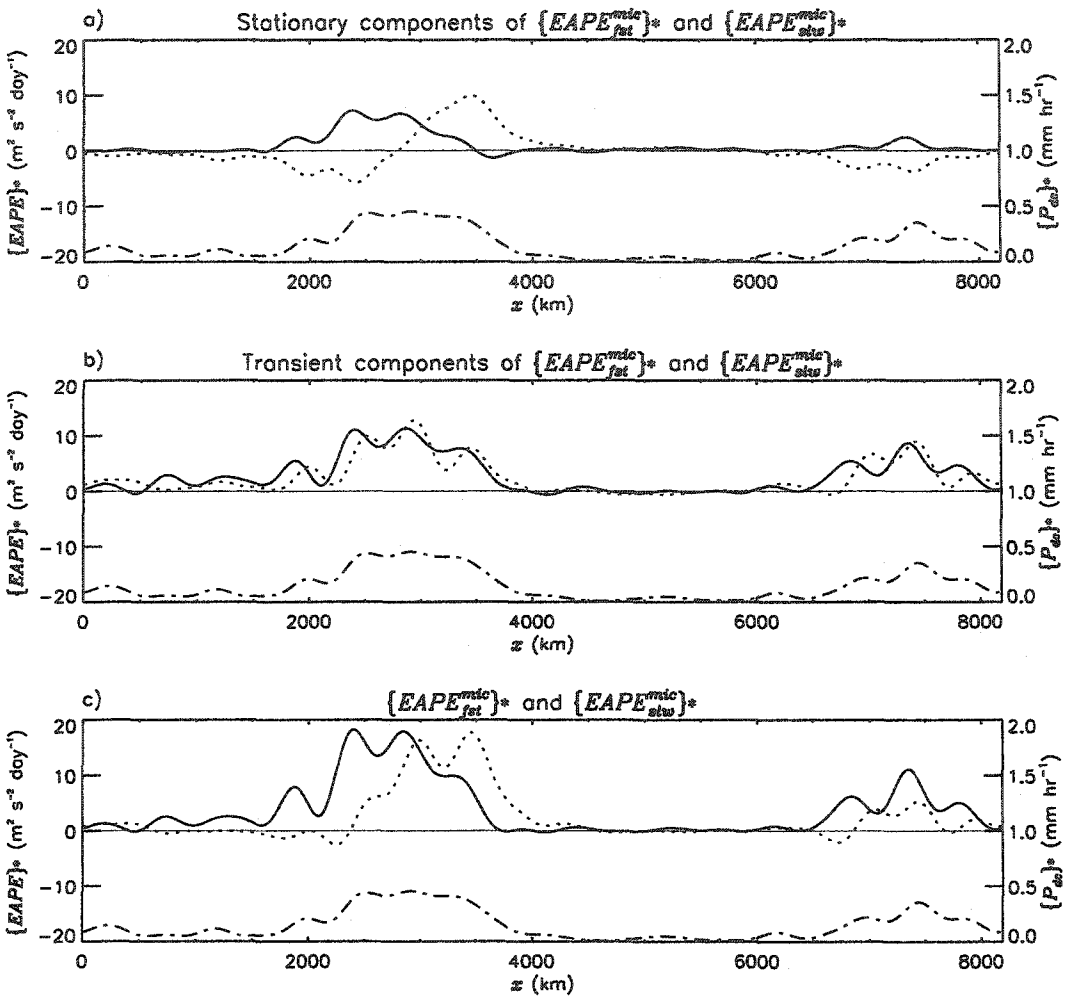

Fig. 4.22 Low-pass filtered distributions of the stationary (a), transient (b), and total component (c) of $\{EAPE^{mic}_{fst}\}$ (dotted) and $\{EAPE^{mic}_{slw}\}$ (solid).

of energy due to PEG_{11} is offset by PEG_{21}, i.e., moisture anomalies of the slow mode being in phase with the geopotential anomalies of fast mode. This prediction is consistent with the stationary energetics of Convective Envelope S.

In conclusion, it appears that the moisture relaxation model fails to predict the correct amplitude ratio of the fast and slow modes because it does not account for the source of energy due to transients.

4.8 Transient structure of the large-scale waves

The previous two sections focused on the time-mean structure and energetics of the convectively coupled gravity waves. In this section, the discussion shifts towards their transient structure, the importance of which has just been illustrated.

4.8.1 Methodology

The transient structure of the waves is analyzed by constructing composited Hovmoller diagrams of model output. The composited diagrams illustrate the averaged space-time evolution of the simulated atmosphere with respect to a set of 600 "discrete convective events" (DCE). The DCEs are identified using an iterative procedure consisting of the following three steps:

Step 1: Search through the simulation to find the most strongly precipitating deep convective core grid-point.

Step 2: Mask the DCE as the core grid point and also the contiguous region of grid points with non-zero P that are connected (either in time or in space) to this grid point.

Step 3: Repeat step 3 to find the next DCE.

The iterative procedure stops when all DCEs with core grid points characterized by $P > 25$ mm hr^{-1} have been identified. Each model field is then composited (both in time and space) with respect to the DCE's "center", i.e., with respect to its deep convective core grid-point.

4.8.2 Results

Figs. 4.23a-d show the resulting composited Hovmoller diagrams of P, PW, CAPE, CIN, and E_b, respectively. When examining these diagrams, the reader should note the fol-

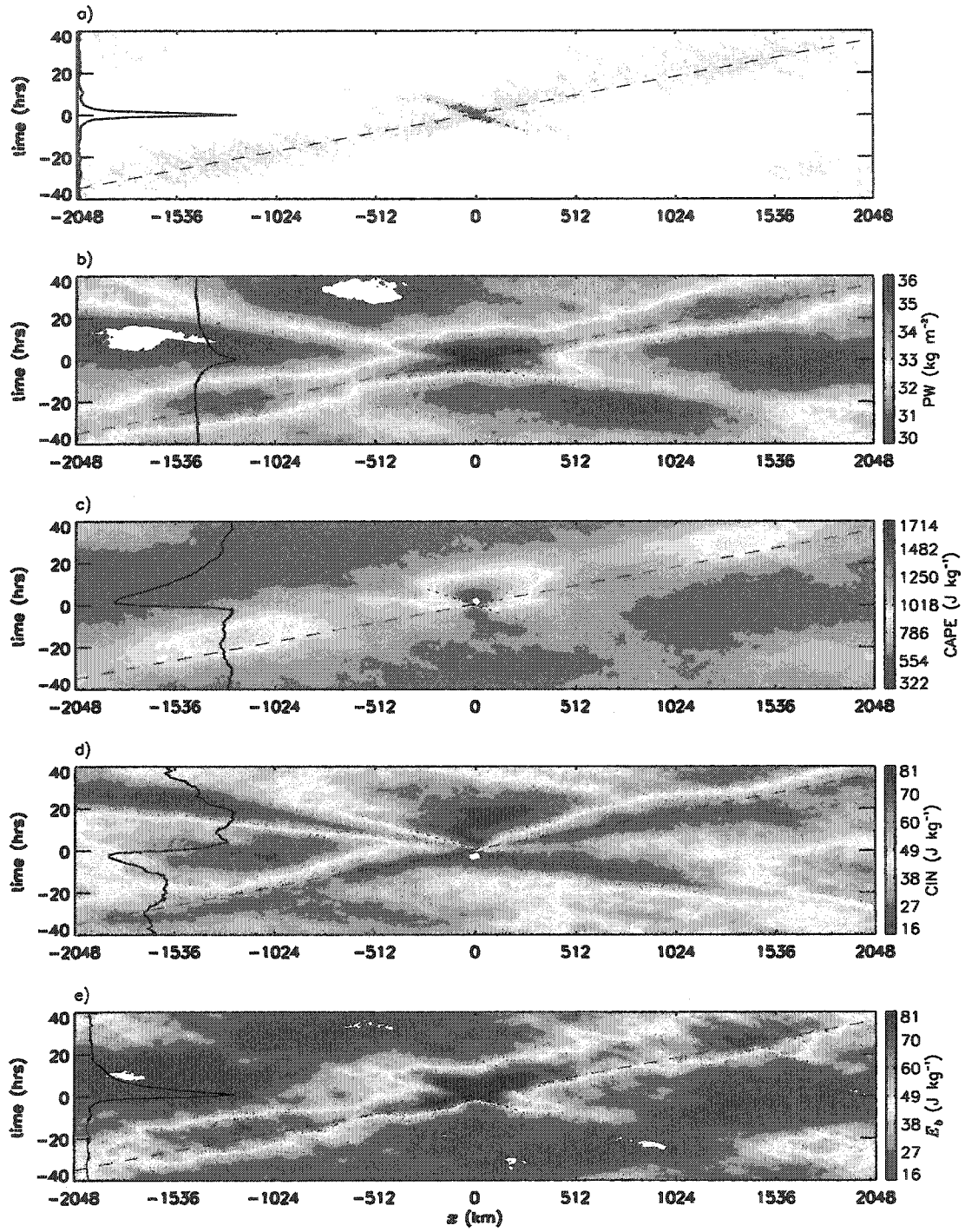

Figure 4.23 Hovmoller diagrams of P (a), PW (b), CAPE (c), CIN (d) and E_b (e) composited with respect to 600 DCEs. Solid line running up the left hand side of each diagram depicts the evolution of respective field averaged between -25 and 25 km. Dashed and dotted lines denote phase speeds of16 and 9 m s^{-1}, respectively. In b)-e), values below that of the color-bar have been left unshaded. Shading increments in a) are 1, 2, and 20 mm hr^{-1}.

lowing. The center of each diagram coincides with center of the DCE. The thick solid contour running up the left-hand side of each diagram (also plotted in Fig. 4.24) depicts the evolution of the respective field averaged within the central 50 km of the domain. The dashed and dotted lines denote phase speeds of 16 and -9 m s^{-1}, respectively.

The space-time evolution of P shows that, on average, DCEs tend to develop within mesoscale (~ 100 km) convective systems (MCSs) travelling westward at an average speed of about 9 m s^{-1} and which are embedded in the wave's larger-scale eastward moving convective envelope. The implied average lifetime of the MCSs is about 8 hrs, while that of the DCE's core is about 1 hr. The large-scale convective envelope travels at a speed of 16 m s^{-1} and, upon close inspection, appears to undergo a temporal modulation of roughly 20 hrs.

The near-field evolution of the simulated atmosphere following the DCE's development is generally as one might expect. Spreading in either direction from the center of the domain at a speed of about 9 m s^{-1}, there is a convective outflow region where CIN and E_{tr} are both anomalously high while CAPE is anomalously low. Values of PW, on the other hand, show relatively strong locally moistening. This moistening likely due to convective detrainment and perhaps also due to enhanced lifting by gravity waves. Interestingly, while values of CAPE, PW, and E_{tr} recover to their background values in about 20 hrs, the recovery of CIN takes more than twice as long.

Prior to the DCE's development and within the central 50 km of the domain, we see that CIN decreases steadily for about 7 hrs and reaches a minimum 3 hrs before the onset of convection. Values of E_b, on the other hand, remain fairly constant up to t = -3 hrs and then increase rapidly towards a peak at t = + 1 hr. GIven that E_b does not exceed CIN until

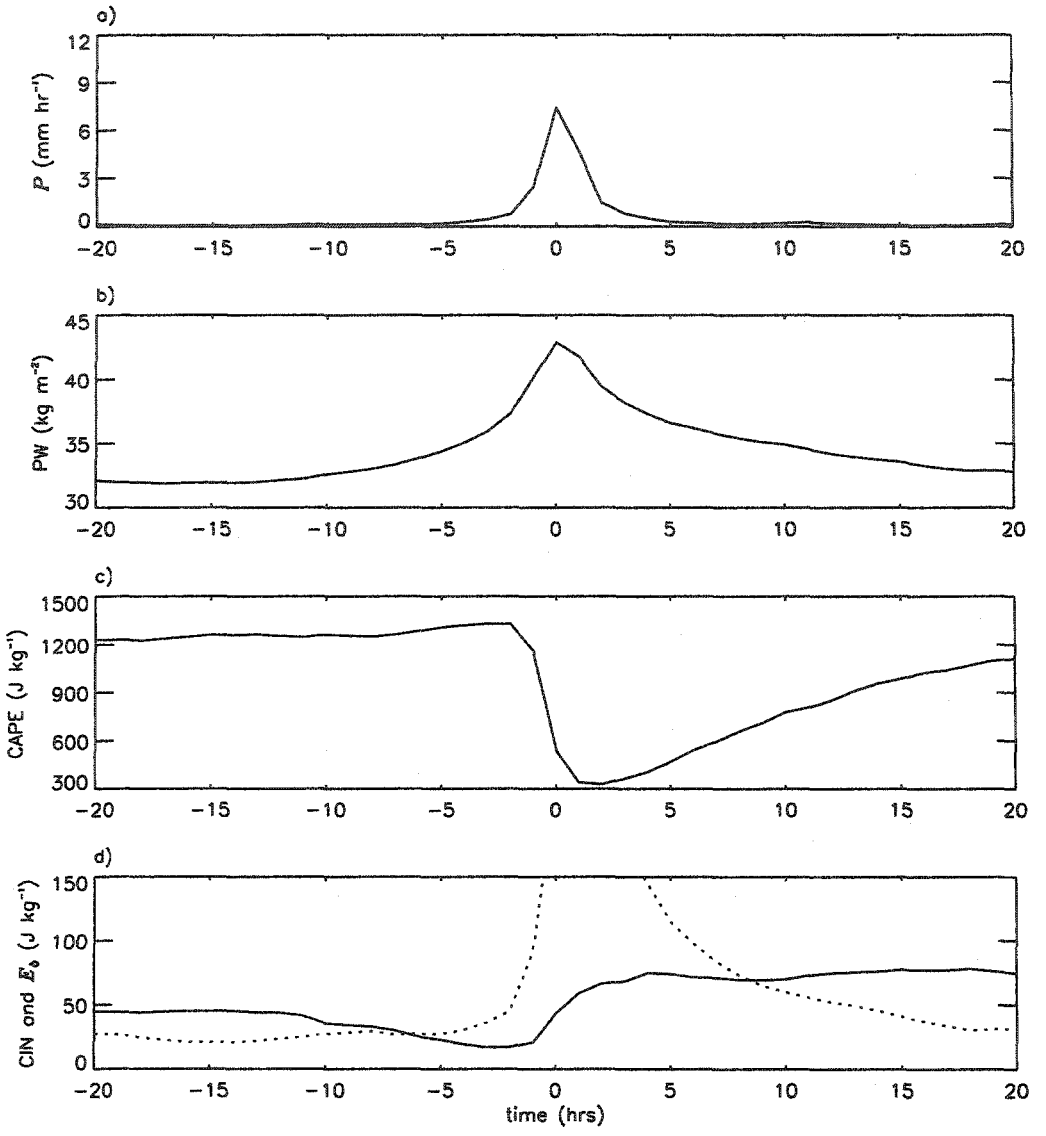

Figure 24. Evolution of P (a), PW (b), CAPE (c), CIN (d; solid), and E_b (d; dotted) averaged within the central 50 km of the composited Hovmoller diagrams appearing in Fig. 23.

t = -5 hrs (Fig. 4.24d), while CAPE is abundant *and* is slowly increasing, suggests that convection may indeed be inhibited prior to this time. Why then doesn't deep convection "fire" at t = -5 hrs? Perhaps, the atmosphere must first undergo a period of moistening in order to allow undilute ascent to the tropopause. The steady increase in PW and P during the six hours leading up to deep convection provides some evidence to support this idea.

Fig. 4.25 is similar to Fig. 4.23 but showing the composited evolution of E_n in the 45 (a), 35 (b), 21 (c), 18 (d) and 16 m s^{-1} (e) modes, respectively. Consistent with Fig. 4.18, we see that the large-scale convective envelope can be regarded as an eastward moving packet of energy in both the 16 and 18 modes. As the eastward moving packets of energy pass though the DCE, we see that both their width and intensity increases suggesting that they are energetically reinforced by convection. At the same time, we also see a more narrow (~200 km) packet of energy (primarily in the 18 m s^{-1} mode) propagating westward from the DCE's center at a speed of roughly 16-18 m s^{-1}. In Fig. 4.23, this narrow westward moving packet, as well as the broader eastward moving packet, appear as a region where CIN is reduced from its background value, while *PW* is enhanced, both of which are favorable for convective development.

In addition to the arrival of relatively intense and broad eastward moving packets of energy in the 16 and 18 m s^{-1} modes, Fig. 4.24c shows that the onset of deep convection also coincides with the arrival of relatively narrow and weak packets of energy (both westward and eastward propagating) in the 21 m s^{-1} mode. The passage of the westward moving packet is clearly evident in Fig. 4.23 as a region where CIN is reduced from its background value, while *PW* is enhanced. Presumably, the low-level moistening associated with the passage of this mode serves to enhance the intensity of the DCE, and perhaps also, promotes its development.

The DCE also acts to excite mesoscale packets of energy in the deep modes. These packets propagate in either direction from the center of the domain at speeds in the range

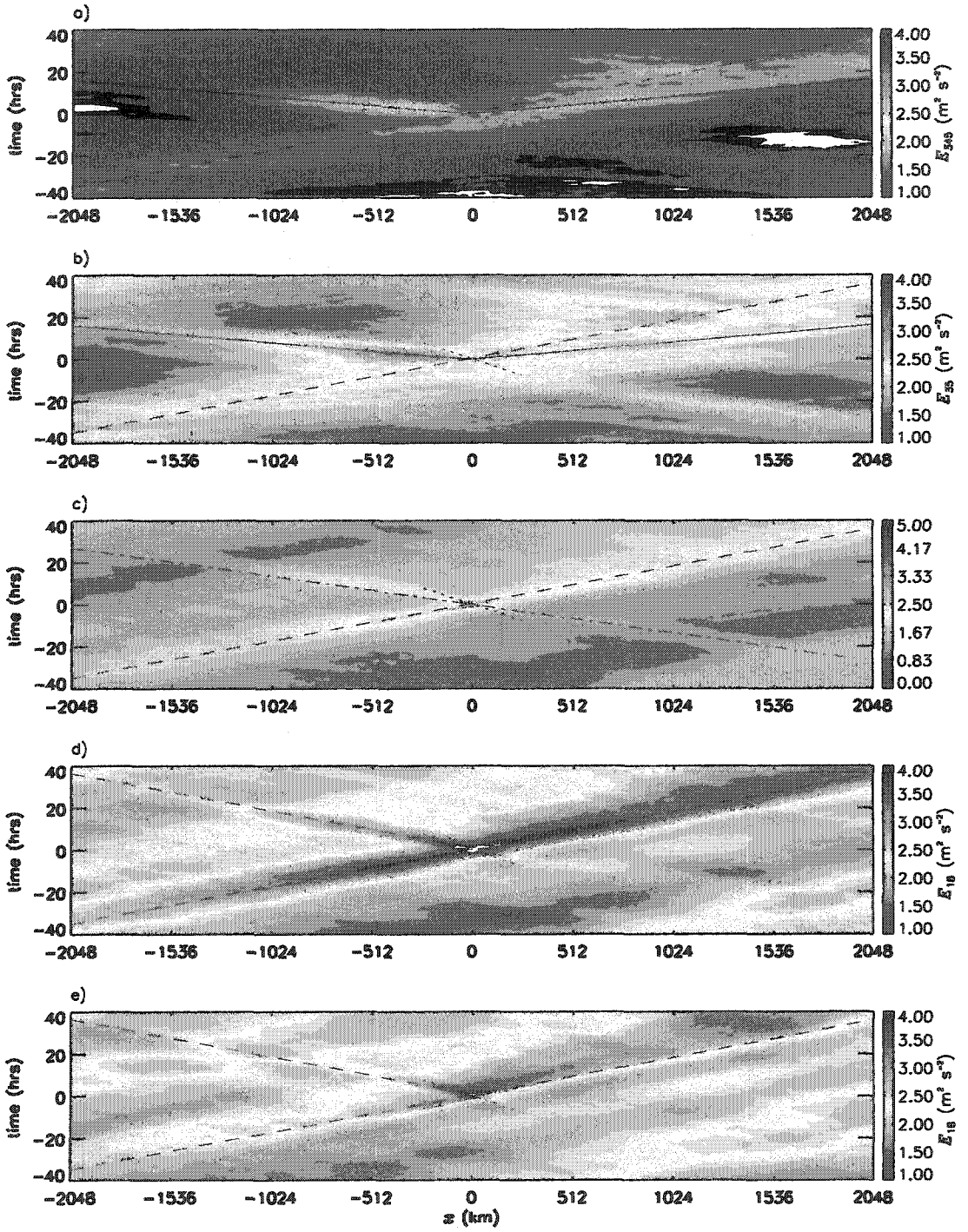

Figure 4.25 Similar to Fig. 4.23 but showing E_n in the 45 (a), 35 (b), 21 (c), 18 (d) and 16 m s^{-1} (e) modes.

35-45 m s^{-1} and appear as regions where *PW* and CAPE are both reduced from their background values, while CIN is enhanced.

Results from the linear analysis of Chapter 2 showed that gravity wave packets excited by and moving in the same direction as a travelling heat source tend to be narrow and intense, while those moving the opposite direction tend to be more broad and weak. The composite evolution of energy in the both the slow and fast modes is broadly consistent with this theoretical prediction. For example, Figs. 4.24a and b show that the amplitude of the westward moving packets of energy in 45 and 35 m s^{-1} modes are each substantially more intense than their eastward moving counterparts.

4.9 Summary and discussion

This chapter discussed an in-depth analysis of the structure and energetics of large-scale convectively coupled gravity waves simulated using a 2D CRM. The structure and energetics of the waves was examined both in physical space and in spectral space. A primary goal of the chapter was to assess existing theories of coupled wave instability, including the ones developed in Chapter 3. A summary and discussion of the important findings of this study are discussed below.

As with Grabowski and Moncrieff (2001), the structure and phase speed of the simulated waves was found to compare favorably with observed convectively coupled Kelvin waves in the equatorial wave guide. Adding to their results, here it was shown that the boomerang-like structure of the waves is primarily due to the superposition of two pairs of vertical normal modes that are phase shifted with respect to one another: a pair of first internal modes with phase speeds of 45 and 35 m s^{-1} and a pair of third internal modes with

phase speeds of 16 and 18 m s^{-1}. Consistent with the predictions of the moisture relaxation model developed in Chapter 3, the large-scale waves were found to propagate at a speed close to that of the slow modes, and the phase shift between the fast and slow modes is about 90°. Unlike the predictions of this model, however, the amplitude ratio of the slow and fast modes was found to be close to unity. This discrepancy is possibly explained by the fact that transient perturbations (with respect to the time-mean averaged flow in the wave's moving frame of reference) generate a substantial amount of energy in the deep mode and, thereby, act to offset the destruction of energy due to the waves' time-averaged heating and circulation patterns.

The deep convection associated with the simulated waves was found to lag the column-integrated moisture convergence by about 300 km, while leading fluctuations in PW by about 50-100 km. Although this result supports the simple approach taken in the moisture relaxation model, the existence of a lag of PW with respect to deep convection suggests that fluctuations in the former may be caused by (rather than controlling) the latter. In any event, a convective parameterization based on moisture relaxation is unsatisfactory, since it does not directly relate the intensity of convection to the buoyancy of clouds (the quantity that actually controls the intensity of convection).

The stratiform instability model of Mapes (2000) provides an alternative explanation for the spontaneous development of large-scale convectively coupled gravity waves in the simulation. Here, the phase relationships between deep convection, CAPE, and CIN in the simulated waves were found to be qualitatively consistent with the predictions of his model. In order to make further assessments of Mapes' theory, the quantity E_b (i.e., the sum of the averaged KE and APE in the boundary layer) was introduced as a measure of

the energy available for overcoming CIN and hence, triggering convection. A surprising result was that E_b is indeed lower (higher) than CIN in the suppressed (convectively active) phases of the large-scale waves. While this result is consistent with Mapes' theory, a direct test of his convective parameterization showed only marginal agreement with the simulated distribution of precipitation. A possible explanation for the discrepancy is that Mapes' convective parameterization does not account for the effects of moisture on convective development.

Results from Chapters 2 and 3 suggested that deep convective heating processes, as well as stratiform heating processes, might play an important role in maintaining the energy of higher-order normal modes associated with large-scale convectively coupled gravity waves. An analysis of the simulation confirmed this idea. Results showed that deep convection heating processes contribute roughly 40% of the total energy production in the slow modes, while stratiform heating processes contribute the remaining 60%. Surprisingly, mid-level convective heating processes were found to destroy roughly the same amount of energy in the slow modes as that generated by stratiform heating processes.

The stratiform model of Mapes (2000) accounts for the destruction of energy in the slow modes by mid-level convective heating processes. On the other hand, this model, as well as the stratiform instability model of Majda and Schefter (2001), does not account for the generation of energy in the slow modes by deep convective heating processes. Presumably, this approximation leads to errors both in the predicted growth rates and structure of unstable waves in their models.

In summary, none of the theories of coupled wave instability assessed herein successfully captures all aspects of the simulation. Nevertheless, the marginal successes of the

moisture relaxation model and the stratiform instability model of Mapes (2001) provide a conceptual basis for further exploring the roles of moisture and CIN in the regulation of tropical deep convection. It also seems safe to conclude that the relatively slow phase speed of the simulated large-scale waves is primarily due to an unstable interaction between convection and higher-order vertical normal modes, rather than to the waves feeling the effects of a reduced static stability.

CHAPTER 5

IMPORTANT FINDINGS AND SUGGESTIONS FOR FUTURE RESEARCH

A fundamental problem in meteorology is the interaction between tropical convection and large-scale waves. This problem has received renewed interest in recent years with the observational work of Takayabu (1994), Wheeler and Kiladis (2000), Wheeler et al. (2001), and Straub and Kiladis (2002). These studies clearly demonstrate the existence of convectively coupled equatorial waves, i.e., zonally propagating synoptic-scale cloud disturbances with the dispersion characteristics of shallow water equatorial waves. Among the various types of waves identified, convectively coupled Kelvin waves are found to be the most prominent, explaining roughly the same amount of convective variance as the MJO. These waves are arguably the simplest type of convectively coupled wave, since they essentially behave as a two-dimensional eastward propagating gravity wave.

With a view towards improving our understanding of convectively coupled Kelvin waves, this study investigated the interaction between tropical convection and atmospheric gravity waves in an idealized (2D and non-rotating) framework. The problem was studied both analytically, in the context of linear hydrostatic theory, and explicitly, via forward time integration of a non-linear and non-hydrostatic CRM. The vertical normal mode

transform was used to aide the development of simple models and also to help interpret output from direct numerical simulations. A primary goal of this study was to assess the predictions of the simple models using output from the simulations.

The important new findings of this research are listed and discussed below. Suggestions for future research are made thereafter.

5.1 What's new?

1) Large-scale convectively coupled gravity waves represent a mode of tropical convective self-organization.

A fundamental question of tropical meteorology is whether convectively coupled Kelvin waves represent a mode of tropical convective self-organization, i.e., whether they can spontaneously develop in the absence of a mean flow, under uniform large-scale forcing and uniform lower boundary conditions. On the basis of their statistical equilibrium view of convection, Emanuel et al. (1994) argue that convection acts to rapidly respond to temperature variations across the depth of the free troposphere and, thereby, tends to damp all pre-existing disturbances. Self-organization is then only possible if the convection is embedded in a mean flow. The unstable waves, in this case, are characterized by a deep (first internal mode) structure in the troposphere and, owing to the effects of a reduced static stability, propagate at speeds considerably slower than that of the first internal mode.

Mapes (2000) later argues that this view is oversimplified. With a convective closure in which convection amount is primarily controlled by CIN, he shows that large-scale convectively coupled gravity waves can spontaneously develop from random initial conditions, even in the absence of a mean flow. An important assumption in his model is that stratiform heating processes lag deep convective heating by a relatively short (3 hr) time

scale. He argues that this assumption selects the preferred scale of the unstable waves. The unstable waves propagate at a speed set by that of the second internal mode, and they exhibit a boomerang-like structure with the elbow of the boomerang located in upper-troposphere. Although the physical explanations are different, the moisture relaxation model developed in Chapter 3, as well as the phase-lagged wave-CISK model of Davies (1979) and the stratiform instability models Majda and Schefter (2001), make predictions similar to those of Mapes' (2000) model.

Extending the work of Grabowski and Moncrieff (2001), this study used a 2D CRM to conduct a 15 day simulation of radiative convective equilibrium in large-scale periodic domain extending 8192 km in the horizontal and with a uniform SST of 300 K. To eliminate possible interactions between convection and a mean flow, the horizontal winds were uniformly relaxed to zero on a four hour time scale. The results of this simulation showed the spontaneous development of two large-scale convectively coupled gravity waves. As with Grabowski and Moncrieff (2001), both the phase speed and vertical structures of the dynamical fields associated with the waves were found to strongly resemble observations of convectively coupled waves. Adding to their results, here it was shown that the boomerang-like structure of the large-scale waves is primarily due to the superposition of two pairs of vertical normal modes that are phase shifted with respect to one another: a pair of first internal modes with phase speeds of 45 and 35 m s^{-1} and a pair of third internal modes with phase speeds of 16 and 18 m s^{-1}. The large-scale waves propagate at a speed close to that of the slow modes and the low-level convergence field of the slow modes leads that of the fast modes by roughly 90° . The deep convection associated with the waves is in phase

with the convergence field of the fast modes and thus, lags the low-level convergence field of the slow modes by 90°.

2) Transient deep convection tends to create a region around itself where conditions are favorable for further convective development.

A long-standing view among meteorologists is that a deep convective heat source primarily excites a first internal mode and that the passage of this mode causes adiabatic warming and drying. In this way, the source creates a region around itself where conditions are hostile towards future convective development. Mapes (1993) later showed that a spatially localized heat source with a top-heavy heating profile, like that of observed tropical MCSs, tends to strongly excite a second internal mode response and that the passage of this mode causes low-level cooling and moistening. He therefore suggested that tropical MCSs should be gregarious.

In the first half of Chapter 2, this study investigated the linear response of two-dimensional atmosphere to a prescribed deep convective heat pulse, extending the earlier theoretical work of Nicholls et al. (1991), Pandya et al. (1993), and Mapes (1993). Results showed that the source strongly excites an 16 or 20 m s^{-1} mode, depending on the depth of the heating, and that the passage of this mode causes a reduction in CIN and an increase in both the moisture content of the free troposphere and CAPE. This provides further evidence that an isolated deep convective cloud tends to create a region around itself where conditions are favorable for future convective development. Here, it was shown that the size of this region depends on the duration of the heating as well as its speed of translation. It was also found that this region does not emerge until *after* the heating is switched off.

3) Deep convection generates large amounts of energy in higher-order normal modes

The stratiform instability models of Mapes (2000) and Majda and Schefter (2001) are both based on the implicit assumption that deep convection does not excite energy in the second internal mode, i.e., the so-called stratiform mode. This assumption is only strictly correct, however, when a rigid lid is placed at the top of the convectively heated layer such that the vertical propagation of gravity wave energy is eliminated. When the rigid lid is placed at a higher level, it was shown here that an isolated deep convective heat source actually tends to rather strongly excite a second or third internal mode, depending on the depth of the heating. It was therefore hypothesized that deep convective heating processes, as well as stratiform heating processes, play an important role in maintaining the energy of higher-order normal modes associated with large-scale convectively coupled gravity waves.

The analysis of the CRM simulation discussed in Chapter 4 confirmed this hypothesis. Results showed that deep convective heating processes contribute roughly 40% of the total energy production in the "slow" modes, while stratiform heating processes contribute the remaining 60%. Consistent with the ideas of Mapes (2000), it was found that mid-level convective heating processes act to strongly remove energy from the slow modes.

4) A simple model of convectively coupled gravity waves

It is generally accepted that, owing to the effects of dry air entrainment, moisture fluctuations in the free troposphere have a strong impact on the buoyancy of air inside clouds, and thus, on the development of cumulus convection. Fluctuations in the moisture content

of the boundary layer also have a strong impact on the intensity of convection owing to their impact on CAPE.

Goswami and Rao (1994) and Fuchs and Raymond (2002) both develop simple tropical wave models, in which the intensity of convection is either completely or partially related to the moisture content of the troposphere (in contrast to wave-CISK models, in which the intensity of convection is related to moisture convergence). To simplify their analyses, both sets of authors truncate vertical structure at only the first internal mode. Similar to the theory of Emanuel et al. (1994), both models predict that large-scale convectively coupled gravity waves cannot amplify in the absence of a mean flow.

In Chapter 3, this study developed an inviscid, 2D tropical wave model in which: 1) deep convective heating anomalies are directly related to column-integrated water vapor anomalies and 2) vertical structure is truncated to include two vertical normal modes: a deep (fast moving) mode and a shallow (slow moving) mode. This model, referred to as the moisture relaxation model, predicted that convectively coupled gravity waves should tend to spontaneously develop from random initial conditions, even in the absence of a mean flow. The unstable waves, referred to MI-modes, were found to propagate at speeds close to that of the slower moving vertical normal mode and to exhibit a westward tilt with height in the troposphere. Similar to the predictions of classical wave-CISK models, the largest growth rates were found to occur at the smallest scales. The degree of the "ultraviolet catastrophe", however, was found to be not as severe in this case, however, and was shown to be completely eliminated when the effects of a delay between stratiform and deep convective processes were included.

on the assumed depth of the atmosphere and also on the vertical spectral truncation of the model? Can *large-scale* convectively coupled gravity waves spontaneously develop from random initial conditions, even in the absence of stratiform precipitation processes or a mean flow?

References

Crum, F. X. and D. E. Stevens, 1983: A comparison of two cumulus parameterization schemes in a linear model of wave-CISK. *J. Atmos. Sci.*, **40**, 2671-2688.

Chang, C.-P. and H. Lim, 1988: Kelvin wave-CISK: A possible mechanism for the 30-50 day oscillations. *J. Atmos. Sci.*, **45**, 1709-1720.

Davies, H. C., 1979: Phase-lagged wave-CISK. *Q. J. R. Meteorol. Soc.*, **105**, 325-353.

Demott, C. and S. A. Rutledge, 1998: The vertical structure of TOGA-COARE convection, Part 1: Radar echo distributions. *J. Atmos. Sci.*, **55**, 2730-2747.

Emanuel K. A., J. D. Neelin, and C. S. Bretherton, 1994: On large-scale circulations in convective atmospheres. *Q. J. R. Meteorol. Soc.*, **120**, 1111-1143.

Fuchs, Z. and D. A. Raymond, 2002: Large-scale modes of a nonrotating atmosphere with water vapor and cloud-radiation feedbacks. *J. Atmos. Sci.*, **59**, 1669-1679.

Fulton, S. R. and W.H. Schubert, 1985: Vertical normal mode transforms: Theory and application. *Mon Wea. Rev.*, **113**, 647-658.

Goswami, P. and R. K. Rao, 1994: A dynamical mechanism for selective excitation of the Kelvin mode at timescale of 30-50 days. *J. Atmos. Sci.*, **51**, 2769-2778.

Grabowski, W. W. and M. W. Moncrief, 2001: Large-scale organization of tropical deep convection in two-dimensional explicit numerical simulations. *Q. J. R. Meteorol. Soc.*, **127**, 445-468.

Grabowski, W. W., 2003: MJO-like coherent structures: Sensitivity simulations using the cloud-resolving convection parameterization (CRCP). *J. Atmos. Sci.*, **60**, 847-864.

Haertel, P. T. and R. H. Johnson, 1998: Two-day disturbances in the equatorial western Pacific. *Quart. J. R. Meteorol. Soc.*, **124**, 615-636.

Hayashi, Y., 1970: A theory of large-scale equatorial waves generated by condensation heat and accelerating the zonal wind. *J. Meteor. Soc. Japan*, **48**, 140-160.

Houze, R. A. Jr., 1997: Stratiform precipitation in regions of convection: A meteoroloical paradox? *Bull. Amer. Meteor. Soc.*, **78**, 2179-2196.

Lane, T.P. and M. J. Reeder, 2001: Convectively generated gravity waves and their effect on the cloud enviroment. *J. Atmos. Sci.*, **58**, 2427-2440.

Lau, K.-M. and L. Peng, 1987: Origin of low-frequency (intraseasonal) oscillations in the tropical atmosphere. Part 1: Basic theory. *J. Atmos. Sci.*, **44**, 950-972.

Lindzen, R. S., 1967: Wave-CISK in the tropics. *J. Atmos. Sci.*, **31**, 156-179.

Khairoutidnov, M. F., and D. A. Randall, 2003: Cloud resolving modeling of the ARM Summer 1997 IOP: Model fomulation, results, uncertainties, and sensitivities. *J. Atmos. Sci.*, **60**, 607-625.

Madden, R. and P. Julian, 1994: Observations of the 40-50-day tropical oscillation- A review. *Mon. Wea. Rev.*, **122**, 814-837.

Majda, A. J. and M. G. Shefter, 2001: Models for stratiform instability and convectively coupled waves. *J. Atmos. Sci.*, **58**, 1515-1535.

Mapes, B. E., 1993: Gregarious tropical convection. *J. Atmos. Sci.*, **50**, 2027-2037.

Mapes, B. E., 1998: The large-scale part of tropical mesoscale convective circulations: a linear vertical spectral band model. *J. Meteor. Soc. Japan*, **76**, 29-55.

Mapes, B. E., 2000: Convective inhibition, subgrid-scale triggering energy, and stratiform instability in a toy tropical wave model., *J. Atmos. Sci.*, **57**, 1515-1535.

Marshall, J. S. and W. McK. Palmer, 1948: The distribution of raindrops with size. *J. Meteor.*, **5**, 165-166.

McClatchey R. A., R. W. Fenn, J. E. A. Selby, F. E. Volz, and J. S. Garing, 1972: Optical Properties of the atmosphere (third edition). Air Force Cambridge Research Laboratories. Environemtal Research Papers, No. 411.

Nakazawa, T., 1988: Tropical super clusters within intraseasonal variations over the western Pacific. *J. Meteor. Soc. Japan*, **66**, 777-786.

Numagati A. and Y. Hayashi, 1991: Behavior of cumulus activity and the structures of circulations in an "aqua planet" model. Part 1: The structure of super clusters. *J. Meteor. Soc. Japan*, **69**, 541-561.

Nicholls, M. E., R. A. Pielke, and W. R. Cotton, 1991: Thermally forced gravity waves in an atmosphere at rest, *J. Atmos. Sci.*, **48**, 1869-1884.

Oouchi, K., 1999: Heirarchical organization of super cloud clusters caused by WISHE, convectively induced gravity waves and cold pool. *J. Meteor. Soc. Japan.*, **77**, 907-927.

Pandya, R. D., D. Durran, and C. Bretherton, 1993: Comments on "Thermally forced gravity waves in an atmosphere at rest",

Randall, D. A. and G. F. Huffman, 1980: A stochastic model of cumulus clumping, *J. Atmos. Sci.*, **37**, 2068-2078.

Randall, D. A., Hu Q., Xu, K.-M. and Kreuger, S. K., 1994: Radiative-convective disequilibrium, *Atmos. Res.*, **31**, 315-327.

Randall, D. A., M. Khairoutdinov, A. Arakawa, W. Grabowski, 2002: Breaking the cloud-paramterization deadlock, *Bull. Amer. Meteor. Soc.*, submitted.

Rickenbach T. M. and S. A. Rutledge, 1998: Convection in TOGA COARE: horizontal scale, morphology, and rainfall production. *J. Atmos. Sci.*, **55**, 2715-2729.

Sherwood, S. 1999: Convective precursors and predictability in the tropical western Pacific.*Mon. Wea. Rev.*, **127**, 2977-2991.

Smolarkiewicz, P. K. and W. W. Grabowski, 1990: The multi-dimensional positive definite advection transport algorithm: Non-oscillatory option. *J. Comput. Phys.*, **86**, 355-375.

Stark, T. E., 1976: Wave-CISK and cumulus parameterization. *J. Atmos. Sci.*, 33, 2383-2391.

Straub K. and G. Kiladis, 2002: Observations of convectively coupled Kelvin waves in the eastern Pacific ITCZ, *J. Atmos. Sci.*, **59**, 30-53.

Straub K. and G. Kiladis, 2003: Observations of convectively coupled Kelvin waves in the eastern Pacific ITCZ, *J. Atmos. Sci.*, **59**, 30-53.

Takayabu Y. N., 1994: Large-scale cloud disturbances associated with equatorial waves. Part I: Spectral features of the cloud disturbances. *J. Meteor. Soc. Japan*, **72**, 433-448.

Tao, W.-K. and J. Simpson, 1987: Modelling study of a tropical squall-type convective line. *J. Atmos. Sci.*, **46**, 177-201.

Wheeler M. and G. Kiladis, 1999: Convectively coupled equatorial waves: analysis of clouds and temperature in the wavenumber-frequency domain. *J. Atmos. Sci.*, **56**, 374-399.

Wheeler M. , G. Kiladis, and P. Webster, 2000: Large-scale dynamical fields associated with convectively coupled equatorial waves *J. Atmos. Sci.*, **57**, 613-639.

Xu, K. M., A. Arakawa, and S. K. Krueger, 1992: The macroscopic behavior of cumulus ensembles simulated by a cumulus ensemble model. *J. Atmos. Sci.*, **49**, 2402-2420.

Xu, K. M. and D. A. Randall, 1996: Influence of large-scale advective cooling and moistening effects on the quasi-equilibrium behavior of explicitly simulated cumulus ensembles. *J. Atmos. Sci.*, **55**, 896-909..